Title

Development and Translation of Novel Hyperpolarized C-13 MRI Technologies for Prostate Cancer Clinical Research

Author

Gebrezgiabhier, Daniel Tewelde

Publication Date

2024

Peer reviewed|Thesis/dissertation

Development and Translation of Novel Hyperpolarized C-13 MRI Technologies for Prostate Cancer Clinical Research

by

Daniel Gebrezgiabhier

DISSERTATION

Submitted in partial satisfaction of the requirements for degree of

DOCTOR OF PHILOSOPHY

in

Bioengineering

in the

GRADUATE DIVISION

of the

UNIVERSITY OF CALIFORNIA, SAN FRANCISCO
AND
UNIVERSITY OF CALIFORNIA, BERKELEY

Approved:

DocuSigned by:
Dan Vigneron
DA5485F9C42341E...

Dan Vigneron

Chair

DocuSigned by:
Peder Larson
DocuSigned by:

Peder Larson

DocuSigned by:
Robert Bok
Signed by:

Robert Bok

DocuSigned by:
Steven Conolly
F1C9CE9002F94E0...

Steven Conolly

Committee Members

Dedicated to my family:

My parents, Fr. Tewelde Kidanemariam and Genet Weldemikael; and my siblings,

Eden, Feven, Luela, Luwam, Robiel, and Mikal.

Acknowledgements

During the past few years in graduate school, I am extremely fortunate to receive all the help and support from my mentors, co-workers, friends, family members and the entire Habesha community.

First and foremost, I would like to express my heartfelt gratitude to my academic advisor, Dr. Dan Vigneron, for being so patient and an extraordinary mentor. During my time as a graduate student, I have received his guidance not only in research but in all aspects of life. Despite the lockdown of the pandemic and limited access to the lab, I was able to gain his undivided attention and guidance in conducting research, writing grants, and his passion towards science. Dan has always reminded me of the goal ahead by reiterating that giving up was not an option even when I almost gave up. I am truly grateful for everything he did to support me to become the scientist I am today.

I would also like to greatly appreciate Dr. Peder Larson, for being so supportive over the years and teaching me so much about MRI, both from his classes and from serving on my qualifying and dissertation committees. When I felt lost after three rotations in my first year, Peder's guidance and suggestions were crucial in helping me join the Vigneron's lab, and I am very grateful. Peder's help was throughout my graduate years at UCSF, including all the technical development (pulse sequence programming, data analysis, RF design, etc) and all the inspiring discussions.

I would like to thank Dr. John Kurhanewicz for sharing his insights on prostate cancer NMR, and for chairing my qualifying committee, Dr. Duan Xu for mentoring me throughout my PhD as my graduate advisor, for keeping on my track for research and classes, Dr. Steven Conolly for also being on both my qualifying and dissertation committees. I want to give special thanks to Dr. Robert Bok for all his help before, during, and after each one of the patient studies and being on both my qualifying and dissertation committees, Dr. Jeremy Gordon for all the great discussions and guidance for my projects and teaching me a lot about MATLAB and for all the help during human studies.

I would like to greatly appreciate Lucas Carvajal for teaching me everything I know on coils and being a close friend, Dr. Hsin-Yu Chen for teaching me and guiding me through patient studies and post processing, Dr. Yaewon Kim for teaching me how to do NMR and always helping during patient studies, Tanner Nickles for always being a great colleague, for his insightful discussions and helping me in many ways, Romelyn Delos Santos, Mary McPolin, and Kimberly Okamoto for their help during patient scans.

Many thanks go to Jenny Che for always being available to help in every way possible, Cresini Tabaranza-David, Kim Semien, Victoria Starrett, Rocio A Sanchez for all their kind administrative support in the past few years. They all helped me in various ways with my projects and experiments, and I feel extremely fortunate to work with them.

I would like to thank my uncles Tekeste Kidane and Girmalem Kidane for their encouragement, motivation and inspiring me to pursue science during my younger years. My cousin Mekonnen Beraki with all his family for always being there for me during the toughest times , my best friend Meseret Sium with all his family for always checking on me, my best friend Isaac Tewolde and his wonderful wife Ruta Berhanemeskel for being my rock throughout the years. I would also like to thank my counselor from Grand Rapids Community college, Anna Maria Clark for keeping track of my progress and always encouraging me to do great. I would like to thank Olivier and Nicole Jolliet for welcoming me to their home and family during my undergraduate years at Ann Arbor, Michigan.

Lastly, I could not have become the person I am without the unconditional love from my family – my grandparents, my parents, my siblings, my uncles and aunts, and my cousins. I am forever grateful for their inspiration, encouragement, sacrifices, and support.

Daniel Gebrezgiabhier

October 17, 2024

Contributions

Chapter 3 is a paper submitted for publishing, and I am the first author for. Chapters 4, 5 and 6 cited below are already published, and I contributed to the device development, methodology, formal analysis, investigation, data curation, writing, review, and editing.

Chapter 3:

"Development of New Endorectal Coil and Novel Methods for Improving Multiparametric MR-TRUS Guided Fusion Prostate Biopsies with Hyperpolarized C-13 Pyruvate Molecular Imaging." Daniel T. Gebrezgiabhier, Lucas Carvajal, Hsin-Yu Chen, Robert A. Bok, Matthew R. Cooperberg, Hao G. Nguyen, Katsuto Shinohara, Kimberly Okamoto, Yaewon Kim, Mary Frost, Zhen J. Wang, Michael A. Ohliger, Jeremy W. Gordon, Peder E.Z. Larson, Rahul Aggarwal, and Daniel B. Vigneron. Magn Reson Med. 2024 Submitted

Chapter 4:

"Improving Multiparametric MR - TRUS Guided Fusion Prostate Biopsies with Hyperpolarized ^{13}C Pyruvate Metabolic Imaging : A Technical Development Study." Hsin-Yu Chen, Robert A. Bok, Matthew R. Cooperberg, Hao G. Nguyen, Katsuto Shinohara, Antonio C. Westphalen, Zhen J. Wang, Michael A. Ohliger, Daniel Gebrezgiabhier, Lucas Carvajal, Jeremy W. Gordon, Peder E.Z. Larson, Rahul Aggarwal, John Kurhanewicz, and Daniel B. Vigneron. Magn Reson Med. 2022 Dec;88(6):2609-2620. doi: 10.1002/mrm.29399. Epub 2022 Aug 17. PMID: 35975978; PMCID: PMC9794017.

Chapter 5:

"Development of Specialized Magnetic Resonance Acquisition Techniques for Human HP [^{13}C,$^{15}N_2$]Urea + [1-^{13}C]Pyruvate Simultaneous Perfusion and Metabolic Imaging." Xiaoxi Liu, Shuyu

Tang, Changhua Mu, Hecong Qin, Di Cui, Ying-Chieh Lai, Andrew M. Riselli, Romelyn Delos Santos, Lucas Carvajal, Daniel Gebrezgiabhier, Robert A. Bok, Hsin-Yu Chen, Jeremy W. Gordon, Daniel B. Vigneron, John Kurhanewicz, Peder E.Z. Larson. Magn Reson Med. 2022; 88(3):1039-1054. doi: 10.1002/mrm.29266. PMCID: PMC9810116.

Chapter 6:

"Dual Hyperpolarized [1-^{13}C]Pyruvate and [^{13}C]Urea Magnetic Resonance Imaging of Prostate Cancer." Ivan de Kouchkovsky, Hao Nguyen, Hsin-Yu Chen, Xiaoxi Liu, Hecong Qin, Bradley A. Stohr, Romelyn Delos Santos, Michael A. Ohliger, Zhen Jane Wang, Robert A. Bok, Jeremy W. Gordon, Peder E. Z. Larson, Mary Frost, Kimberly Okamoto, Daniel Gebrezgiabhier, Matthew Cooperberg, Daniel B. Vigneron, John Kurhanewicz, Rahul Aggarwal. Journal of Magnetic Resonance Open, 2024; https://doi.org/10.1016/j.jmro.2024.100165

Development and Translation of Novel Hyperpolarized C-13 MRI Technologies for Prostate Cancer Clinical Research

Daniel Tewelde Gebrezgiabhier

Abstract

Prostate cancer is one of the most common cancers in men and second leading cause of death cancer in the United States of America. Current clinical imaging modalities provide limited information on prostate cancer aggressiveness and response to therapy required for optimal patient management. To reduce the mortality rates, early detection and diagnosis of prostate cancer is crucial. Thus, there is a clinical need for improved noninvasive accurate histopathologic diagnosis and grading of prostate cancer. Currently, transrectal ultrasonography (TRUS)–guided biopsy is the standard approach for histopathologic diagnosis and grading of prostate cancer. However, TRUS is limited for directly visualizing and targeting prostate lesions and therefore the fusion of magnetic resonance (MR) images with US was developed to overcome many of these limitations. The development of endorectal (ER) coils has further improved prostate tumor visualization on MR images as the endorectal coil used in an MRI-guided prostate biopsy helps provide more detailed images from the prostate and surrounding structures. However, conventional anatomic and diffusion MR images do not provide metabolic information on prostate cancer aggressiveness and extent. Recent studies with the emerging hyperpolarized (HP) carbon-13 (^{13}C) MR imaging technique have shown that hyperpolarized (HP) ^{13}C-pyruvate MRI in a rapid 1-minute addition to conventional proton MRI exams can detect metabolic reprogramming in prostate cancer improving the detection of aggressive cancers and for

monitoring response to therapy. Dual-agent ([1-^{13}C]-pyruvate, [1-^{13}C,$^{15}N_2$]-urea) hyperpolarized ^{13}C MRI can also be used to simultaneously assess tumor metabolism and tissue perfusion in patients with localized prostate cancer; Thus, this project was designed to develop specialized hardware and software to enable multiparametric MR incorporating hyperpolarized (HP) ^{13}C MR molecular imaging for improved characterization and MR- US fusion biopsy guidance. In this dissertation project, new methods and detector hardware to acquire and display ^{13}C-pyruvate to ^{13}C-lactate conversion rate constants (k_{PL}) images were developed and applied for guiding MR-US fusion biopsies in prostate cancer patients for the first time.

Table of Contents

List of Figures

List of Tables

Chapter 1: Introduction

Magnetic resonance imaging (MRI) is one of the commonly used medical imaging modalities which is both non-invasive and non-radioactive. MRI provides high spatial resolution imaging with excellent soft tissue contrast that enables a broad range of clinical applications including various types of cancers, neurological disease, cardiovascular disease, and musculoskeletal disease. MRI also can be used to obtain a wide variety of valuable biomedical information beyond just anatomy depictions including perfusion, metabolism, tissue structure, and function.

Current conventional clinical MRI relies on the MR signals emitted by proton atoms (^{1}H). However, this limits the modality and does not provide kinetic metabolic information on cancer aggressiveness or treatment response. The MR active carbon-13 atom is a crucial element of organic molecules, and enables ^{13}C MR to detect an extremely wide range of chemicals in living organisms and thereby can provide valuable metabolic information. However, ^{13}C MR is limited by low gyromagnetic ratio, low active spin distribution, and low natural abundance(1%).

Hyperpolarized ^{13}C MRI is an emerging molecular imaging modality based on an unprecedented gain in signal intensity of 10,000- to 100,000-fold that has been used to monitor uptake and enzymatic conversions of naturally-occurring biomolecules. Thus, hyperpolarization via dynamic nuclear polarization (dDNP) amplifies the weak C-13 signal for a significantly enhanced SNR. Studies of HP ^{13}C-pyruvate imaging has shown the conversion of pyruvate to its metabolites aligns with the Warburg effect in that increased pyruvate to lactate conversion is observed even in the presence of oxygen in prostate cancers due to oncogenic mutations and tumor microenvironment adaptation to promote proliferation.

In this dissertation project, novel bioengineering technologies and applications of hyperpolarized ^{13}C MRI, were developed and investigated. The overall goals were to improve metabolic imaging of aggressive tumors and evaluate HP ^{13}C-MR-TRUS fusion biopsy guidance for prostate cancer patients.

Chapter 2 intends to provide the reader with scientific and technical background of the dissertation. This chapter outlines the background information for this dissertation, including quantum physics understanding of MR signals, fundamental principles of MR imaging, hyperpolarization techniques and corresponding imaging considerations, and specialized RF coil development for hyperpolarized C-13 prostate studies.

Chapter 3 describes the development of a new dual-element endorectal coil and preliminary comparative results from both phantom and Active Surveillance (AS) patient studies. A new $^{13}C/^{1}H$ dual-element endorectal coil was designed, 3D printed and manufactured with optimal dimensions to improve the comfort and tolerability for patients and achieve higher SNR over the original endorectal coil used for over a decade. After bench and phantom tests, the new endorectal coil was used in patient studies for mpMRI-TRUS guided fusion prostate biopsies with hyperpolarized C-13 pyruvate molecular imaging in three patients on active surveillance. The results of this novel approach with the new $^{13}C/^{1}H$ ERC demonstrated an increase in sensitivity, image quality and ultimately supports better detection of lesions.

Chapter 4 presents development of techniques and establishment of a workflow using hyperpolarized ^{13}C (HP ^{13}C) MRI and the pyruvate-to-lactate conversion rate (k_{PL}) biomarker to guide MR-transrectal ultrasound (TRUS) fusion prostate biopsies. This technical development study

demonstrated the feasibility of adding HP ^{13}C-pyruvate MRI to guide TRUS fusion prostate biopsies. HP-MRI was integrated into the diagnostic mpMRI workflow, complete with identification of ^{13}C research targets and sampling of these targets in fusion biopsies. These initial results support future studies in larger cohorts of patients to evaluate the role of HP ^{13}C MRI guided targeted biopsy for improving prostate cancer risk stratification.

Chapter 5 presents the development and demonstration of the *in vivo* feasibility of a 3D balanced steady-state free precession (3D-bSSFP) urea sequence with a stack-of-spiral acquisition for improving the signal-to-noise ratio (SNR) and spatial resolution of the first hyperpolarized ^{13}C MRI human studies with the injection of co-hyperpolarized [1-^{13}Cpyruvate and [^{13}C, $^{15}N_2$]urea imaging contrast agents and utilizing the new endorectal coil described in chapter 3. The 3D-bSSFP urea sequence with a stack-of-spiral acquisition has been demonstrated to significantly increase the SNR and image quality for [^{13}C, $^{15}N_2$]urea in co-hyperpolarized [1-^{13}C]pyruvate and [^{13}C, $^{15}N_2$]urea imaging studies. This work lays the foundation for future human studies to achieve high-quality, high-SNR, and simultaneous metabolism and perfusion imaging.

Chapter 6 describes the first-in-human co-hyperpolarized [1-^{13}C]pyruvate and [^{13}C, $^{15}N_2$]urea imaging study with histopathology correlations. This unprecedented first-in-human radiopathologic study demonstrated the feasibility of dual-agent HP MRI in PC patients, and the potential for simultaneous assessment of tumor metabolism and perfusion to detect aggressive prostate cancer.

Chapter 7 summarizes the overall bioengineering technical developments, applications investigated in this dissertation and discusses future directions of hyperpolarized ^{13}C metabolic imaging translations and implications.

Chapter 2: Scientific and Technical Background

2.1 Basics of Magnetic Resonance Imaging

Magnetic Resonance Imaging (MRI) is a powerful non-invasive and nonionic medical imaging modality that uses a strong magnetic field, magnetic field gradients, and radio waves to acquire images of anatomical organs and physiological processes. MRI provides a variety of information including anatomy, perfusion, metabolism, tissue structure, and function. In this chapter, the basics of MRI background information with their inherent scientific principles that are crucial to accomplish and fully understand both technical and experimental methods underlying the imaging research conducted for this dissertation will be covered, including topics on spin physics, Radiofrequency (RF) pulses and excitation, relaxation, Bloch equations, localization, hyperpolarization, and RF coils.

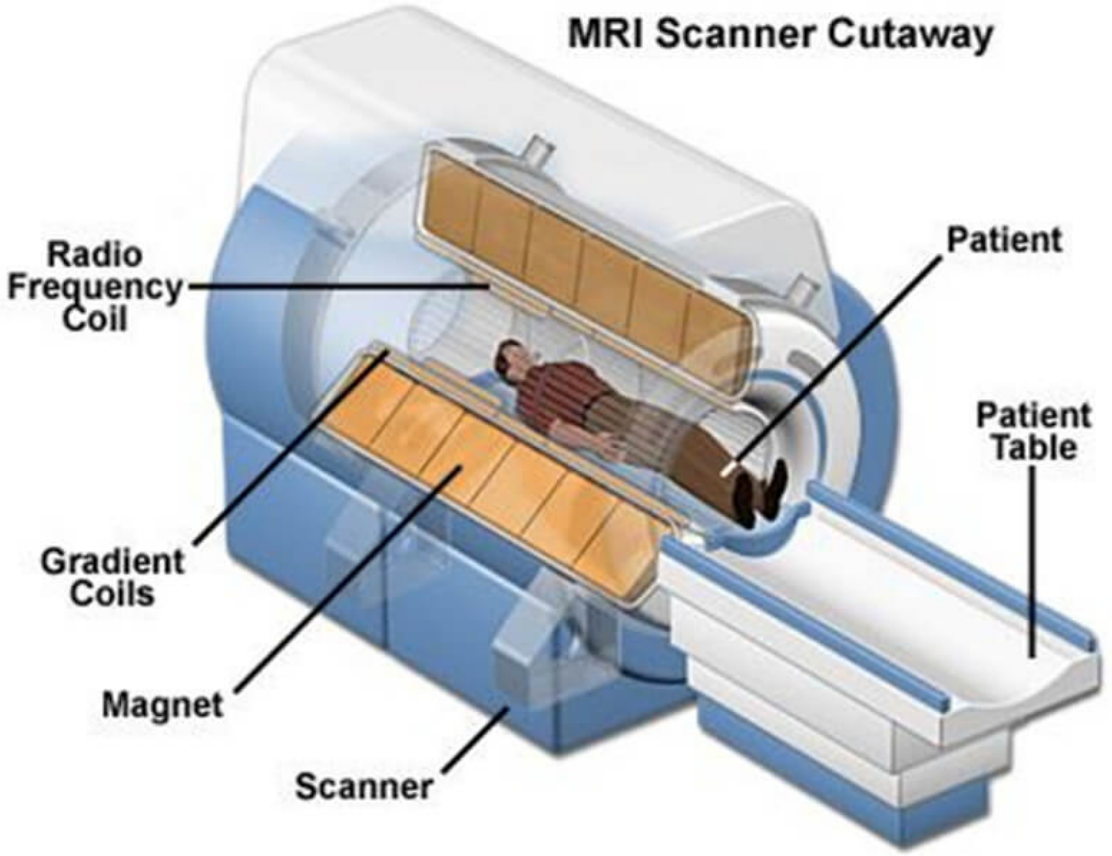

Figure 2.1: Magnetic Resonance Imaging (MRI) scanner and all its different parts. (Adapted from https://www.dofrp.com/cases-study/mri-coils/).

2.1.1 Nuclear Spins, Magnetic Resonance, Polarization

The charge and angular momentum of atomic nuclei and their interactions with electric and magnetic field explains the magnetic resonance (MR) phenomenon[1]. Nuclear spin is a quantum mechanical angular momentum that physically can be detected by nuclear magnetic resonance (NMR). As nuclear spin is the intrinsic form of angular momentum of subatomic particles, the nucleus of an atom exhibits an overall spin depending on the number of protons and neutrons of which it is comprised. Consequently, MR active atomic nuclei with an odd number of protons and/or odd number of neutrons possess an intrinsic angular momentum, and an associated magnetic dipole moment $\boldsymbol{\mu}$. Atomic nuclei with even number of protons and neutrons are MR invisible[2], as the nucleus spin are paired against each other resulting in a net result of no spin. In living organisms, MR active nuclei can have a spin of half or an integer. Atomic nuclei with the number of protons plus the number of neutrons as odd have a half-integer spin such as 1/2, 3/2 and 5/2 while atomic nuclei with odd number of protons and odd number of neutrons have an integer spin (e.g. deuterium, ^{2}H). In living organisms, ^{1}H is the most abundant MR active nuclei with a half-integer spin since water (H_2O) is the key component of most living tissues. Other common nuclei that fulfill the requirement for MR activity and provide pertinent biological information, include ^{13}C, ^{15}N, ^{19}F, ^{23}Na, ^{31}P, and ^{129}Xe[1].

A non-zero nuclear spin of a given molecule (whether alone, or in solution, or even in a complex cellular environment) give rise to a signal with a unique frequency as its molecular signature that can be detected, observed and quantified. Thus, nuclear spin angular momentum refers to the intrinsic angular momentum associated with the spin of a nucleus, which plays a crucial role in describing the coupling between the nuclear spin and the rotational angular momentum of a molecule in the context of molecular energy levels. The spin angular momentum, S is a vector quantity as its directionality is aligned along its axis of rotation can be expressed as follows,

$$\boldsymbol{S} = \frac{h}{2\pi}\boldsymbol{I} \tag{2.1}$$

where $\boldsymbol{h}$ is Planck's constant ($6.62607004 \times 10^{-34}$ m^2 kg / s), and **I** is the spin angular momentum quantum number in quantum mechanics and is related to the magnetic dipole moment $\boldsymbol{\mu}$ and can be expressed as follows,

$$\boldsymbol{\mu} = \gamma \boldsymbol{S} = \gamma \frac{h}{2\pi}\boldsymbol{I} \tag{2.2}$$

where γ is the gyromagnetic ratio, a specific constant for a given nuclear species[1]. The magnetic moment ($\boldsymbol{\mu}$) is a vector quantity used to measure the tendency of an object to interact with an external magnetic field. In NMR, the object of interest is typically a molecule, atom, nucleus, or subatomic particle. The object's intrinsic magnetic properties are often visualized as emanating from a tiny bar magnet with north and south poles (the "dipoles"), and is therefore also called the magnetic dipole moment.

As depicted in Figure 2.2(a), in the absence of an external magnetic field B_0, the spins are at thermal equilibrium where no heat entering or leaving the system and would be randomly oriented in space with the same energy level canceling each other out, resulting in a macroscopically zero magnetization[3]. In the presence of an external magnetic field, B_0, the spins with a spin quantum number *I* can assume 2*I*+1 energy states. For instance, since ^{1}H of spin $\frac{1}{2}$ ($I = \frac{1}{2}$), ^{1}H spins have two distinct energy states where one of the energy states is almost aligned or parallel (n^+) with the applied external magnetic field, while the other one is almost opposite or anti-parallel (n^-) to the external magnetic field. As depicted in Figure 2.2, there is a small energy difference between these two states which causes a difference in the spin populations of each state and subsequently results in a non-zero macroscopic magnetization(M_0)[3] that is of profoundly fundamental to MR.

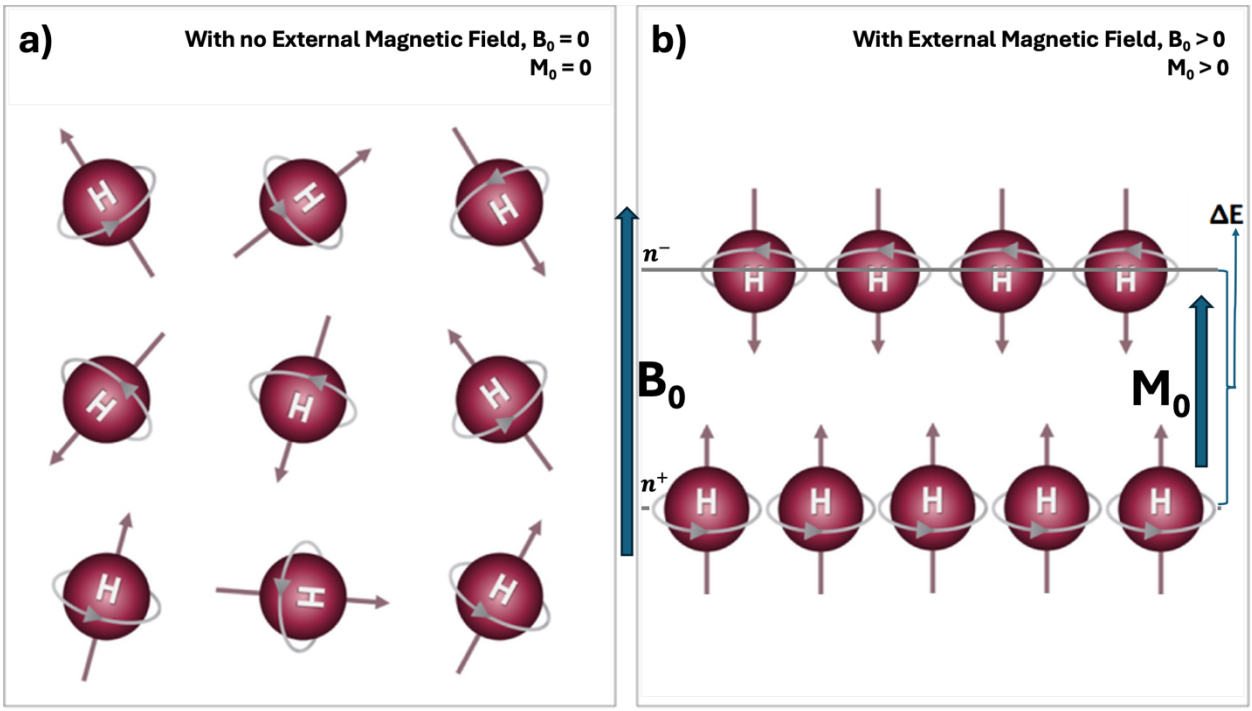

Figure 2.2: Nuclear spin with and without external magnetic field. a.) At thermal equilibrium without an external magnetic field, nuclear spins are randomly aligned with the same energy level, resulting in a zero net magnetization. b.) When an external magnetic field is applied, spins will split between energy states, resulting in more spins in lower energy level and a non-zero net magnetization parallel to the applied static magnetic field.

The spin population ratio between the parallel (n^+) and anti-parallel (n^-) is described by the Boltzmann's distribution[1,3], as follows:

$$\frac{n^-}{n^+} = e^{-\frac{\Delta E}{k_B T}} = e^{\frac{-\gamma \hbar B_0}{k_B T}} \tag{2.3}$$

where ΔE is the energy difference between the spin states, k_B is the Boltzmann's constant (1.38064852 $\times 10^{-23}$ m^2 kg s^{-2} K^{-1}), T is temperature in Kelvin, h is Planck's constant, and B_0 is the strength of the external magnetic field. Therefore, the thermal polarization, $P_{thermal}$, could be defined as[1,3]:

$$P_{thermal} = \frac{n^+ - n^-}{n^+ + n^-} = \tanh\left(\frac{\gamma \hbar B_0}{2 k_B T}\right) \tag{2.4}$$

The formula (Equation 2.4) for thermal polarization describes the fraction of total spins that are aligned with the external magnetic field B_0, and for any given nuclei, the observable magnetization

signal is directly proportional to the magnetic field strength and inversely proportional to temperature. In order to have a strong observable signal, strong magnetic field and lower temperature is required.

Table 2.1: Gyromagnetic ratio, natural abundance, Larmor frequency and spin number of commonly used MR isotopes at 3T

Nuclear	Gyromagnetic Ratio $\frac{\gamma}{2\pi}$ (MHz/T)	Natural Abundance (%)	Spin	ω (MHz at B_0 of 3 T)
^{1}H	42.576	~100	1/2	127.7
^{13}C	10.705	1.109	1/2	32.13
^{15}N	-4.316	0.37	1/2	-12.948
^{19}F	40.078	~100	1/2	120.2
^{23}Na	11.262	~100	3/2	33.78
^{31}P	17.235	~100	1/2	51.72
^{129}Xe	-11.777	24.4	1/2	-35.331

The motion of a spinning top is a great analogy for magnetic resonance spins[4]. A spinning top placed on a level surface rotates around a vertical axis through its foot, with the gravitational field applying a torque for the rotation. Likewise, when the magnetic resonance spins are placed in a magnetic field, the magnetic field apply a torque to the spins, and the spins would have an angular momentum and a magnetic moment; and thus, subsequently cause the spins to rotate around an axis. This behavior is called precession[3]. The angular velocity of this rotation (ω_0), also called the Larmor frequency[3], is dependent only on the gyromagnetic ratio (γ) and the strength of the applied external magnetic field (B_0), and can be described as follows:

$$\omega_0 = \gamma B_0 \tag{2.5}$$

2.1.2 Linear Gradient Fields

When a static magnetic field B_0 is applied in the z-direction, all the spins would resonate at resonance frequency ω_0; and when the spins are excited, they would behave like oscillators and induce oscillating signals at ω_0[1]. However, if all spins behave identically the same, the RF receive coils would only receive a cohesive signal without differentiation to any spatial information. If only $\mathbf{B}_0$ exits, as the RF transmit/receive coil encompasses the center region of interest (ROI), exciting a selected portion of the volume or distinguish the signals generated from different spatial locations is not possible[1]. The fact that the total signal generated by all the oscillators of the excited region in a single time waveform is recorded is where the problem lies[1].

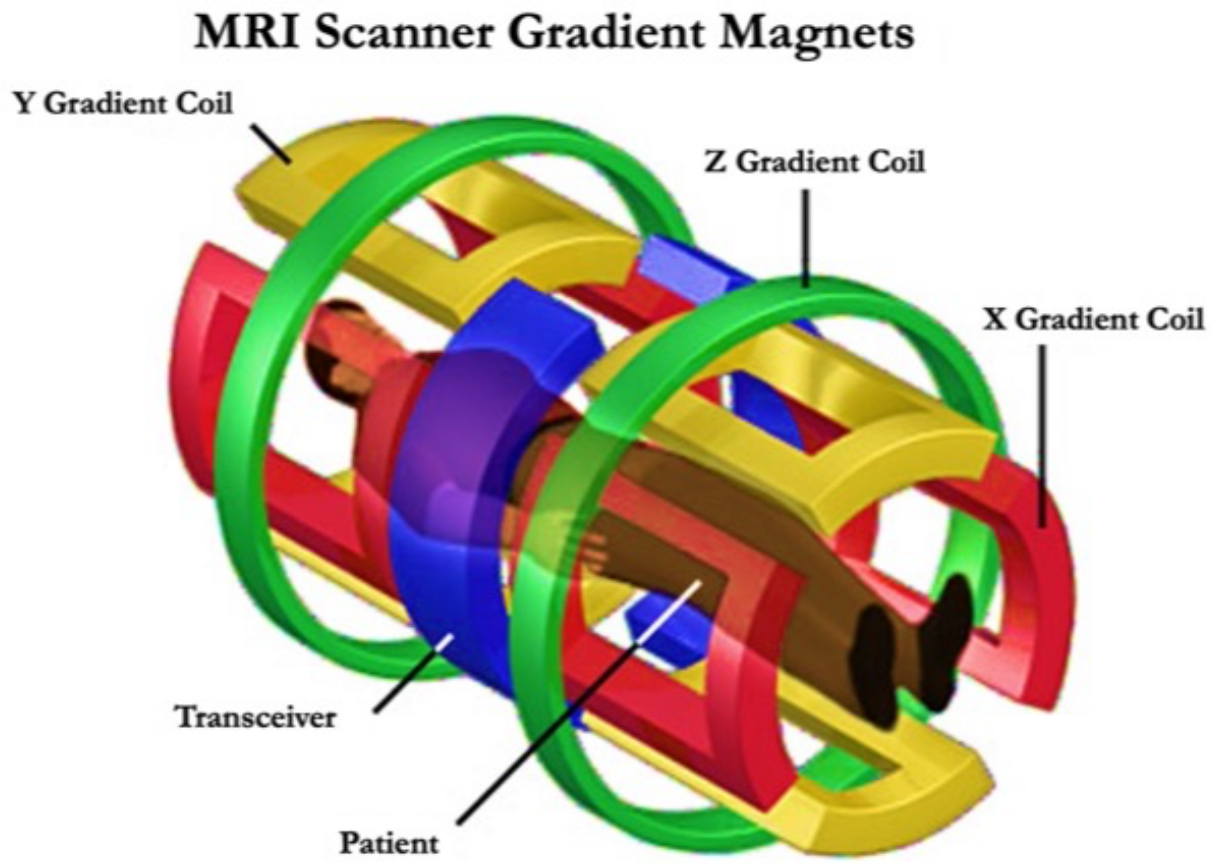

Figure 2.3: MRI Scanner Gradient magnets showing all the three gradient fields are used for spatial localization. (Adapted from http://www.magnet.fsu.edu).

In MRI, the above mentioned problem is resolved by applying linear gradient fields on top of the static magnetic field B_0 that way spatial localization is achieved. For instance, if a gradient field G_y is applied along the y-direction, then the total applied magnetic field strength along the y-direction is $B_0 + yG_y$, resulting to varying frequencies for the spins at different locations along the y-direction. Thus, the derived precession frequency along the y-direction is:

$$\omega(y) = \gamma(B_0 + yG_y) \tag{2.6}$$

If a gradient field G_x is applied along the x-direction or G_z is applied along the z-direction, their respective total applied magnetic field strength along the x-direction and z-direction would be $B_0 + xG_x$ and $B_0 + zG_z$ respectively, and their precession frequency follows Eqn. 2.6. By creating this inhomogeneous magnetic field, spatially localized information can be determined from the different precession frequencies as the resonant frequency of a nucleus is proportional to the applied magnetic field strength and frequency changes when the magnetic field strength changes[1].

2.1.3 Magnetization and Radiofrequency Field

As discussed above, the presence of static external magnetic field B_0 gives rise to a tendency of the spins to align in the direction of B_0, giving rise to a net magnetization moment $\mathbf{M}$[1], and the spins exhibit resonance which is manifested by precessional behavior at the resonance frequency[1]. Although precession allows the MR signal to be detected, another external magnetic field, $\mathbf{B_1}$, needs to be applied to tilt the magnetization to the transverse plane (xy-plane) from the longitudinal axis (z-direction) to allow signal detection to happen. In addition, the frequency of this $\mathbf{B_1}$ field must be the Larmor resonant frequency for the deflection of the magnetization.

Radiofrequency (RF) coils (discussed in section 2.4) are used to generate $\mathbf{B_1}$ to perturb the net magnetization from its equilibrium state[1]. According to the Faraday's law of induction, the precessing magnetization causes a change in flux in the RF coil and thereby inducing a small electromotive force

(EMF). As depicted in Figure 2.4 for RF excitation and MR signal detection, this resulting time signal is commonly called a free induction decay (FID), which can be Fourier Transformed to create a MR image or spectrum.

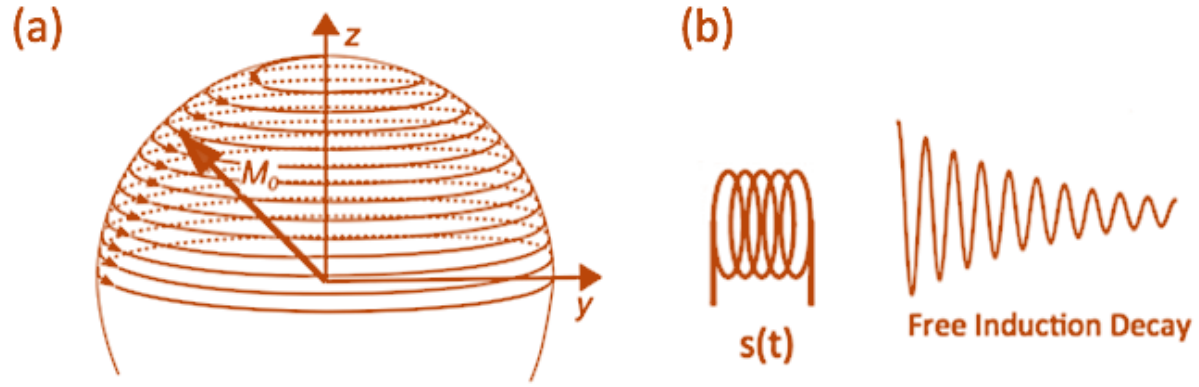

Figure 2.4: Depicts RF excitation and MR signal detection. (a) When $\mathbf{B}_1$ is applied, the magnetization is tilted away from the +z direction to precess around the z-axis with the Larmor frequency. (b) Tuned and matched RF coils are used for RF pulse excitation and reception of signals from the free induction decay (FID). [Adapted from Faber et al[3] and Swisher 2014[6]]

The extent to which **M** rotates around $\mathbf{B}_1$ is called the flip angle α. For an RF pulse duration of τ, the flip angle α between the +z-axis and the tilted magnetization is given by the following integral:

$$\alpha = \int_0^{\tau} \gamma B_1(t) dt \qquad (2.7)$$

The flip angle (α) of a hard pulse which is a constant RF pulse with no spatial selection, can be expressed as:

$$\alpha = \gamma B_1 \tau \qquad (2.8)$$

Figure 2.5 shows examples of several common types of RF pulses (a hard pulse, a spatially selective pulse, and a spectral-spatial pulse). The simplest RF pulse with no spatial and spectral selectivity, and with a constant $\mathbf{B}_1$ field amplitude; and without any gradient turned on simultaneously as shown in Figure 2.3 (a) is the hard pulse, all spins within the volume are excited to have transverse plane components. Using a sinc-shaped $\mathbf{B}_1$ RF pulse with a gradient turned on simultaneously on the

desired spatial dimension that the spatial selectivity could be achieved as can be shown Figure 2.5 (b). The excited slice thickness (Δz) is mathematically described as:

$$\Delta z = \frac{\Delta f}{\frac{\gamma}{2\pi} G_z} \tag{2.9}$$

where G_z is the applied gradient field strength in z-direction, and Δf is the excitation bandwidth of the RF pulse. If the flip angles are small (α<30^0), the excitation profile of a $\mathbf{B_1}$ is the Fourier Transform of the RF pulse. Figure 2.5 (c) depicts a more complicated RF pulse with both spectral and spatial selectivity.

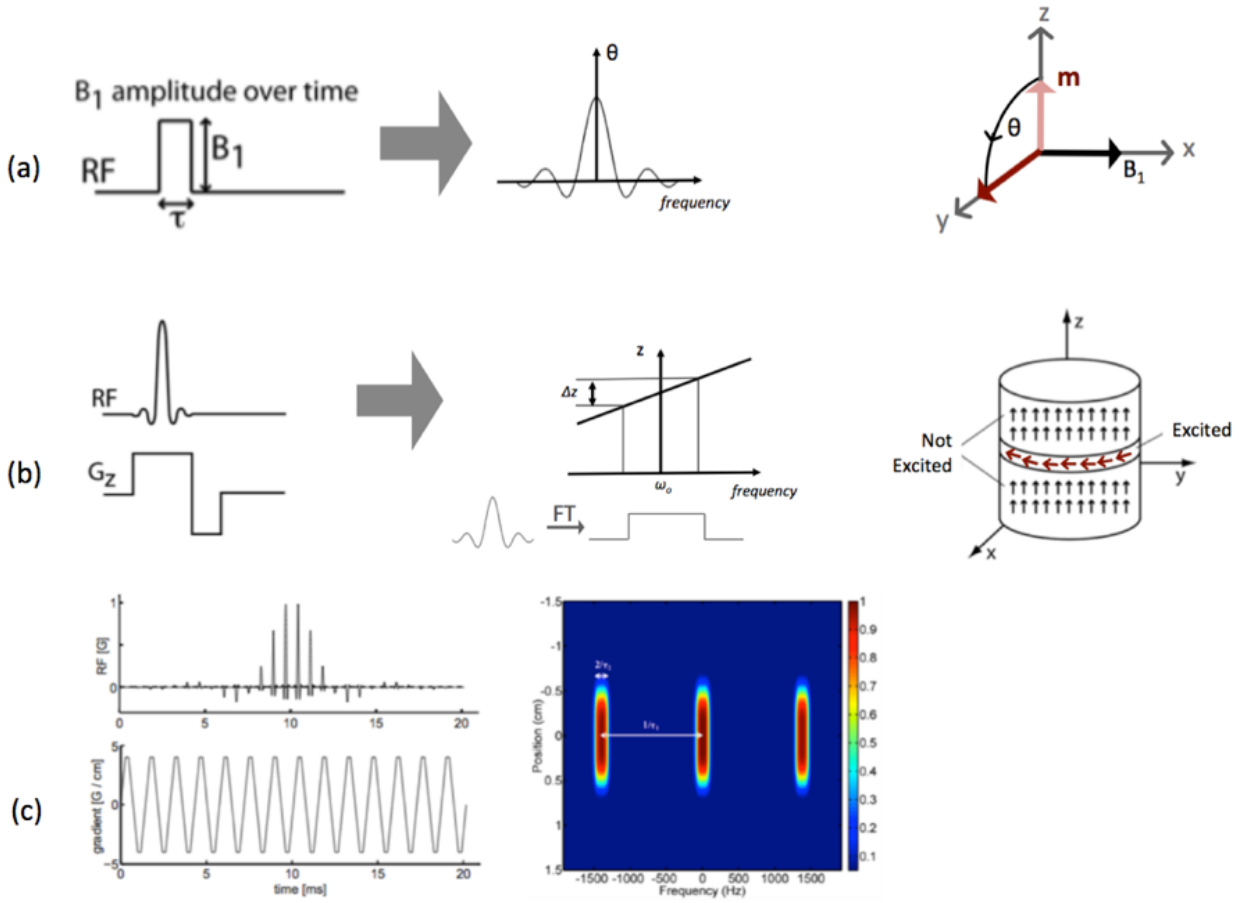

Figure 2.5: Shows examples of common RF pulses (a) a hard pulse, the simplest and most straight forward pulse. (b) a spatially selective pulse, and (c) a spectral-spatial pulse that has applications for HP ^{13}C MRI. (Adapted from Swisher 2014[6] and Larson et al[7]).

This RF pulse with both spectral and spatial selectivity and small tip approximation for flip angles is frequently used for hyperpolarized (HP) ^{13}C MR imaging to suppress unwanted metabolite signals. In the case of HP ^{13}C MRI, a train of sub-pulses with modulated $\mathbf{B_1}$ with an alternating slice selective gradient is applied simultaneously. The spatial selectivity is determined by individual sub-pulses, while the delay between each sub-pulses and the duration and shape of the B_1 envelope determine spectral selectivity[6].

2.1.4 Relaxation

Relaxation refers to the returning of the spins back to their equilibrium state. Once the magnetization is excited and is tipped away from the z-direction, and once the RF pulse is turned off, the spins would have to realign with the axis of the static magnetic field by giving up all their excess energy[8]. The experience of the spins to return to its original state is what we call relaxation. The relaxation process could be characterized by two different relaxation time constants, T_1 and T_2.

T_1 relaxation is also called the longitudinal relaxation[1,8], or the spin-lattice relaxation time because it refers to the time it takes for the spins to give the energy obtained from the RF pulse back to the surrounding lattice in order to go back to their equilibrium state[8]. It describes how fast the longitudinal magnetization, M_z, is restored after being tipped to the transverse plane[1,8]. This recovery process can be mathematically described as[1,8]:

$$\frac{dM_z}{dt} = -\frac{M_z - M_0}{T_1} \tag{2.10}$$

where $\mathbf{M_0}$ is the magnetization at equilibrium along the z-direction, the solution to the above first order differential equation is:

$$M_z = M_0 + (M_z(0) - M_0)e^{-\frac{t}{T_1}} \tag{2.11}$$

After a 90° RF excitation, $\mathbf{M}_z(0)$ would be 0, thus:

$$M_z = M_0(1 - e^{-\frac{t}{T_1}}) \tag{2.12}$$

The other relaxation time constant, T_2, which is also called spin-spin relaxation time[1,8], and it is used to describe how fast the transverse magnetization (M_{xy}) decays to equilibrium (0)[1,8]. This decay process can be mathematically described as:

$$\frac{dM_{xy}}{dt} = -\frac{M_{xy}}{T_2} \tag{2.13}$$

After a 90° RF excitation, $M_{xy}(0) = M_0$, the solution to the above first order differential equation is:

$$M_{xy} = M_0 e^{-\frac{t}{T_2}} \tag{2.14}$$

For the same tissue, the T_2 time constant is smaller than T_1 and is mainly independent of the magnetic field strength. Figure 2.6 below depicts the graphical description of the recovery process with T_1 and decay process with T_2 relaxation times after a 90° RF excitation.

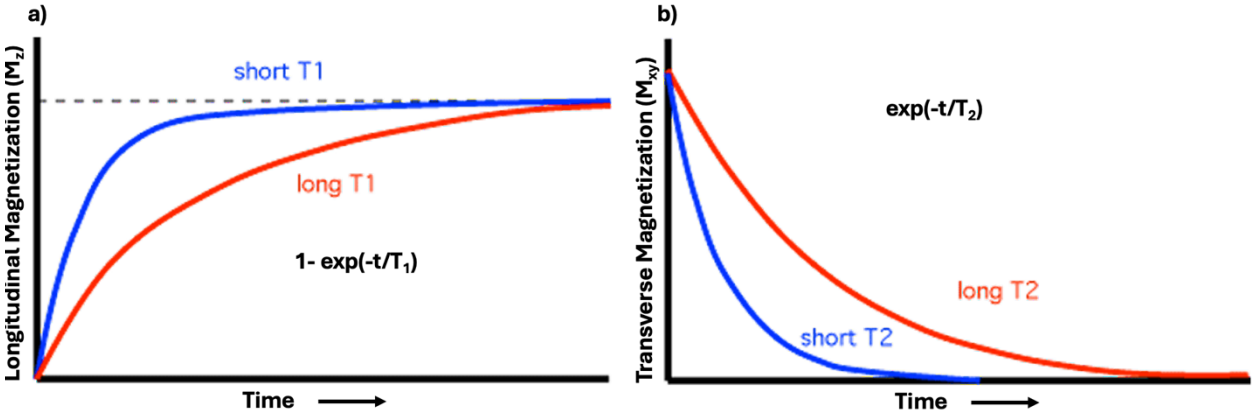

Figure 2.6: Depicts magnetization decay and recovery governing T_1 and T_2 relaxation processes. (a) Immediately after the RF pulse excitation, the longitudinal magnetization starts at 0 and gradually recovers to equilibrium $\mathbf{M}_0$ governed by the relaxation time T_1. (b) Immediately after the RF pulse excitation, the transverse magnetization starts at $\mathbf{M}_0$ and decays to zero. (Adapted from MRI Questions and Answers).

T_1 and T_2 are important and inherent tissue characteristics that provide MR image contrast. Thus, T_1 and T_2 are distinct for each biological tissue due to differences tissue properties and

microenvironments[1,8]. Table 2.2 summarizes T_1 and T_2 of some common tissue types at the 3 Tesla magnetic field strength.

Table 2.2: T1 and T2 values of some common tissues at 3 Tesla magnetic field.

Tissue	T_1(ms)	T_2(ms)
White matter	838	75
Gray matter	1607	83
Subcutaneous fat	365	133
Blood	1932	275
Kidney	1194	56
Liver	812	42

2.1.5 Bloch Equation with Chemical Exchange Modeling

The MR phenomenon of spin precession, spin-lattice relaxation, and spin-spin relaxation are mathematically described by the Bloch equation. This mathematical description is of profound significance in explaining the dynamics of nuclear magnetization, and can used to assist various computer simulations. The Bloch equation is:

$$\frac{d\boldsymbol{M}}{dt} = \boldsymbol{M} \times \gamma \boldsymbol{B} - \frac{M_x \boldsymbol{i} + M_y \boldsymbol{j}}{T_2} - \frac{(M_z - M_0)\boldsymbol{k}}{T_1} \tag{2.15}$$

where $\boldsymbol{M} = \left[M_x, M_y, M_z\right]^T$ is the magnetization vector, $\boldsymbol{B}$ is the magnetic field vector, γ is the gyromagnetic ratio of the nucleus, $\boldsymbol{B}$ is the magnetic field vector, t is time, $\boldsymbol{i}$, $\boldsymbol{j}$, and $\boldsymbol{k}$ are unit vectors in x, y, and z directions respectively, M_0 is the equilibrium magnetization, and T_1 and T_2 are the longitudinal and transverse relaxation time constants described in section 2.1.4. The magnetic field $\boldsymbol{B}$ is comprised of three types of magnetic fields: main static fields $\boldsymbol{B_0}$, radiofrequency fields $\boldsymbol{B_1}$

transmitted by coils for excitation, and linear gradient fields $\boldsymbol{G}$ for spatial encoding. The cross-product relationship ($\boldsymbol{M} \times \gamma \boldsymbol{B}$) phenomenologically describes the precession of $\boldsymbol{M}$ about $\boldsymbol{B}$ while the relaxation terms T_1 and T_2 describe the exponential behavior of both the longitudinal and transverse components of the magnetization. T_1 and T_2 relaxation effects can change the magnitude $\boldsymbol{M}$ but precessing does not change the magnitude of $\boldsymbol{M}$[1].

In order to accommodate the chemical exchange modeling[10,11], as it is of a tremendous interest for hyperpolarized ^{13}C MR imaging applications, the Bloch equation can be further modified. This chemical exchange results for the MR active nuclei to be in different environments which in turn leads to changes in chemical shift, coupling, and relaxation rates. For instance, assume two spin states, S_1 and S_2, with chemical exchange, their magnetization can be modeled as follows[10]:

$$\frac{d\boldsymbol{M_1}}{dt} = \boldsymbol{M_1} \times \gamma \boldsymbol{B} - R_1\left(\boldsymbol{M_1} - \boldsymbol{M_1(0)}\right) + k(\boldsymbol{M_2} - \boldsymbol{M_1})$$

$$\frac{d\boldsymbol{M_2}}{dt} = \boldsymbol{M_2} \times \gamma \boldsymbol{B} - R_2\left(\boldsymbol{M_2} - \boldsymbol{M_2(0)}\right) + k(\boldsymbol{M_1} - \boldsymbol{M_2}) \quad (2.16)$$

Where k is the apparent exchange rate between the two chemicals, and R_1 and R_2 are the full relaxation matrices for S_1 and S_2. It is important to note that most conversions are relatively slow, leading to two separate resonance peaks on the resulting spectrum for hyperpolarized ^{13}C applications.

2.1.6 Imaging Readout and Localization

MRI is an example of a Fourier Imaging modality that performs data acquisition in the frequency domain, which is also called the "k-space". MRI utilizes the three types of magnetic fields: the main static field $\mathbf{B_0}$, radiofrequency field $\mathbf{B_1}$ transmitted by coils for excitation, and linear gradient

fields $\boldsymbol{G}$ in the x, y, and z directions for spatial and temporal encoding. The mathematical derivation of the total received time MR signal s(t) and its relations to the spatial k-space frequencies can be described by integrating over the entire volume of interest (regions that are excited by the RF field)[1]:

$$s(t) = \iiint m(x,y,z)\, e^{-i\omega_0 t} e^{-i\gamma \int_0^t \boldsymbol{G}(\tau)\cdot \boldsymbol{r} d\tau}\, dx\, dy\, dz \tag{2.17}$$

where m is the excited magnetization, and **G** is the superimposed linear gradient field strength **G** = (G_x, G_y, G_z) in the x, y, and z directions. However, the $e^{-i\omega_0 t}$ in the above equation, is not of interest, thus[12]:

$$s(t) \propto \iiint m(x,y,z)\, e^{-i\gamma \int_0^t \boldsymbol{G}(\tau)\cdot \boldsymbol{r} d\tau}\, dx\, dy\, dz \tag{2.18}$$

$$s(t) \propto \iiint m(x,y,z)\, e^{-i2\pi[(k_x(t)x)+(k_y(t)y)+(k_z(t)z)]}\, dx\, dy\, dz \tag{2.19}$$

where

$$k_x(t) = \frac{\gamma}{2\pi}\int_0^t G_x(\tau)d\tau$$

$$k_y(t) = \frac{\gamma}{2\pi}\int_0^t G_y(\tau)d\tau \tag{2.20}$$

$$k_z(t) = \frac{\gamma}{2\pi}\int_0^t G_z(\tau)d\tau$$

Hence, 3D -Fourier transform of the excited magnetization m(x, y, z) would be:

$$\mathcal{F}_{3D}\big(m(x,y,z)\big) = M(k_x,k_y,k_z) \tag{2.21}$$

$$s(t) \propto \mathcal{F}_{3D}\big(m(x,y,z)\big) \tag{2.22}$$

where $\mathcal{F}_{3D}$ denotes the three dimensional (3D) Fourier transform. As depicted in equation 2.20, the spatial frequencies k_x, k_y, and k_z is proportional to the time integral of applied linear gradient field strengths in the x, y, and z directions. Equation 2.22 states, the received time signal s(t) could be re-

written in the form of a Fourier transform of the MRI signal $m(x, y, z)$. Then, the image can be reconstructed by performing an 3D- inverse Fourier transform of the received MR time signal from the k-space data:

$$m(x, y, z) \propto \mathcal{F}_{3D}{}^{-1}(s(t)) \tag{2.23}$$

where $\mathcal{F}_{3D}{}^{-1}$ denotes the three dimensional inverse Fourier transform. The relationship between k-space and image space is also explained by the Fourier theory. The spatial resolution (δ) is inversely proportional to the k-space coverage, while the field of view (FOV) is inversely proportional to the k-space point distance (Δk).

$$\delta = \frac{1}{N\Delta k} \tag{2.24}$$

where N is the number of acquired k-space points,

$$FOV = \frac{1}{\Delta k} \tag{2.25}$$

and

$$\Delta k = \frac{\gamma}{2\pi} G \Delta t \tag{2.26}$$

The gradient field strength **G** and the time difference Δt between each k-space point determines the distance between each k-space point. As discussed above, FIDs are acquired in *k*-space and Fourier transformed from spatial frequencies to images. Gradients spatially encode FIDs thereby traversing *k*-space. A standard 2D imaging sequence can thus be represented by a pulse sequence composed of the amplitude and timing of the RF pulse, gradient waveforms, and data acquisition (Figure 2.7).

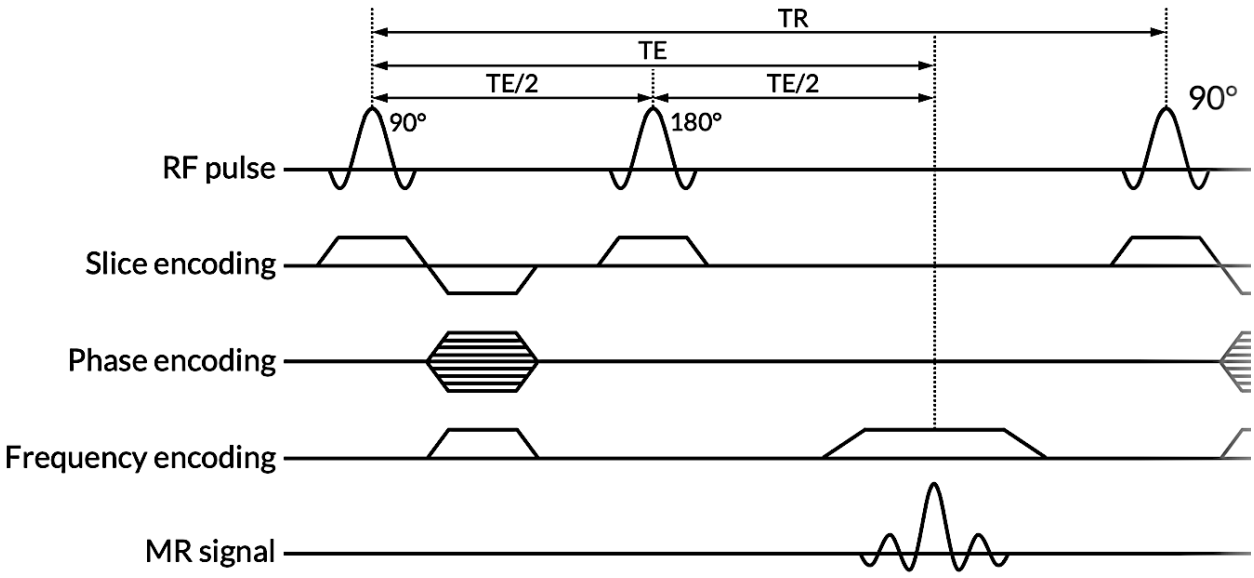

Figure 2.7: Depicts a generic spin-echo pulse sequence with a 90° RF pulse followed by a 180° pulse. The 180^0 pulse refocuses the dephasing spins. The slice, phase, and frequency encoding gradients (G_z, G_y, G_x) are depicted by three lines respectively. The MR signal is the bottom line. The time duration between the 90° pulse and the MR signal is the echo time (TE). The time duration between the first 90° RF pulse and the subsequent 90° RF pulse is the repetition time (TR). (Adapted from Lee et. al. 2022)

Repetition time (TR) is the time interval between two consecutive 90^0 RF pulse excitations[8]. TR determines the amount of T_1 relaxation that can occur before the next pulse[1,8]. T_1 contrast in the image can be affected by modulating the TR. Echo time (TE) is the time duration from the peak of the RF pulse to the moment when gradients traverse the center of *k*-space[1,8]. Gradients and their timing, TE, affects T_2 contrast in the image can be used to refocused nuclear spins[8].

Figure 2.8A depicts Echo-planar imaging (EPI) pulse sequence which allows fast imaging acquisition possible and of great interest for hyperpolarized ^{13}C imaging. EPI uses a spectral-spatial pulse that can selectively excite the molecules of interest based on frequency. Echo-planar spectroscopic imaging (EPSI) depicted in Figure 2.8B enables spectroscopic imaging for ^{13}C compounds acquisition in one spatial dimension and a spectroscopic dimension by performing a single readout during a rapidly switching frequency encoding gradient.

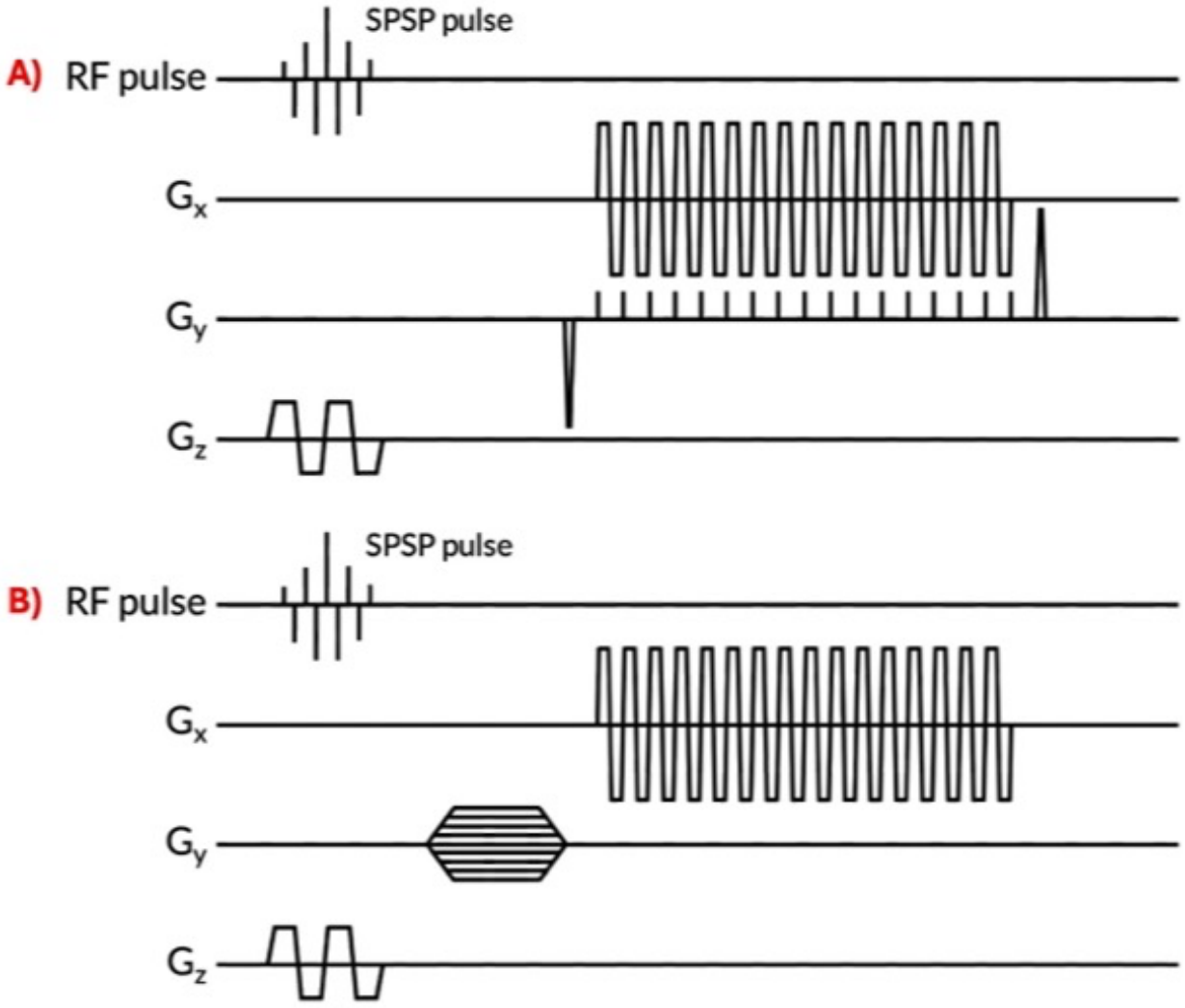

Figure 2.8: Shows some pulse sequences for rapid HP ^{13}C acquisitions. A). 2D multi-slice echo-planar imaging (EPI) pulse sequence with a spectral-spatial (SPSP) followed by a symmetric readout. B). 2D echo-planar spectroscopic imaging (EPSI) pulse sequence followed by a phase-encoding gradient.

2.2 Fundamentals of Magnetic Resonance Spectroscopy/Spectroscopy Imaging (MRS & MRSI)

In both research and clinical studies pertaining tissue metabolism, Magnetic Resonance Spectroscopy (MRS) and Magnetic Resonance Spectroscopic Imaging (MRSI) are profoundly crucial tools for non-invasive *in vivo* investigation. This section briefly discusses topics on chemical shift, MRSI, and specific examples of MRS will.

2.2.1 Chemical Shift

Chemical shift is a small displacement of the resonant frequency due to the shielding created by the orbital motion surrounding electrons in response to the main $\mathbf{B_0}$ field[1]. In NMR spectroscopy, chemical shift is the resonant frequency of an atomic nucleus relative to a standard in a magnetic field. Different chemical species create different electron microenvironments, even for the same nuclear species, and these different microenvironments lead to chemical shift differences on the nuclear magnetic resonance spectrum. Chemical shift is the shift of species happens as a result of the different microenvironment that is created by the different electron environments for each chemical species. These microenvironment differences are induced by electronegativity of nearby groups, which lead to magnetic shielding effects[3]. Thus, the nucleus would experience an effective magnetic field strength that can be mathematically described in the following equation:

$$B_{eff} = B_0 \cdot (1 - \sigma) \tag{2.27}$$

where σ is the shielding constant[3]. Thus, this nucleus' resulting resonant frequency can be described as:

$$\omega = \gamma B_{eff} = \gamma B_0 (1 - \sigma) \tag{2.28}$$

and the resulting relative chemical shift δ can be expressed as[3]:

$$\delta = \frac{\omega - \omega_{ref}}{\omega_0} \approx \sigma_{ref} - \sigma \tag{2.29}$$

where ω_{ref} is the resonance frequency of a reference peak and σ_{ref} is the shielding constant of a reference peak. The chemical shift, δ, is independent of the main magnetic field strength and often in the units of parts per million (ppm).

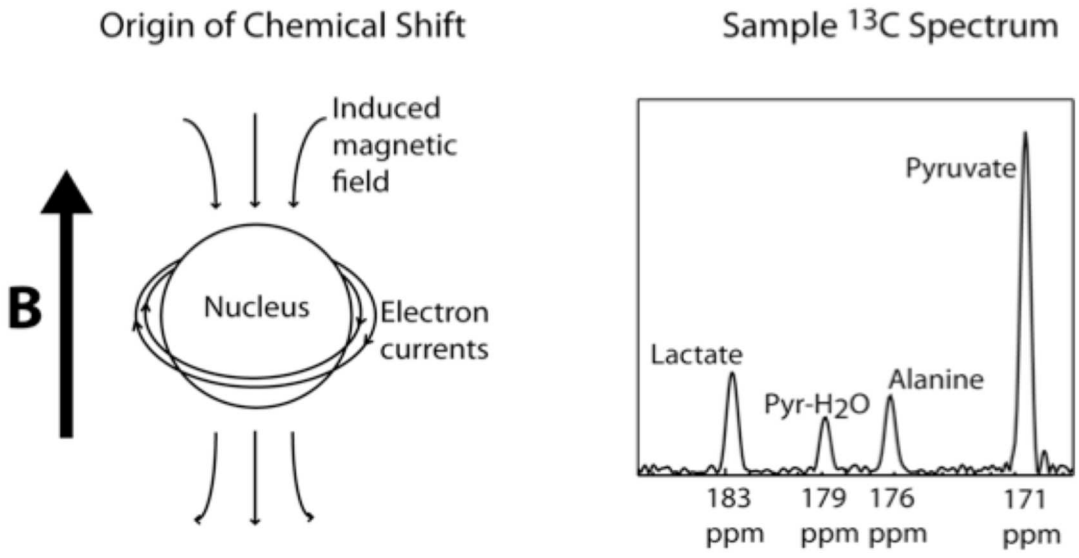

Figure 2.9: Chemical shift from an induced magnetic field in addition to the main field, resulting in a molecular dependent shift of the Larmor frequency. Sample HP 13C spectrum with chemical shifts. (Adapted from Swisher et al.[6]).

2.2.2 Magnetic Resonance Spectroscopic Imaging (MRSI)

To denote the chemical shift (spectral) dimension another variable, f, is used here, and to account for this dimension, the signal equation in equation 2.17 can be modified as follows:

$$s(t) \propto \int\int\int\int m(x,y,z,f)\, e^{-i2\pi[(k_x(t)x)+(k_y(t)y)+(k_z(t)z)+k_f f]}\, dx\, dy\, dz \qquad (2.30)$$

Where $k_f = t$ and k_x, k_y, and k_z are the same as equation 2.20. The signal equation (equation 2.30) above is a 4D Fourier transform of $m(x,y,z,f)$ when time *t* is denoted as k_f.

Thus, to acquire maps of spatially distributed chemical compounds both spatial localization and spectral encoding is required. Like the spatial dimension, the spectral dimension can also be described as follows.

$$\delta_f = \frac{1}{T_{acq}} = \frac{1}{N\Delta t} \qquad (2.31)$$

$$BW_{spectral} = \frac{1}{\Delta t} \tag{2.32}$$

where δ_f is the spectral resolution, T_{acq} is the time duration of spectroscopic readout, N is the number of points acquired, Δt is the sampling time, and $BW_{spectral}$ is the spectral bandwidth of the acquired spectrum.

2.3 Hyperpolarization

At thermal equilibrium, the nuclear spins of nuclei with rare natural abundance are relatively low and results in a very low sensitivity that is merely detectable for MR imaging. For instance, ^{13}C has a natural abundance of (1.1%) with a gyromagnetic ratio four-fold lower than ^{1}H, which makes imaging difficult and results at a low polarization at physiological conditions. Increasing the concentrations and sample volumes or acquisition strategies with time intensive signal averaging, wouldn't change the low sensitivity or low polarization. To increase the SNR of MR signal and to overcome the signal limit imposed by the Boltzmann's distribution of these nuclei with rare natural abundance, several methods have been proposed. One of the common hyperpolarization methods is dissolution dynamic nuclear polarization (dDNP).

Hyperpolarized (HP) ^{13}C MRI is an emerging molecular imaging modality based on an unprecedented gain in signal intensity of 10,000- to 100,000-fold that has been used to monitor uptake and metabolism of naturally-occurring biomolecules.[13,14] Thus, hyperpolarization via dynamic nuclear polarization amplifies the weak ^{13}C signal for a significantly enhanced SNR, but requires fast image acquisition techniques to capture the HP signal before it decays due to T_1 relaxation and metabolism.[14,15] Studies of HP ^{13}C-pyruvate imaging has shown the conversion of pyruvate to HP ^{13}C-lactate aligns with the Warburg effect in that increased pyruvate to lactate conversion is observed even

in the presence of oxygen in cancers due to oncogenic mutations and tumor microenvironment adaptation to promote proliferation.

2.3.1 Dissolution Dynamic Nuclear Polarization

As mentioned in section 2.1.2, because of the small difference in spin population distribution between different energy states at physiologic temperatures, the resulting polarization of these nuclei is really low, hence imaging these metabolites is challenging due to low SNR. Dissolution dynamic nuclear polarization (dDNP) is a technique that overcomes many of these challenges by providing over 10^4-fold signal enhancement enabling HP ^{13}C MR imaging[16]. Figure 2.10 depicts that dDNP drastically increasing the SNR by more than 10,000-fold[16].

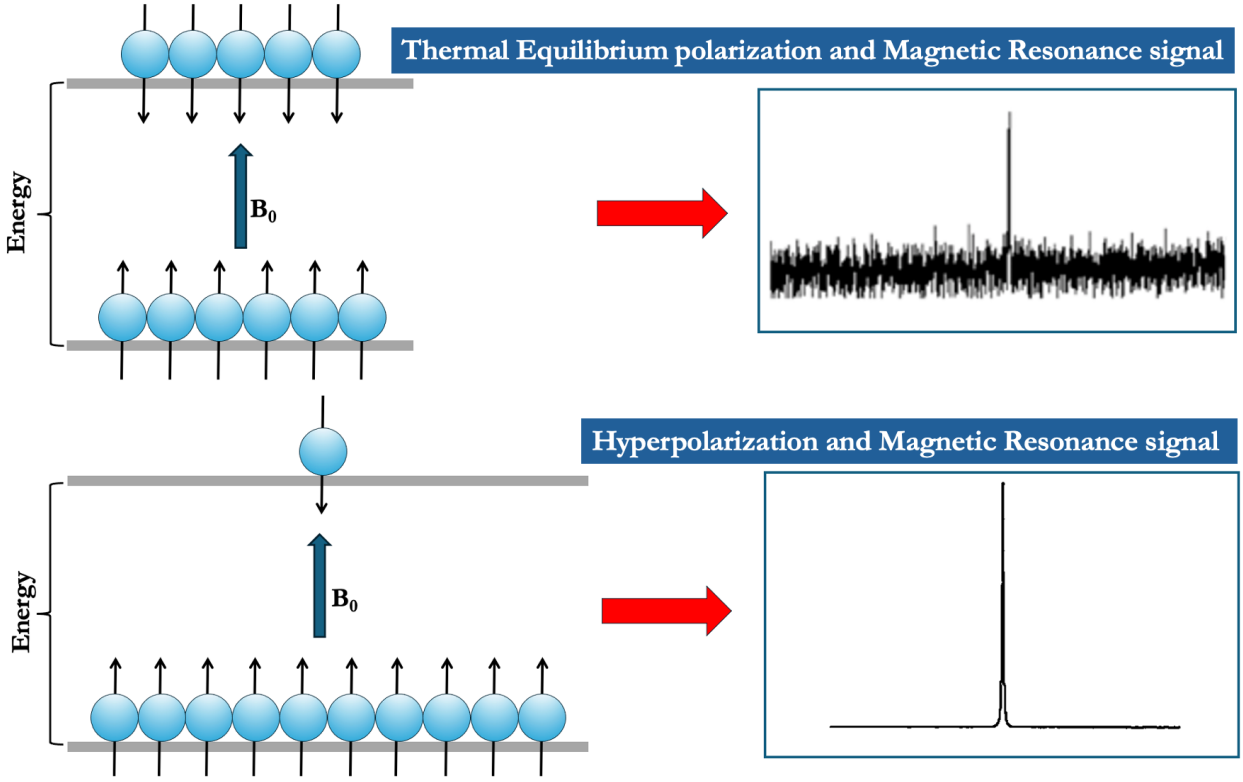

Figure 2.10: depicts comparison of the spin distribution with thermal polarization and hyperpolarization. dDNP creates perturbation of the spin populations between energy states and thereby increase the net magnetization and SNR by > 10,000-fold.

At a moderate magnetic field strength and liquid helium temperature, electron spins reach unity polarization as the magnetic moment of the electron is much higher than that of the proton[3]. When microwave irradiation is applied to the nuclei of interest placed in close proximity to unpaired electrons, the spin polarization transfer from the unpaired electrons to the nuclei of interest at a cryogenically low temperature and high magnetic field environment can occur. The nuclear spin polarization of ^{13}C could be increased to about ~50% in solid state at low temperature[3]. Figure 2.11 depicts the polarization transfer process from unpaired electrons to ^{13}C nuclei.

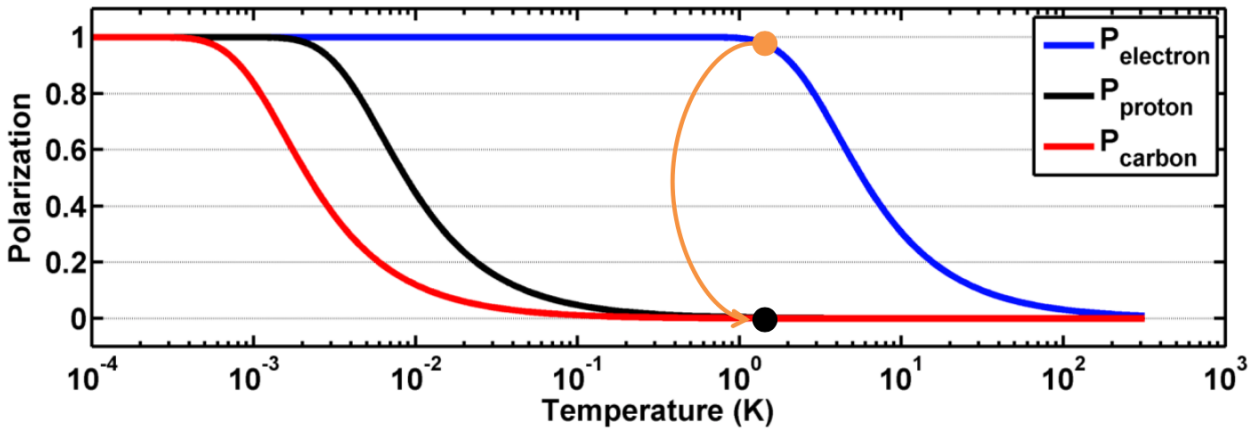

Figure 2.11: Polarization of electrons, proton, and carbon at a magnetic field over a range of temperatures. The polarization transfer happens at low temperature in the shaded area. Courtesy of Dr. Jeremy Gordon.

2.3.2 Hyperpolarized Imaging and Signal Decay

HP enables imaging of ^{13}C metabolites with their low gyromagnetic ratio and low *in vivo* concentration in a reasonable timeframe achievable. After the dDNP process, to bring the solid-state ^{13}C substrates to solutions with physiological pH and temperature, the superheated and pressurized dissolution media rapidly dissolves ^{13}C substrates. Then, the dissolved sample is transferred into the MR scanners for patients or animal experiments. However, As soon as the ^{13}C substrate leaves the polarizer, the longitudinal magnetization starts to relax to its thermal equilibrium[17-20]. Thus, to express the T_1 relaxation of the longitudinal magnetization M_z[21] equation 2.11 can be modified as follows:

$$M_z(t) = M_0 + (M_{z,HP} - M_0)e^{-\frac{t}{T_1}} \cong M_{z,HP}e^{-\frac{t}{T_1}} \quad (2.33)$$

where M_0 is the magnetization at thermal equilibrium, and $M_{z,HP}$ is the longitudinal magnetization right after the HP process.

The above equation 2.33 holds true if $M_{z,HP} >> M_0$. HP magnetization is non-renewable; thus, the use of this magnetization relies on efficacy and efficiency. Applying variable flip angles[22,23] and using efficient readout gradients[24,25] are some of the commonly used methods for efficient magnetization usage. As the signal (longitudinal magnetization) decays, each RF excitation consume the non-renewable magnetization discretely. Thus, the relaxation and RF excitation effects on the longitudinal and transverse magnetization after applying n RF excitations of the same flip angle α at time t can be described mathematically with the following equations:[13]

$$M_z(t) = M_{z,HP}e^{-\frac{t}{T_1}} cos^{n-1}\alpha \quad (2.34)$$

$$M_{xy}(t) = M_{z,HP}e^{-\frac{t}{T_1}} cos^{n-1}\alpha \, sin\alpha \quad (2.35)$$

As HP magnetization is non-renewable, signal averaging or experiments that require large flip angles ($\alpha = 90°$) are generally incompatible. Thus, proper calibration of RF power before injection and scanning is important. Hence, development of fast imaging sequence is a profound challenge. The two commonly used approaches for metabolic imaging to encode the spectral dimension are spectroscopic imaging (MRSI) and metabolic-specific imaging. For both of these methods, Cartesian (echo-planar) readout[26,28] and non-Cartesian (spiral and concentric rings) readout[27,29] could be applied. Figure 2.12 displays examples of a MRSI sequence and a metabolic-specific imaging sequence, along with their respective k-space trajectories.

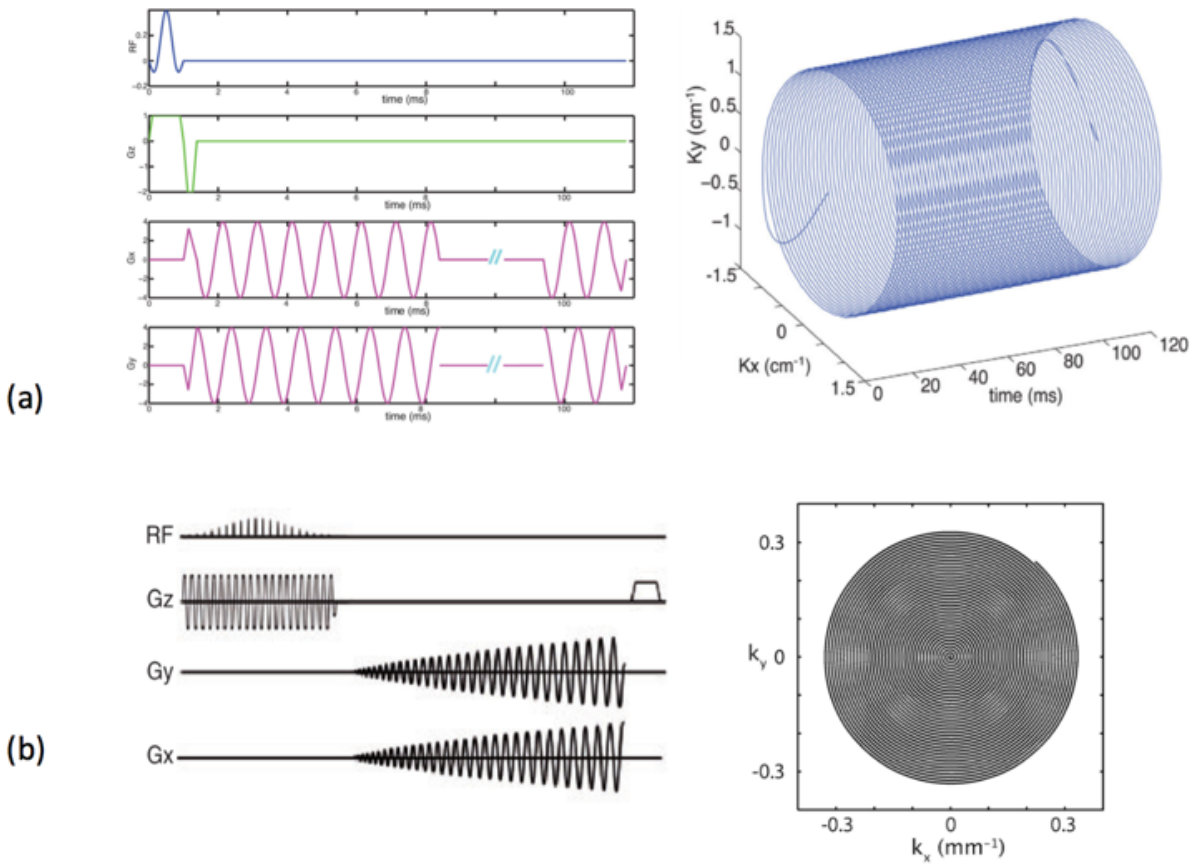

Figure 2.12: Shows examples of a spectroscopic and a metabolic-specific imaging sequence. (a) 3D trajectory showing the k-space readout of k_x, k_y, and k_f (time) directions for a spectroscopic imaging sequence with concentric ring readout. (b) A metabolic-specific imaging sequence with a selective RF pulse and spiral readout. As the RF pulse takes care of the spectral selection, only k_x and k_y directions are depicted in the k-space trajectory. (Adapted from Jiang et al[26], Gordon et al[21], and Lau et al[29]).

2.4 RF Coils

Radiofrequency (RF) coils are critical components of a MRI scanner by which the MRI signals are excited and received[30,31]. RF coils are the antennas that transmit and/or receive of the MRI system[30,31], and they play a crucial role in image quality such as signal-to-noise ratio (SNR), signal uniformity, and image resolution[31]. Fundamental understanding of use and safety issues of RF coils is imperative to utilize them in both research and clinical MRI, including knowledge of the basic principles of RF coils including coil designs and detailed schematics of RF receive coils[31]. To achieve the highest possible optimal image quality, prevent image artifacts, and reduce the risk of RF burns,

an educated selection of suitable RF coils for individual applications and proper use of RF coils are needed [31,33].

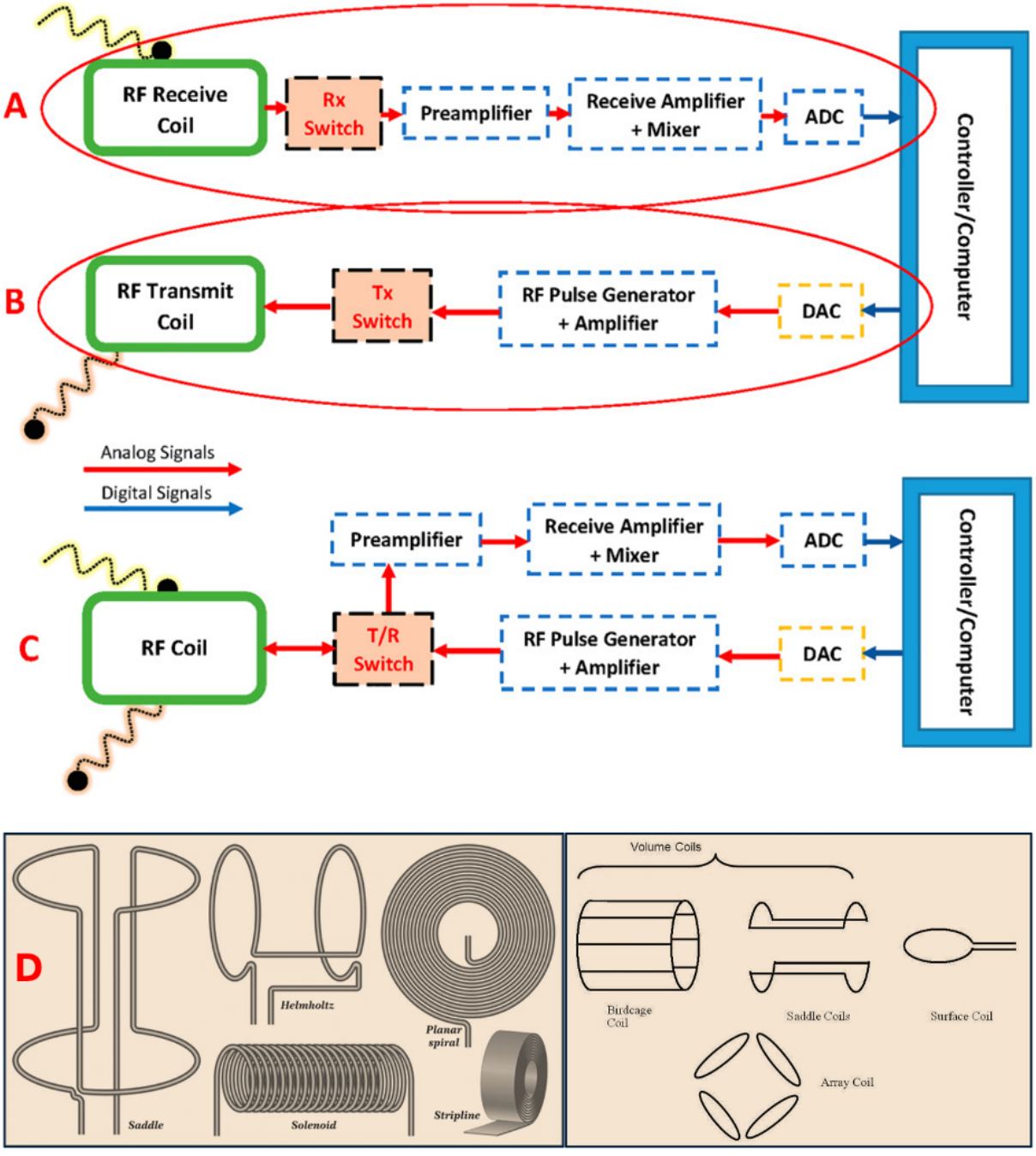

Figure 2.13: Schematics of different RF coils. (B) To excite the spins, the transmit coil receives a signal from the controller/computer via a digital-to-analog converter (DAC). (A) The receive coil then detects the response signals from the excitation, amplifies, and digitizes (ADC) the data. (C) The schematic of a transmit-receive RF coil: the T/R-switch controls the transmission and reception of RF signals. (D) Schematics of different RF coils. (A,B &C adapted from Gruber B. et. al. [31]).

2.4.1 Kinds of RF Coils

There are many types of RF coil designs, which may be classified from different aspects. RF coils generally have two functions: to excite the magnetization by broadcasting the RF power (Tx-Coil) and/or to receive the signal propagated from the excited spins (Rx-Coil)[31]. Thus, based on function, RF coils can be categorized into three: transmit only (Tx-coil), receive only (Rx-coil), and transmit and receive (Tx/Rx-coil) coils[31]. RF transmit (Tx) only coil generates an RF pulse and produces a small magnetic field perpendicular to the main static magnetic field B_0, which perturbs and rotates net magnetization away from its alignment with the main static magnetic field[31]. The RF receive (Rx) only coil detects the precessing nuclear spins resulting in an induced electric current via electromagnetic induction[31]. The induced current is the MR signal, and reflects the magnetizations from the tissue within the field of view (FOV) of the Rx-Coil. The Tx-Coils generate the electromagnetic B_1^+-field, which is perpendicular to the main (static) magnetic field B_0, and oscillates at the resonance frequency (Larmor Frequency, ω_0)[31]. As can be depicted from equation 2.5 the Larmor frequency ω_0 depends on the type of nucleus and the strength of the main magnetic field (i.e., 128 MHz for ^{1}H at 3T).

RF coils are also categorized into volume coils and surface coils[33]. Saddle, birdcage, and solenoid RF coils are volume coils that are designed to surround the body region and offer high signal sensitivity and uniformity[33]. A surface coil is a basic form of RF coil design that consists of a single conductive loop[30]. Surface coils provide strong signal close to the coils as coupling to the body is stronger, and signal decreases with distance from the coil[30-33]. Although smaller surface coils have stronger proximal signal, but it drops off faster than that of larger surface coils[30]. Surface coils also receive sample noise only from the sensitive volumes of the coils (noise filtering effect) and thus have higher SNR than volume coils[30], as they are in close proximity to the sample than that of volume coils.

Surface coils are usually used only as receive coils and not as transmit coils, as they generate inhomogeneous B_1 field outside of the center plane of their coil, and that could cause spatial variation in the RF flip angle leading to changes in image signal and contrast[30]. Although surface coils are placed as closely as possible to the area of interest to optimize signal reception[33,34], regions further away from surface coils have lower SNR and their signal uniformity is compromised. The phased-array RF coils combine the benefits of both types[33,34]. Phased-array RF coils comprised of several small independent surface coils, each having its own preamplifier and RF receiver channel and the elements are carefully positioned to minimize mutual interactions (aka coupling) while receiving signals simultaneously[33,34].

Saddle coils have cylindrical bodies with one or more turns of wire or foil on each side. Saddle coils generate a very homogenous field in the direction of its along axis, and they are suited for experiments on nuclei with low gyromagnetic ratios and when an axial sample access is required[35]. There are different developments such as folded Litz-foil Saddle coils or Etched Litz-foil saddle coils[33-35]. The basic element of a Litz coil is a wire that provides two parallel paths to the current[35]. Although Litz wire is efficient at low frequencies, it losses its quality at frequency above 2MHz[35]; hence, Litz foil Saddle coils are generally used below ~3MHz. Thus, informed specification, design and construction, evaluation, and application of properly selected RF coils are all critical to a safe and successful MRI scan[30].

2.4.2 Development of a RF coil

Once the selection of the desired coil is made depending on function and structure, and all considerations are in perspective including the materials: the ultimate goal is always to develop a coil that enhances the signal-to noise ratio (SNR) and reduce imaging time. Thus, following all the steps and making sure the coil is safe are crucial. A coil normally comprises of a coil element (a loop),

inductors and capacitors, diodes, chokes, baluns, preamplifiers. Doing simulations help us decide on the size and shape of the RF coils we intend to build. For instance, shown in Figure 2.14 shows a simulation of simple circular surface coils with different diameter sizes and the expected magnetic field strength versus position of targeted sample or organ. This simulation utilized the Biot-Savart law of magnetostatics which states that when a loop of radius R carries a current I the magnetic field strength at a position z from the center of the loop can be expressed as follows:

$$B_1(z) = \frac{\mu_0}{4\pi}\frac{2\pi R^2 I}{(z^2+R^2)^{3/2}} \tag{2.36}$$

This simulation depicts that when the target position is short distance from the center of the loop, smaller size coils result in a stronger magnetic field, but the strength dies quickly. Thus, when the target position is at a longer distance from the loop larger size loops are preferrable.

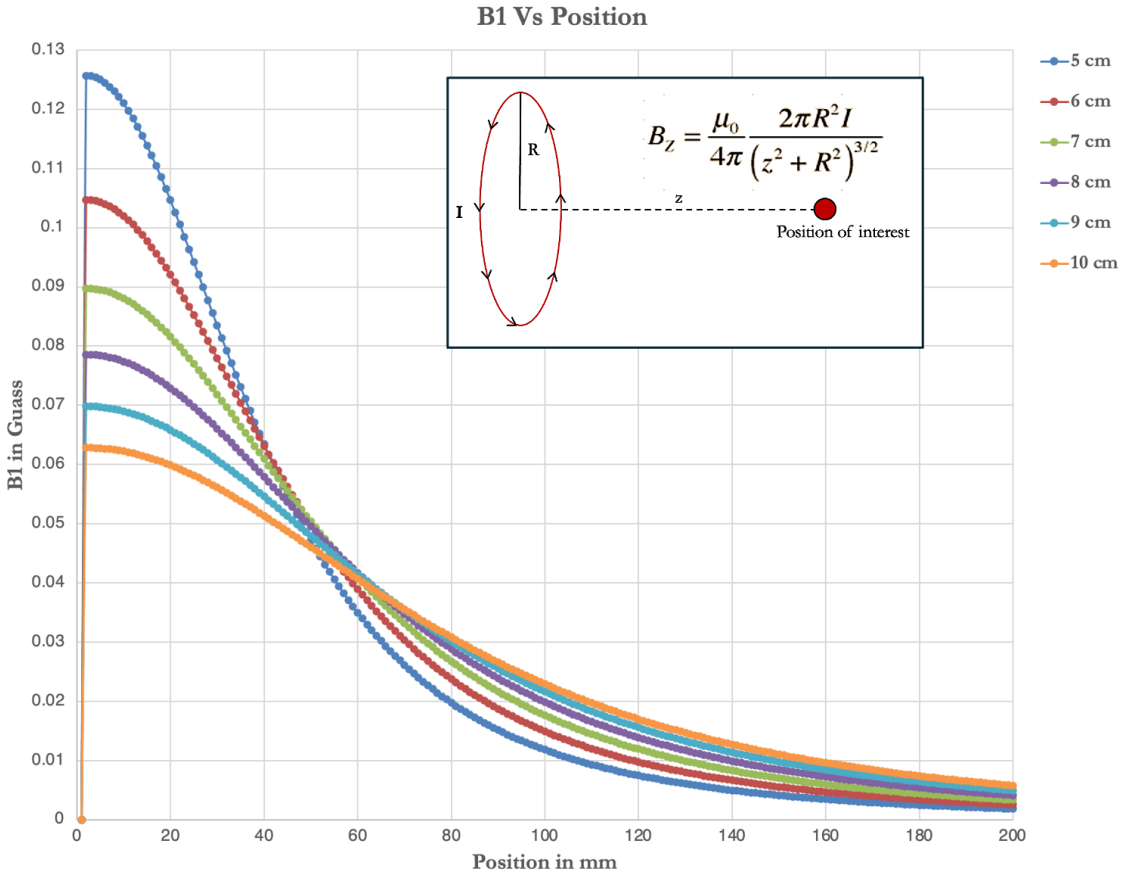

Figure 2.14: Simulation of different loop radii and their respective magnetic field strength versus position using Biot-Savart law of magnetostatics.

The first step would be to make sure the LC loop is to the desired size and with a desired frequency. Since RF coils are conductive wires with inductors and capacitors, measure or calculate the inductance of the loop wire and using this value calculate the capacitance needed to reach obtain the resonance frequency. The frequency at which the RF coil operates is resonance frequency and can be expressed as follows:

$$\omega_r = \frac{1}{\sqrt{LC}} = 2\pi f_r \tag{2.37}$$

Where ω_r is the resonance frequency in Hz, L is the inductance and C is the capacitance. Equation 2.37 enables you to determine the required values of the capacitor and inductor to construct the conductive wire loop to the desired resonance frequency. Once tuned to the working frequency, the coil needs to be matched with the transmission cable which usually is around 50Ω.

Once the coil elements are fully tuned and matched, coil testing follows. One determinant normally used to tell coil efficiency is the quality factor usually called as Q factor. Q factor is expressed as follows:

$$\mathrm{Q} = \frac{\omega L}{R} = \frac{Maximum\ Energy\ Stored}{Avg\ Energy\ Dissipated\ per\ Cycle} \tag{2.38}$$

$$Q_{ratio} = \frac{Q_{unloaded}}{Q_{loaded}} = \frac{R_{coil} + R_{sample}}{R_{coil}} \tag{2.39}$$

Where, ω is the resonance frequency, L is the inductance of the coil and R is the resistance of the coil. R_{coil} is the resistance of the coil, and R_{sample} is the resistance of the sample.

If Q factor of a coil is > 2, the coil is good which means most of the noise is coming from the sample and the losses in the coil are minimal or $R_{sample} >> R_{coil}$. Q factor (quality factor) refers to the efficiency in minimizing signal loss caused by the sample, essentially indicating the efficiency of the coil in capturing the MR signal[32,33]. A high Q factor achieves a higher signal-to-noise ratio (SNR).

Tissue-emitted MR signals are very weak, requiring effort to maximize signal detection[31]. The filling factor refers to how well a given RF coil geometry matches the anatomy of the area of interest in size and shape[31]. An RF coil that has a high filling factor samples a comparatively large volume of tissues of interest for a given volume of the coil, and hence detects more signal and less noise[32].

2.5 References

1. Nishimura DG. *Principles of Magnetic Resonance Imaging*. Stanford University; 2010.
2. Prince JL, Links JM. *Medical Imaging Signals and Systems*. Pearson Prentice Hall; 2008.
3. Schroder L, Faber C. *In Vivo NMR Imaging - Methods and Protocols*. Springer Nature Link; 2011.
4. McRobbie DW, Moore EA, Graves MJ, Prince MR. *MRI From Picture to Proton*. 3rd edition, Cambridge University Press, New York; 2007.
5. Larson PEZ, Kerr AB, Chen AP, Lustig MS, Zierhut ML, Hu S, Cunningham CH, Pauly JM, Kurhanewicz J, Vigneron DB. Multiband Excitation Pulses for Hyperpolarized ^{13}C Dynamic Chemical Shift Imaging. J. Magn. Reson. 2008; 194(1):121-127. PMCID: PMC3739981
6. Swisher CL. Hyperpolarized 13C Magnetic Resonance Spectroscopic Acquisition and Reconstruction. 2014.
7. Larson PEZ, Hu S, Lustig M, et al. Fast dynamic 3D MR spectroscopic imaging with compressed sensing and multiband excitation pulses for hyperpolarized 13C studies. *Magn Reson Med*. 2011;65(3):610-619. doi:10.1002/mrm.22650.
8. Hashemi RH, Lisanti CJ, Bradley WGJ. *MRI: The Basics*. Wolters Kluwer; 2018.
9. Park IW. Improving Brain Tumor Characterization and Management Using 1 H and Hyperpolarized 13C Magnetic Resonance Spectroscopic Imaging. 2010.
10. Abergel D, Palmer AG. Approximate Solutions of the Bloch-McConnell Equations for Two-Site Chemical Exchange. *ChemPhysChem*. 2004;10032(5):787-793. doi:10.1002/cphc.200301051.
11. Mcconnell HM. Reaction Rates by Nuclear Magnetic Resonance. *J Chem Phys*. 1958;1958(28):430-431. doi:10.1063/1.1744152.
12. Jiang W. Rapid and Robust Non-Cartesian Magnetic Resonance Imaging Methods. 2016.

13. Larson PEZ, Chen HY, Gordon JW, et al. Investigation of analysis methods for hyperpolarized 13C-pyruvate metabolic MRI in prostate cancer patients. *NMR Biomed.* 2018;31(11):e3997. doi:10.1002/nbm.3997

14. Nelson SJ, Kurhanewicz J, Vigneron DB, Larson PEZ, Harzstark AL, Ferrone M, van Criekinge M, Chang JW, Bok R, Park I, Reed G, Carvajal L, Small EJ, Munster P, Weinberg VK, Ardenkjaer-Larsen JH, Chen AP, Hurd RE, Odegardstuen L-I, Robb FJ, Tropp J, Murray JA. Metabolic Imaging of Patients with Prostate Cancer Using Hyperpolarized [1-^{13}C]Pyruvate. Science Translational Medicine. 2013; 5(198): 198ra108. PMCID: PMC420104

15. Aggarwal, R., Vigneron, D. B., & Kurhanewicz, J. (2017). Hyperpolarized 1-[^{13}C]-Pyruvate Magnetic Resonance Imaging Detects an Early Metabolic Response to Androgen Ablation Therapy in Prostate Cancer. *European urology*, *72*(6), 1028–1029. https://doi.org/10.1016/j.eururo.2017.07.022

16. Ardenkjær-larsen JH, Gram A, Hansson G, et al. Increase in signal-to-noise ratio of > 10 , 000 times in liquid-state NMR. *Proc Natl Acad Sci U S A.* 2003;100(18):10158-10163.

17. Månsson S, Johansson E, Magnusson P, et al. C imaging — a new diagnostic platform. *Eur Radiol.* 2006;16(2006):57-67. doi:10.1007/s00330-005-2806-x.

18. Olsson LE, Chai C, Axelsson O, Karlsson M, Golman K, Petersson JS. MR Coronary Angiography in Pigs With Intraarterial Injections of a Hyperpolarized 13 C Substance. *Magn Reson Med.* 2006;55:731-737. doi:10.1002/mrm.20847.

19. Golman K, Petersson JS. Metabolic imaging and other applications of hyperpolarized 13C. *Acad Radiol.* 2006;13(8):932-942. doi:10.1016/j.acra.2006.06.001.

20. Ishii M, Emami K, Kadlecek S, et al. Hyperpolarized 13 C MRI of the Pulmonary Vasculature and Parenchyma. *Magn Reson Med.* 2007;57:459-463. doi:10.1002/mrm.21168.

21. Gordon JW, Larson PEZ. Pulse Sequences for Hyperpolarized MRS. *eMagRes*. 2016:1229-1246. doi:10.1002/9780470034590.emrstm1451.

22. Maidens J, Gordon JW, Arcak M, Larson PEZ. Optimizing Flip Angles for Metabolic Rate Estimation in Hyperpolarized Carbon-13 MRI. *IEEE Trans Med Imaging*. 2016;35(11):2403-2412. doi:10.1109/TMI.2016.2574240.

23. Xing Y, Reed GD, Pauly JM, Kerr AB, Larson PEZ. Optimal variable flip angle schemes for dynamic acquisition of exchanging hyperpolarized substrates. *J Magn Reson*. 2013;234:75-81. doi:10.1016/j.jmr.2013.06.003.

24. Cunningham CH, Vigneron DB, Chen AP, et al. Design of flyback echo-planar readout gradients for magnetic resonance spectroscopic imaging. *Magn Reson Med*. 2005;54(5):1286-1289. doi:10.1002/mrm.20663.

25. Schmidt R, Laustsen C, Dumez J, et al. In vivo single-shot 13 C spectroscopic imaging of hyperpolarized metabolites by spatiotemporal encoding. *J Magn Reson*. 2014;240(2014):8-15. doi:10.1016/j.jmr.2013.12.013.

26. Jiang W, Lustig M, Larson PEZ. Concentric rings K-space trajectory for hyperpolarized ^{13} C MR spectroscopic imaging. *Magn Reson Med*. 2014;00(2014):n/a-n/a. doi:10.1002/mrm.25577.

27. Gordon JW, Vigneron DB, Larson PEZ. Development of a symmetric echo planar imaging framework for clinical translation of rapid dynamic hyperpolarized 13C imaging. *Magn Reson Med*. 2017;77(2):826-832. doi:10.1002/mrm.26123.

28. Lau AZ, Chen AP, Ghugre NR, et al. Rapid multislice imaging of hyperpolarized 13C pyruvate and bicarbonate in the heart. *Magn Reson Med*. 2010;64(5):1323-1331. doi:10.1002/mrm.22525.

29. Vaunghan, J. T & Griffiths, J. R, RF Coils for MRI (JohnWiley and Sons Ltd.,2012)

30. Kwok WE. Basic Principles of and Practical Guide to Clinical MRI Radiofrequency Coils. Radiographics. 2022 May-Jun;42(3):898-918. doi: 10.1148/rg.210110. Epub 2022 Apr 8. PMID: 35394887.

31. Gruber B, Froeling M, Leiner T, Klomp DWJ. RF coils: A practical guide for nonphysicists. J Magn Reson Imaging. 2018 Jun 13;48(3):590–604. doi: 10.1002/jmri.26187. Epub ahead of print. PMID: 29897651; PMCID: PMC6175221.

32. Buchli, R., Saner, M., Meier, D., Boskamp, E.B. and Boesiger, P. (1989), Increased rf power absorption in MR imaging due to rf coupling between body coil and surface coil. Magn. Reson. Med., 9: 105-112. https://doi.org/10.1002/mrm.1910090112

33. G.M. Tse, D.K.W. Yeung, W.C.W. Chu, 3.13 - MRI of the Breast, Comprehensive Biomedical Physics, Elsevier, 2014, Pages 205-220, ISBN 9780444536334, https://doi.org/10.1016/B978-0-444-53632-7.00314-2.
(https://www.sciencedirect.com/science/article/pii/B9780444536327003142)

34. Roemer PB, Edelstein WA, Hayes CE, et al. The NMR phased array. Magn Reson Med. 1990; 16:192–225. [PubMed: 2266841]

35. Mispelter J, Lupu M, Briguet A. NMR probeheads for biophysical and biomedical experiments : theoretical principles & practical guidelines. London : Imperial College Press ; Singapore : Distributed by World Scientific Pub. Co., c2006.

Chapter 3: Development of New Endorectal Coil and Novel Methods for Improving Multiparametric MR-TRUS Guided Fusion Prostate Biopsies with Hyperpolarized C-13 Pyruvate Molecular Imaging

3.1 Introduction

Prostate cancer is one of the most common cancers in men and second leading cause of death cancer in the United States of America.[1] Prostate cancer is more likely to develop in older men and in non-Hispanic Black men.[1] According to the American Cancer Society's estimates for prostate cancer, about 248,530 new cases with about 34,130 deaths are from prostate cancer.[1] To reduce the mortality rates, early detection and diagnosis of prostate cancer is crucial.[2,3] Once detected, the aggressiveness and extent of the prostate cancer help determine the decision on how to manage prostate cancer.[8,13] However, this is difficult as prostate cancer has a vast biologic diversity and is treated with a broad spectrum of approaches from "active surveillance" to surgical, radiation-based, and other focal therapies.[8,13] Such therapies have trade-offs because, no matter how well they are delivered, resulting morbidities can severely impact quality of life.[13] Also, between 22 and 35% of men presenting with clinically advanced prostate cancer, who are treated with what was thought to be definitive radiation or surgery, suffer a posttreatment biochemical recurrence.[8,13] Conversely, many prostate cancers follow an indolent course that would not threaten the duration or quality of lives for the affected men, but identifying these not clinically-significant tumors is poorly accomplished using currently available prognostic data.[13,15,17,18] The ability to accurately predict outcome for individual patients and thereby select the most appropriate treatment is critically important, but is still an unmet, clinical need.[8,13]

Transrectal ultrasonography (TRUS)–guided biopsy can improve histopathologic diagnosis and grading of prostate cancer.[4,5,6] However, TRUS is limited for directly visualizing and targeting prostate lesions and therefore the fusion of magnetic resonance (MR) images with US overcomes many of these limitations but does not provide metabolic information on cancer aggressiveness or extent.[4,5,7,8] Although noninvasive imaging is used widely in the clinical management of prostate cancer, conventional techniques have limited value for assessing cancer aggressiveness and therapeutic response. There is no clinically approved modality that provides the critical information about how an individual cancer will behave when treated and so therapy selection and monitoring is often sub-optimal.[13]

Hyperpolarized ^{13}C MRI is an emerging molecular imaging modality based on an unprecedented gain in signal intensity of 10,000- to 100,000-fold that has been used to monitor uptake and metabolism of endogenous biomolecules.[9,13] Hyperpolarization via dynamic nuclear polarization amplifies the weak C-13 signal for a significantly enhanced SNR, but requires specialized rf coils tuned to the ^{13}C-frequency (32MHz at 3T instead of 128MHz) and fast image acquisition techniques to capture the HP signal before it decays due to T1 relaxation and metabolism.[13,17] Preclinical and recent clinical research HP ^{13}C-pyruvate MRI studies have shown that the conversion of pyruvate to its metabolites (specifically to ^{13}C-lactate) reflects the metabolic reprogramming known as the Warburg effect in that increased pyruvate to lactate conversion is observed even in the presence of oxygen in prostate cancers due to oncogenic mutations and tumor microenvironment adaptation to promote proliferation.

Multiparametric MRI (mpMRI) plays an ever-increasing role in the management of patients with suspicion of prostate cancer. Apart from local staging and estimation of cancer aggressiveness,

the detection and localization of prostate cancer foci have become important aspects in the diagnostic workup of men with suspected prostate cancer. In particular, excluding clinically significant cancer in a noninvasive matter may allow for significant reduction of prostatectomies and systematic or targeted biopsies in patients with elevated prostate specific antigen (PSA).

Although external coils are usually adequate for routine ^{1}H clinical studies, specialized endorectal coils provide up to 10-fold higher sensitivity that can significantly benefit specialized prostate ^{1}H MRI exams including MR molecular imaging with HP C-13 MRI. The endorectal coil (ERC) is a surface coil that is inserted in the rectum, similarly to the widely used trans-rectal ultrasound (TRUS) probe, to enable improved prostate MRI. The original $^{1}H/^{13}C$ ERC[30] created 15 years ago has been used in hundreds of prostate cancer patient exams (Figures 3.1), but is limited by suboptimal geometry with the probe head being too large and the neck too short, residual RF coupling during transmit, limited direct disinfection in chemical bath, transmission cables did not have built-in RF blocks, and older preamps located ~154cm away from the probe in T/R box. To address the above-mentioned issues, this project was designed to construct a new dual-element $^{13}C/^{1}H$ ERC that, compared to prior designs, would provide substantially improved sensitivity, better rf isolation, and more robust reliability with improved electronics for hyperpolarized C-13 prostate MRI enabling more routine guidance of MRI-TRUS biopsies.

Accurate histopathologic diagnosis and grading of prostate cancer is critical for clinical management of this disease. Currently, transrectal ultrasonography (TRUS)–guided biopsy is considered the standard.[1,2,3] However, TRUS is quite limited for directly visualizing and targeting prostate lesions and therefore the fusion of MR images (with greatly improved soft-tissue contrast) with TRUS images overcomes many of these limitations[1,2]. However, conventional anatomic and

diffusion MRI does not provide metabolic information on cancer aggressiveness or response to therapy.[4,5,6] Recent studies have shown that hyperpolarized (HP) (1-^{13}C)-pyruvate MRI in a rapid 2-minute addition to MRI exams can detect metabolic reprogramming in prostate cancer improving the detection of aggressive cancers and response to therapy[8]. This project was designed to develop specialized hardware and software to enable multiparametric MR incorporating hyperpolarized (HP) ^{13}C-pyruvate MR molecular imaging for improved MR-TRUS fusion biopsy guidance.

Similar to transrectal ultrasound probes, endorectal MR coils can improve prostate tumor visualization on mpMR images by providing ~5 fold higher SNR and more detailed images from the prostate and surrounding structures as compared to external coils.[9,10,11,] Although current 3T MRI scanners with high performance body coils and new receive arrays enable fast throughput clinical exams of adequate quality, developments, multiple studies have shown superiority of using endorectal coil in acquiring images with better image quality over pelvic phased array coil or surface coil.[10,11,12] A recent 3T mpMRI study suggested higher sensitivity and positive predictive value for data acquired with an ERC coil compared to data acquired with a PPA coil.[19] However, there is the downside of comfort, tolerability and slower workflow resulting in longer exam times that comes with endorectal coils, but for HP C-13 studies they are required for optimal sensitivity and spatial resolution especially for MR-TRUS fusion biopsies.

The original ^{1}H/^{13}C ER coil has been used for establishing the safety & feasibility of HP ^{13}C prostate MRI for detecting aggressive prostate cancers based on significantly higher HP ^{13}C-pyruvate to lactate conversion rate constants (k_{PL})[9] and recently to guide biopsies in larger clinical trials. Using our original ^{1}H/^{13}C ERC, the first human HP ^{13}C MR clinical trial of 31 patients not only showed safety and feasibility but also the detection of occult prostate cancer[13]. While the original ^{1}H/^{13}C ERC

has been used in hundreds of prostate cancer patient exams and has helped improve resolution to 0.34cm^3, it is limited by suboptimal geometry with the probe head being too large and the neck too short, residual coupling during transmit, and older preamps & electronics. The original endorectal coil is also sub-optimal in terms of SNR, ease of use, performance, and robustness. In this project, the new endorectal coil was designed to address these prior limitations and enable new clinical trials applying HP ^{13}C MRI to improve prostate cancer clinical management.

3.2 Materials & Methods

To obtain the highest sensitivity HP ^{13}C & ^{1}H MRI data, address the issues with the original ERC, a new dual-element ^{13}C/^{1}H ERC was developed to better detect aggressive prostate cancers within the prostate[7,8,9]. The housing was designed with input from radiologists, urologist, nurses and MRI technologists to be optimally contoured to anatomy, with tolerability and size more similar to transrectal ultrasound (TRUS) probes, using computer design software (SolidWorks 2020) and commercially 3D printed by Stratasys. For the housing to be lightweight and durable, a high-performance polyetherimide (PEI) thermoplastic, strong 3D printing material that has high heat resistance with a low coefficient of thermal expansion ULTEM^{TM} 1010 resin was used. The housing probe was tested and validated for its water-resistant ability, and rf coupling interference before the circuitry was put in place (Figure 3.1).

The housing probe was designed to have a shorter head (1.0in wide x 3in long) to reduce patient discomfort and longer neck for ease of maneuver. The rectangular circuit box (2in x 4in x 1in) was also designed to hold a circuit board on which the pre-amplifiers are mounted. With this approach, all mechanical details were 3D modeled and 3D-printed faster and at lower cost compared to the extensive machine shop milling in making the original dual-element ^{13}C/^{1}H ERC[10].

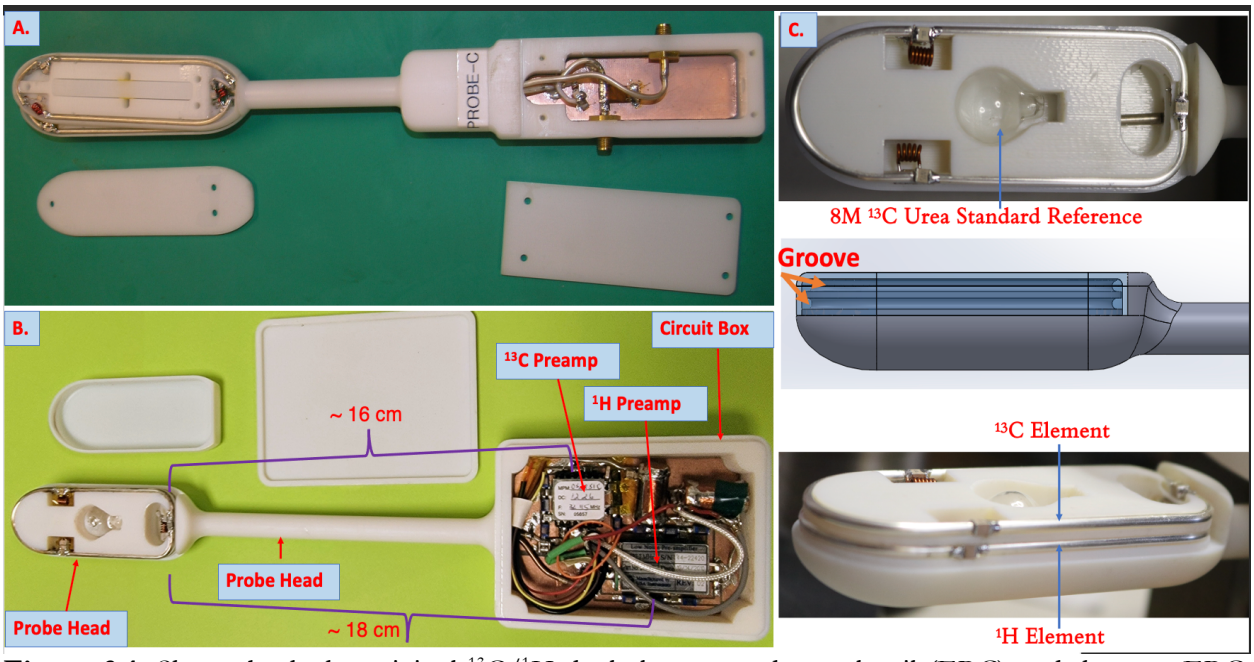

Figure 3.1: Shows both the original ^{13}C/^{1}H dual-element endorectal coil (ERC) and the new ERC. A.) The original ^{13}C/^{1}H dual-element ERC with its machined three layers Delrin housing. B.) The new ^{13}C/^{1}H dual-element ERC designed in SolidWorks (SolidWorks 2020) and commercial 3D printed housing. Both ^{13}C and ^{1}H preamps are about 16cm and 18cm away from the probe head. C.) The probe head with the ^{13}C and ^{1}H coils made with silver and placed in the grooves. The ^{13}C coil placed on the top as the sensitivity of ^{13}C is lower than ^{1}H.

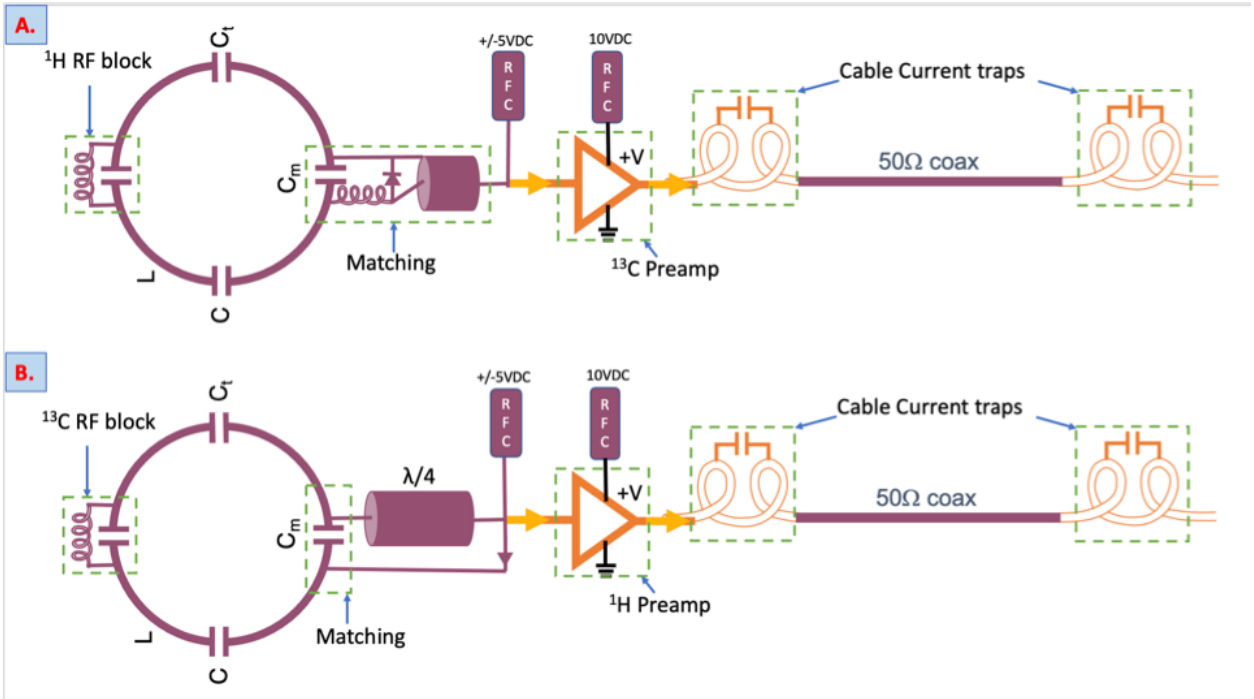

Figure 3.2: Circuit Schematics of both ^{13}C and ^{1}H coils of the new dual-element ^{13}C/^{1}H ERC. A.) Circuit schematics of the ^{13}C element of the new dual-element ^{13}C/^{1}H ERC. B.) Circuit schematics of the ^{1}H element of the new dual-element ^{13}C/^{1}H ERC.

For the ^{1}H element, low noise pre-amplifier with a frequency of 127.7MHz (USA Instruments, part no 2409871) and for ^{13}C element low noise amplifier with a frequency of 32.225MHz, gain=28.9dB, input impedance ~0Ω and output impedance of 52Ω (MPM, SN 05657) were utilized and preamplifiers were placed ~18cm and ~16cm from the probe in the circuit box(Figure 3.1B) respectively.

The ^{1}H and ^{13}C elements coil-loops were made using silver plated copper wire for optimal conductivity and fit in the groves on the probe head housing(Figure 3.1C). To obtain the highest sensitivity C-13 element is placed on top to be closer to the prostate as ^{13}C is less sensitive than ^{1}H. The proton element is detuned using the semi-rigid coaxial line connection to the pre-amplifier. The diode is located near the pre-amplifier and serves as pre-amplifier protection and active element detuning. For ^{13}C a normal trap circuit was built at the taping capacitor with a diode to ground to actively detune the element during transmit. NMR-compatible phantom with 8 molar solution of Gadolinium-doped (for shorter relaxation times) C13-urea in a 1cc spherical glass was constructed and placed at the center of the probe head for standard reference to ^{13}C scans (Figure 3.1C). To provide a clean DC bias for the preamps and to minimize coupling noise during amplification, 5-pole Butterworth lowpass filters with larger than 60dB loss and cutoff frequency of 4Hz for ^{13}C and ^{1}H preamps were implemented. Miniature parallel resonant (1/16 ") circuits was constructed and implemented in the loops of the elements for passively blocking ^{1}H frequency in the ^{13}C element and ^{13}C frequency in the ^{1}H prostate element. Every circuit element of both elements was then tuned & matched (Figure 3.2).

Two cable traps for the proton element were designed and placed at λ/4 (~38cm) distances apart. The length of the coaxial cable used was approximately the wavelength λ_H of the proton element with a dielectric media solid polyethylene (2.3). As the wavelength ^{13}C is almost quadruple of the ^{1}H,

the length of the coaxial transmission cable is almost quarter wavelength of ^{13}C ($\lambda_C/4$). The electrical measurement was ~573.14 degrees at 127.77MHz and ~11.327 degrees at 32.125MHz.

A Keysight/Agilent E5071C ENA Vector Network Analyzer was used to bench test the components and the two element coils. Phantom imaging was performed using 8mm isotropic echo-planar imaging (EPI) imaging with a 2s temporal resolution, FOV=24X24cm, slice thickness=10mm, matrix=16X16 on 3T GE MRI. For C-13 transmit a clamshell transmitter consisted of a Helmholtz pair built into the patient table was used.[9] For HP ^{13}C pyruvate active-surveillance prostate patient studies, the acquisition, analysis and image processing methods followed those described in Chen Hsin-Yu et al 2022[26].

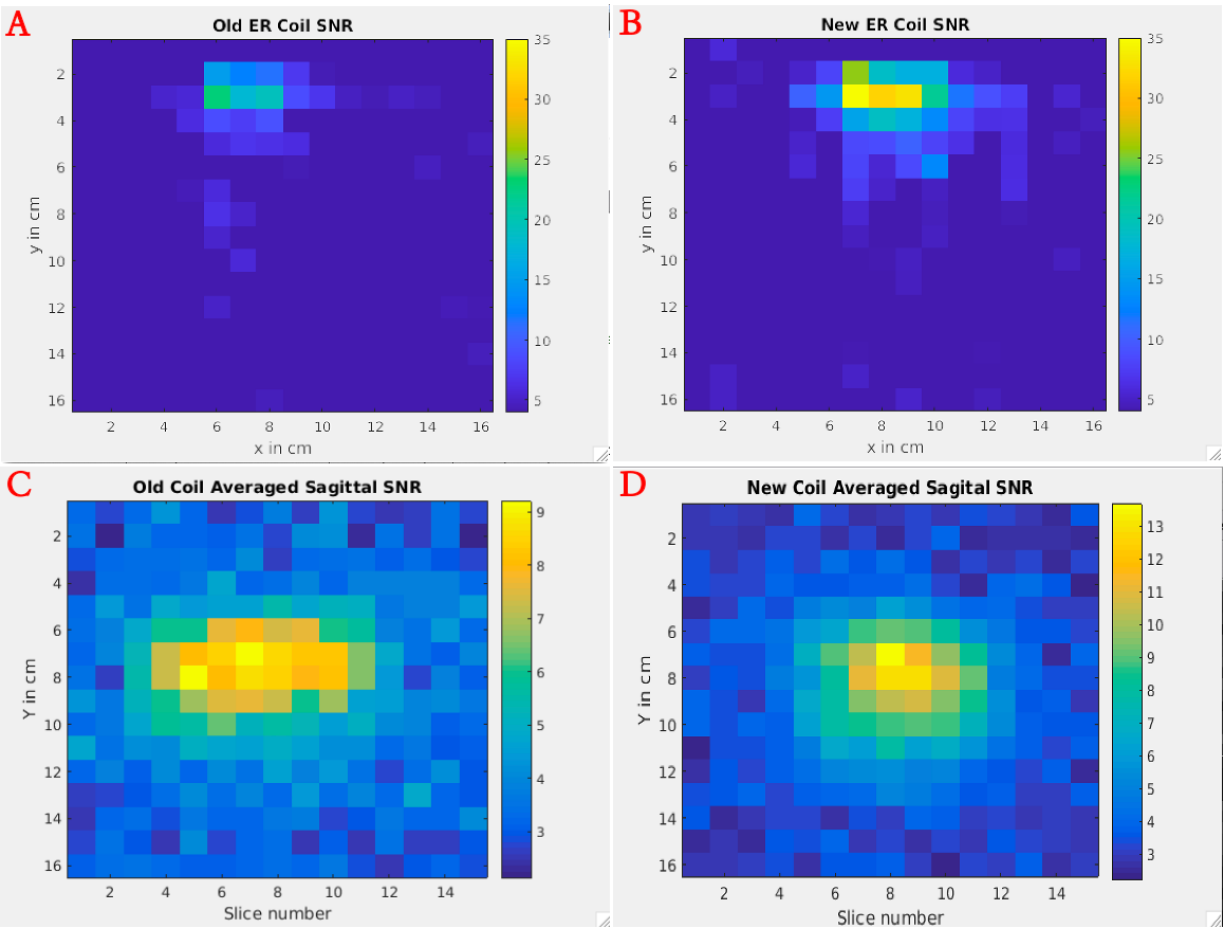

Figure 3.3: Normalized axial and sagittal phantom SNR images acquired using the original and new dual-element ^{13}C ERCs. A.) Axial SNR image of the original ERC. B.) Axial SNR image of the new ERC showing 60% improvement. C.) Sagittal SNR image of the original ERC. D.) Sagittal SNR image of the new ERC that demonstrated 80% improvement in SNR.

3.3 Results

The new $^{13}C/^{1}H$ endorectal coil (ERC) (Figures 3.1&3.2) provided an improved geometry for patient comfort/tolerance as compared to the prior design and demonstrated substantially improved ^{13}C and ^{1}H MRI sensitivity and with negligible rf coupling in bench electronic testing. $Q_{unloaded}$ for ^{1}H = 410, Q_{loaded} for ^{1}H = 42, $Q_{unloaded}$ for ^{13}C = 172, Q_{loaded} for ^{13}C = 55, resulting Q-factors 3.4 for the ^{13}C and ~10 for ^{1}H (Figure 3.7). The new ERC has satisfied the body noise dominance requirement which means most of the noise is from the sample.[3] The respective Q factors for the respective elements of the original coil is 1.5 and 2.8. The electrical bench testing using the Keysight/Agilent E5071C ENA Vector Network Analyzer showed that the voltage standing wave ratio (VSWR) of the new ERC is ~1.02 showing that the transmission loss is negligible, and the power transmission is ~100%. Phantom performance testing (Figure 3.3) of new ERC showed a 1.6-1.8-fold improvement in SNR compared to the original ERC.

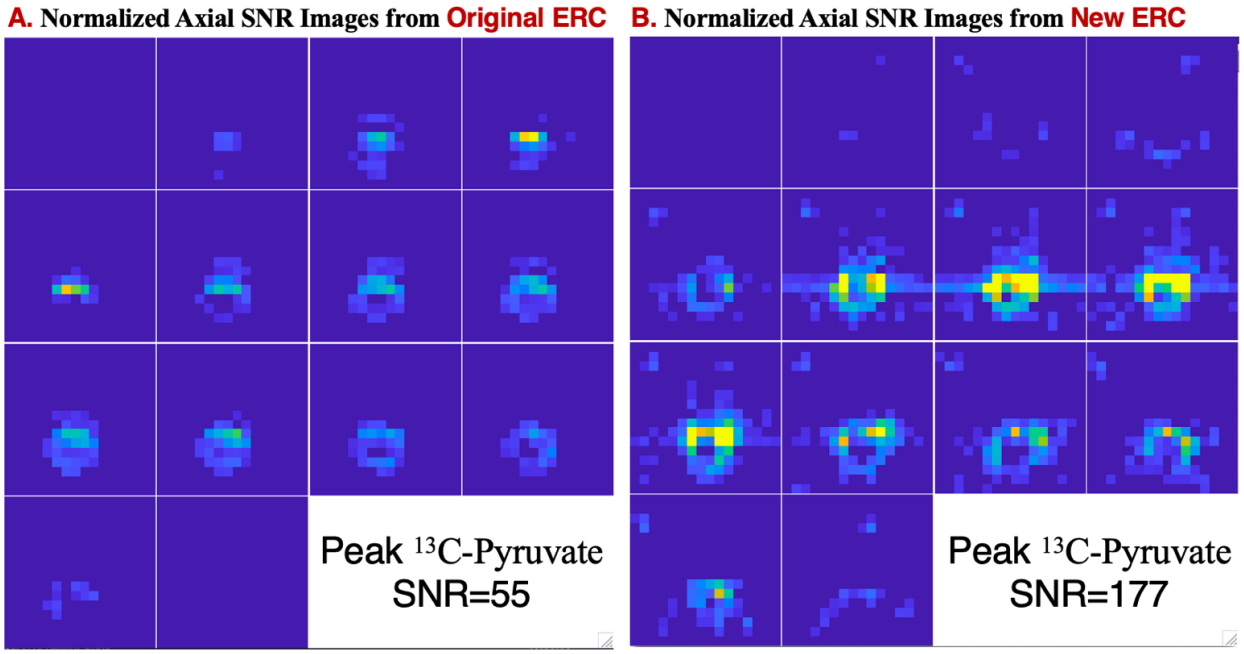

Figure 3.4: Normalized images acquired using the original and new ERCs from a representative active surveillance (AS) patient with serial HP C-13 scans. A). Slices from the initial study using the original ERC (Peak pyruvate SNR 55). B). Slices from a second study a year later using the new ERC developed in this project.

As shown in (Figure 3.4), the results from a patient study demonstrated not only feasibility for guiding HP ^{13}C mpMR-TRUS fusion biopsies, but also improvements in quantitative measures including signal-to-noise ratios (SNR). This representative patient was scanned using the original endorectal coil, external coils, and the new dual-element endorectal coil in a time span of a year (13 months). Qualitative and quantitative comparisons of the data acquired showed an improvement in SNR using the new ERC.

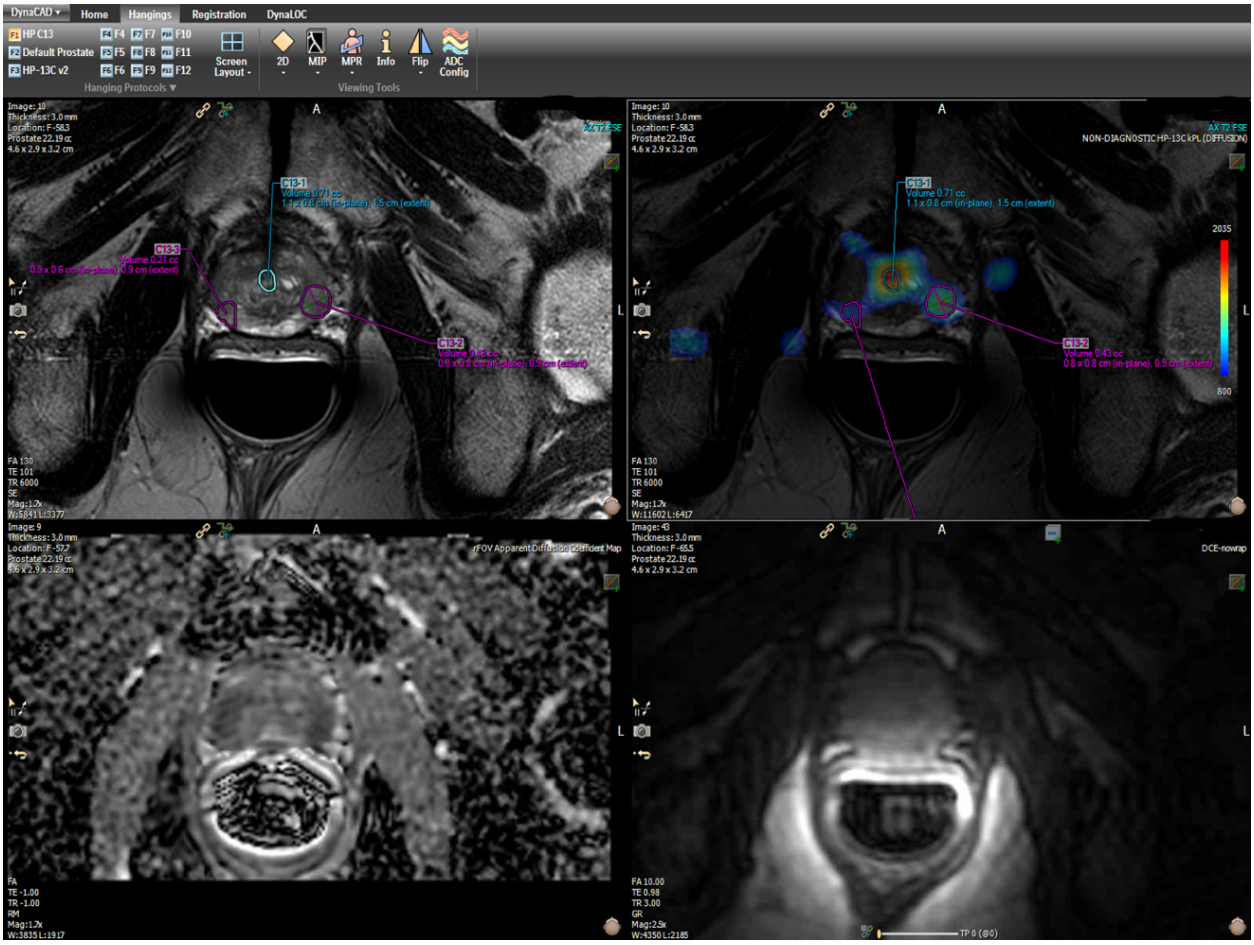

Figure 3.5: The images here are from a patient who was diagnosed with biopsy confirmed localized intermediate risk prostate cancer with Gleason 3+4 disease and PSA of 7.5. ^{1}H and HP ^{13}C k_{PL} color overlay images on PACS along with multiparametric evaluation from a radiologist.

The results from the new ERC on the same patient (Figure 3.4) showed substantial improvement with SNR greater than the phantom improvement of 1.8-fold. Three k_{PL} targets were

identified in this case (Figure 3.5), one of which aligned with the standard PIRADs and PSMA-PET lesion. The other two high k_{PL} targets did not have PIRADS correlation, indicating that HP ^{13}C k_{PL} values can provide unique metabolic information not depicted by current clinical proton imaging for guiding biopsies. As depicted in Figure 6 from the overlay of 2D CSI and proton imaging, the new ERC shows strong spectra with high SNR up to a depth of ~ 6cm and is in agreement with Biot–Savart law.

Table 3.1: Q factor values of both elements of the original and new ERCs obtained using a vector network analyzer (VNA).

ERC		$\mathbf{Q_{Unloaded}}$	$\mathbf{Q_{Loaded}}$	$\mathbf{Q_{ratio}}$
Original	^{1}H	177	64	2.8
	^{13}C	150	100	1.5
New	^{1}H	301	44	6.9
	^{13}C	172	55	3.4

3.4 Discussion

In this project, new methods to acquire and display ^{13}C-pyruvate to ^{13}C-lactate conversion rate constants (k_{PL}) images were developed and applied for guiding MR-US fusion biopsies in prostate cancer patients for the first time. The results from a patient scanned with both the new and original $^{13}C/^{1}H$ endorectal coil showed substantial SNR improvement greater than the phantom improvement of 1.8-fold. Three k_{PL} targets were identified in this case (Figure 3.5), one of which aligned with the standard PIRADs and PSMA-PET lesion. The other two high k_{PL} targets did not have PIRADS correlation, indicating that HP ^{13}C k_{PL} values can provide unique metabolic information not depicted by conventional proton imaging for guiding biopsies.

The new endorectal coil provided improved performance and safety. Electric currents can be induced by the $\mathbf{B}_1$ field on the cable shield of an RF coil or by unbalanced loop voltages coupled to the cable shield in a transmit-receive coil. Cable shield current can cause heating in the cable and lead to patient burns. The cable traps we installed along the cable of a receive or transmit-receive coil prevented cable shield currents. The traps consisted of parallel LC circuitry in the cable shield to block the current. Multituned RF coils are tuned to several resonance frequencies to detect signals from nuclei other than hydrogen. Having a multituned RF coil system enabled ^{13}C metabolic investigations without changing the RF coils and replacing the subject of interest, which also eliminates registration issues.

$$Q = \frac{\omega L}{R} = \frac{Maximum\ Energy\ Stored}{Avg\ Energy\ Dissipated\ per\ Cycle} \tag{3.1}$$

$$Q_{ratio} = \frac{Q_{unloaded}}{Q_{loaded}} = \frac{R_{coil} + R_{sample}}{R_{coil}} \tag{3.2}$$

Where Q is the quality factor, ω is the resonance frequency, L is the coil inductance, R is resistance of the coil. R_{coil} is the resistance of the coil, and R_{sample} is the resistance of the sample.

The Q_{ratio} of the new ERC are both higher than 2, which indicate that the coils met the design criteria, and most of the noise is from the sample resistance not from coil resistance.

3.5 Conclusion

This novel approach with the new dual-element $^{13}C/^{1}H$ ERC provided a substantial (~1.8-fold in phantom studies) increase in SNR and demonstrated the feasibility for guiding HP ^{13}C mpMR-TRUS fusion biopsies using k_{PL} maps for identifying aggressive cancers acquired as a 2-minute addition to standard-of-care MRI prostate exams. In addition, this new ERC demonstrated the safety and

feasibility of first hyperpolarized ^{13}C-MRI human study with injection of co-hyperpolarized [1-^{13}C]pyruvate and [^{13}C,$^{15}N_2$]urea.[31]

Table 3.2: Dissolution values and transfer time for 1- ^{13}C pyruvate injections performed on a representative patient that was scanned using both the original and new ERCs within a year.

ERC	Pol (%)	Tr Time (sec)	Concentration	↑ Pyr SNR
Original	31.7	NR	271mM	55
New	34.1	45	252	177

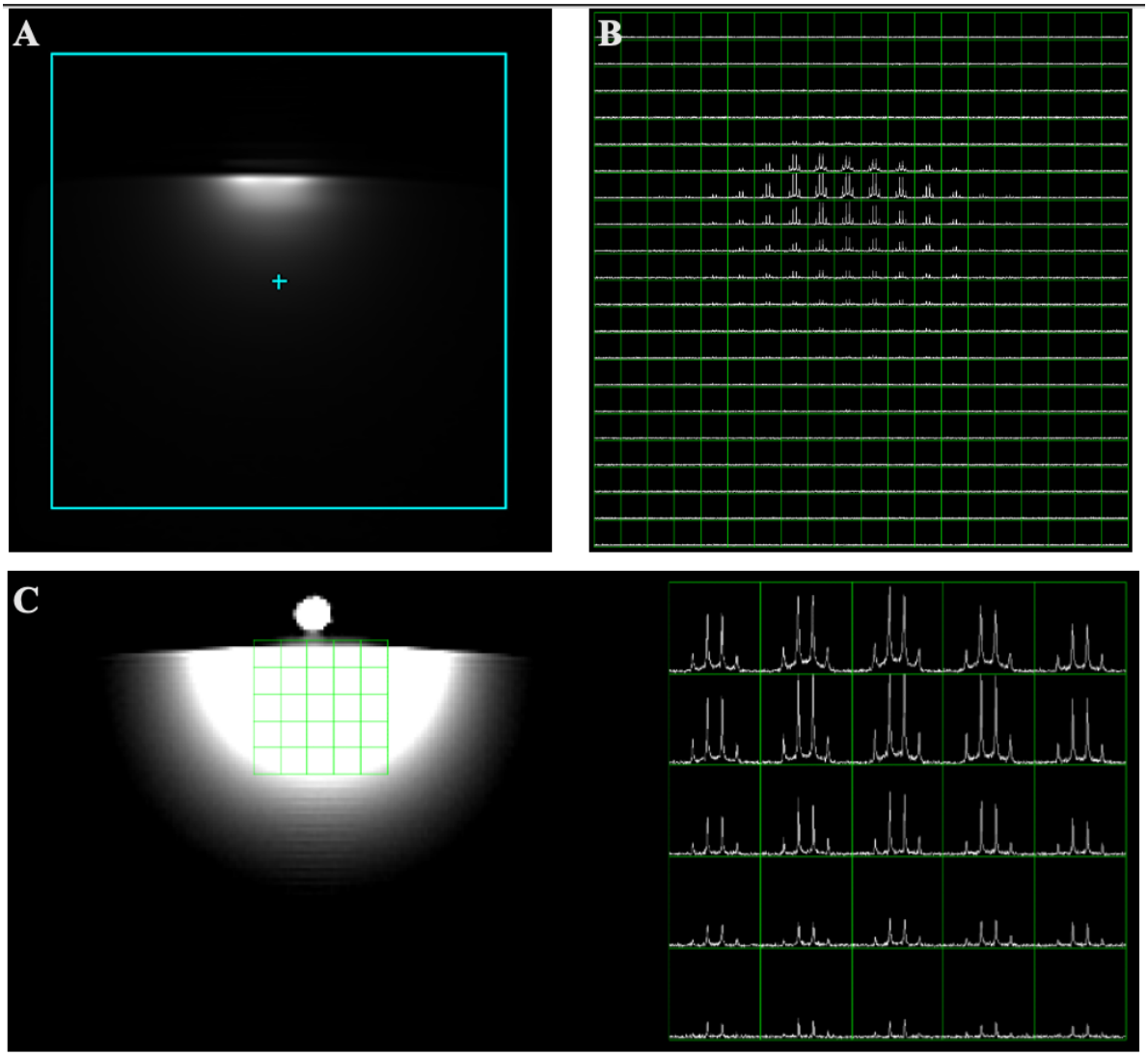

Figure 3.6: ^{1}H image and 2DCSI (1cm x1cm voxel size) overlay showing how the signals look over every pixel.

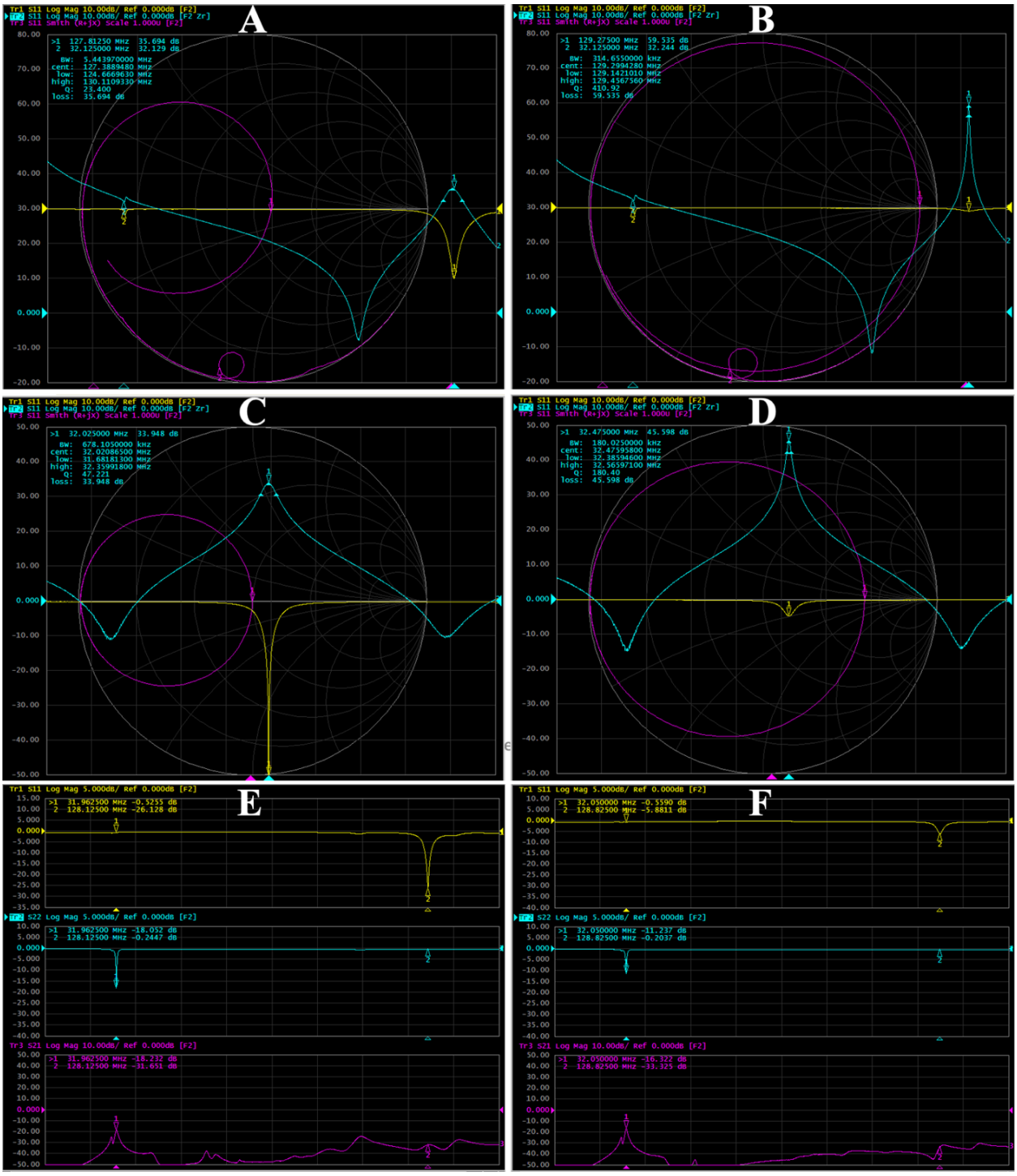

Figure 3.7: Displays LNA results of both elements when loaded and unloaded. A and B show loaded and unloaded Q of the 1H element respectively. C and D show loaded and unloaded Q of ^{13}C element. E and F show return loss and coupling of the ^{1}H and ^{13}C coils both when loaded and unloaded.

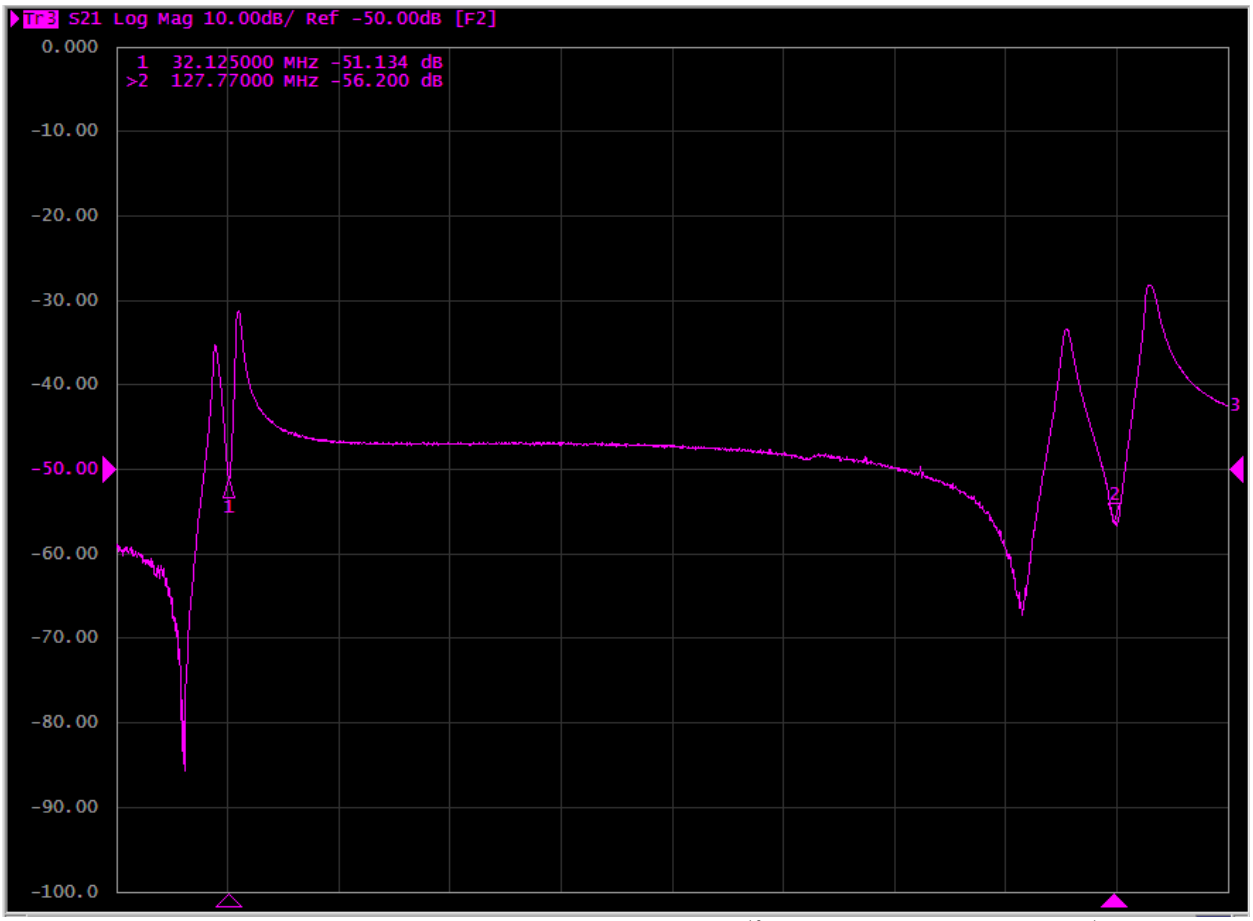

Figure 3.8: S21 trace of coils showing S21(-51.134dB) for ^{13}C and S21(-56.200dB) for ^{1}H showing the rf isolation for the new ERC.

3.6 References

1. Key Statistics About Prostate Cancer. https://www.cancer.org/cancer/prostate-cancer/about/key-statistics.html.
2. van den Bergh RCN, Loeb S, Roobol MJ. Impact of Early Diagnosis of Prostate Cancer on Survival Outcomes. *Eur Urol Focus*. 2015;1(2):137-146. doi:10.1016/j.euf.2015.01.002
3. Cuzick J, Thorat MA, Andriole G, et al. Prevention and early detection of prostate cancer. *Lancet Oncol*. 2014;15(11):e484-e492. doi:10.1016/S1470-2045(14)70211-6
4. Yacoub JH, Verma S, Moulton JS, Eggener S, Aytekin O. Imaging-guided prostate biopsy: conventional and emerging techniques. Radiographics. 2012 May-Jun;32(3):819-37. doi: 10.1148/rg.323115053. PMID: 22582361.
5. Norberg M, Busch C, Stavinoha J, Scardino PT, Magnusson A. Transrectal ultrasound-guided core biopsies of the prostate. A comparison between the standard 1.2-mm needle and three thinner needles. Acta Radiol. 1994 Sep;35(5):463-7. PMID: 8086255.
6. Norberg M. Transrectal ultrasound and core biopsies for the diagnosis of prostate cancer. A study of pretreatment investigation strategy for patients with suspected prostate cancer. Acta Radiol Suppl. 1994;393:1-21. PMID: 8184698.
7. Gordon JW, Chen HY, Autry A, et al. Translation of Carbon-13 EPI for hyperpolarized MR molecular imaging of prostate and brain cancer patients. *Magn Reson Med*. 2019;81(4):2702-2709. doi:10.1002/mrm.27549
8. Chen HY, Larson PEZ, Bok RA, et al. Assessing Prostate Cancer Aggressiveness with Hyperpolarized Dual-Agent 3D Dynamic Imaging of Metabolism and Perfusion. *Cancer Res*. 2017;77(12):3207-3216. doi:10.1158/0008-5472.CAN-16-2083

9. Larson PEZ, Chen HY, Gordon JW, et al. Investigation of analysis methods for hyperpolarized 13C-pyruvate metabolic MRI in prostate cancer patients. *NMR Biomed.* 2018;31(11):e3997. doi:10.1002/nbm.3997

10. Gawlitza J, Reiss-Zimmermann M, Thörmer G, et al. Impact of the use of an endorectal coil for 3T prostate MRI on image quality and cancer detection rate. *Sci Rep*. 2017;7:40640. Published 2017 Feb 1. doi:10.1038/srep40640

11. Ganie FA, Wani MS, Shaheen F, et al. Endorectal coil MRI and MR-spectroscopic imaging in patients with elevated serum prostate specific antigen with negative trus transrectal ultrasound guided biopsy. *Urol Ann*. 2013;5(3):172-178. doi:10.4103/0974-7796.115741

12. Dhatt R, Choy S, Co SJ, Ischia J, Kozlowski P, Harris AC, Jones EC, Black PC, Goldenberg SL, Chang SD. MRI of the Prostate With and Without Endorectal Coil at 3 T: Correlation With Whole-Mount Histopathologic Gleason Score. AJR Am J Roentgenol. 2020 Jul;215(1):133-141. doi: 10.2214/AJR.19.22094. Epub 2020 Mar 11. PMID: 32160050.

13. Nelson SJ, Kurhanewicz J, Vigneron DB, Larson PEZ, Harzstark AL, Ferrone M, van Criekinge M, Chang JW, Bok R, Park I, Reed G, Carvajal L, Small EJ, Munster P, Weinberg VK, Ardenkjaer-Larsen JH, Chen AP, Hurd RE, Odegardstuen L-I, Robb FJ, Tropp J, Murray JA. Metabolic Imaging of Patients with Prostate Cancer Using Hyperpolarized [1-^{13}C]Pyruvate. Science Translational Medicine. 2013; 5(198): 198ra108. PMCID: PMC420104

14. Chan W. P. (2013). Magnetic resonance imaging of soft-tissue tumors of the extremities: A practical approach. *World journal of radiology*, *5*(12), 455–459. https://doi.org/10.4329/wjr.v5.i12.455

15. Granlund, K. L., Tee, S. S., Vargas, H. A., Lyashchenko, S. K., Reznik, E., Fine, S., Laudone, V., Eastham, J. A., Touijer, K. A., Reuter, V. E., Gonen, M., Sosa, R. E., Nicholson, D., Guo, Y. W., Chen, A. P., Tropp, J., Robb, F., Hricak, H., & Keshari, K. R. (2020). Hyperpolarized MRI of

Human Prostate Cancer Reveals Increased Lactate with Tumor Grade Driven by Monocarboxylate Transporter 1. *Cell metabolism*, *31*(1), 105–114.e3. https://doi.org/10.1016/j.cmet.2019.08.024

16. Vaeggemose, M., F Schulte, R., & Laustsen, C. (2021). Comprehensive Literature Review of Hyperpolarized Carbon-13 MRI: The Road to Clinical Application. *Metabolites*, *11*(4), 219. https://doi.org/10.3390/metabo11040219
17. Aggarwal, R., Vigneron, D. B., & Kurhanewicz, J. (2017). Hyperpolarized 1-[^{13}C]-Pyruvate Magnetic Resonance Imaging Detects an Early Metabolic Response to Androgen Ablation Therapy in Prostate Cancer. *European urology*, *72*(6), 1028–1029. https://doi.org/10.1016/j.eururo.2017.07.022
18. Han, M., Partin, A. W., Piantadosi, S., Epstein, J. I., & Walsh, P. C. (2001). Era specific biochemical recurrence-free survival following radical prostatectomy for clinically localized prostate cancer. *The Journal of urology*, *166*(2), 416–419.
19. Turkbey B, Merino MJ, Gallardo EC, et al. (2014) Comparison of endorectal coil and nonendorectal coil T2 W and diffusion-weigh- ted MRI at 3 Tesla for localizing prostate cancer: correlation with whole-mount histopathology. J Magn Reson Imaging 39(6):1443– 1448. doi:10.1002/jmri.24317
20. Roemer PB, Edelstein WA, Hayes CE, et al. The NMR phased array. Magn Reson Med. 1990; 16:192–225. [PubMed: 2266841]
21. Gordon JW, Vigneron DB, Larson PE. Development of a symmetric echo planar imaging framework for clinical translation of rapid dynamic hyperpolarized 13C imaging. *Magn Reson Med.* 2017;77:826–832.

22. Geraghty BJ, Lau JY, Chen AP, Cunningham CH. Dual-echo EPI sequence for integrated distortion correction in 3D time-resolved hyperpolarized 13C MRI. *Magn Reson Med.* 2018;79:643–653.

23. Feinberg DA, Hale JD, Watts JC et al. Halving MR imaging time by conjugation: demonstration at 3.5 kG. Radiology 1986; 161:527-531

24. Kouchkovsky ID, Chen HY, Ohliger MA, Wang ZJ, Bok RA, Gordon JW, Larson PEZ, Frost M, Okamoto K, Cooperberg MR, Kurhanewicz J, Vigneron DB, Aggarwal R, Hyperpolarized 1-[^{13}C]-Pyruvate Magnetic Resonance Imaging Detects an Early Metabolic Response to Immune Checkpoint Inhibitor Therapy in Prostate Cancer, European Urology, Volume 81, Issue 2, 2022, Pages 219-221, ISSN 0302-2838, https://doi.org/10.1016/j.eururo.2021.10.015. (https://www.sciencedirect.com/science/article/pii/S0302283821021163)

25. Zhu Z, Zhu X, Ohliger MA, Tang S, Cao P, Carvajal L, Autry AW, Li Y, Kurhanewicz J, Chang S, Aggarwal R, Munster P, Xu D, Larson PEZ, Vigneron DB, Gordon JW, Coil combination methods for multi-channel hyperpolarized 13C imaging data from human studies, Journal of Magnetic Resonance, Volume 301, 2019, 73-79,ISSN1090-7807,https://doi.org/10.1016/j.jmr.2019.01.015. (https://www.sciencedirect.com/science/article/pii/S1090780719300217)

26. Chen HY, Bok RA, Cooperberg MR, Nguyen HG, Shinohara K, Westphalen AC, Wang ZJ, Ohliger MA, Gebrezgiabhier D, Carvajal L, Gordon JW, Larson PEZ, Aggarwal R, Kurhanewicz J, Vigneron DB. Improving multiparametric MR-transrectal ultrasound guided fusion prostate biopsies with hyperpolarized ^{13} C pyruvate metabolic imaging: A technical development study. Magn Reson Med. 2022 Dec;88(6):2609-2620. doi: 10.1002/mrm.29399. Epub 2022 Aug 17. PMID: 35975978; PMCID: PMC9794017.

27. Vaunghan, J. T & Griffiths, J. R, RF Coils for MRI (JohnWiley and Sons Ltd.,2012)

28. Z. Mo et al., "A Novel Three-Channel Endorectal Coil for Prostate Magnetic Resonance Imaging at 3T," in IEEE Transactions on Biomedical Engineering, doi: 10.1109/TBME.2023.3286488.

29. Roemer PB, Edelstein WA, Hayes CE, et al. The NMR phased array. Magn Reson Med. 1990; 16:192–225. [PubMed: 2266841]

30. Tropp J, Calderon P, Vigneron D, Carvajal L, Karoodinis K, Systems, methods and apparatus for an endo-rectal receive-only probe. Patent US7945308B2, 12-27-2005, 05-17-2011

31. Liu X, Tang S, Mu C, et al. Development of specialized magnetic resonance acquisition techniques for human hyperpolarized [^{13}C,$^{15}N_2$]urea + [1-^{13}C]pyruvate simultaneous perfusion and metabolic imaging. *Magn Reson Med.* 2022; 88(3): 1039-1054. doi:10.1002/mrm.29266

Chapter 4: Improving Multiparametric MR - TRUS Guided Fusion Prostate Biopsies with Hyperpolarized ^{13}C Pyruvate Metabolic Imaging : A Technical Development Study

4.1 Abstract

4.1.1 Purpose

To develop the techniques and establish a workflow using hyperpolarized ^{13}C (HP ^{13}C) MRI and the pyruvate-to-lactate conversion rate (k_{PL}) biomarker to guide MR-transrectal ultrasound (TRUS) fusion prostate biopsies.

4.1.2 Methods

The integrated multiparametric MRI (mpMRI) exam consisted of a 1-minute HP ^{13}C-pyruvate EPI acquisition added to a conventional prostate mpMRI exam. Maps of k_{PL} values were calculated, uploaded to PACS/targeting platform and displayed as color overlays on T_2-weighted anatomic images. Abdominal radiologists identified ^{13}C research biopsy targets based on the general rule of focal lesions with $k_{PL}>0.02(s^{-1})$, and created a targeting report for each study. Urologists conducted TRUS-guided MR fusion biopsies including the targets identified from the standard-of-care ^{1}H mpMRI, as well as 12-14 core systematic biopsies informed by the research ^{13}C-k_{PL} targets. All biopsy results were included in the final pathology report and calculated toward clinical risk.

4.1.3 Results

This study demonstrated the safety and feasibility of integrating HP ^{13}C metabolic targeting into routine ^{1}H-mpMRI and TRUS fusion biopsy workflows. Median turnaround time was less than

3 days between the scan and report/targeting, and two weeks scan-to-biopsy. Proposed technique was evaluated via five men (median age 71, PSA 8.4, CAPRA score 2) on active surveillance undergoing integrated scan and subsequent biopsies. No adverse event was reported. The number of ^{13}C targets was 1 (range:1-3) per patient, measuring 1.0 cm (range:0.6-1.9) in diameter, with a median k_{PL} of 0.0266 s^{-1} (range:0.0136-0.0410).

4.1.4 Conclusions

This proof-of-concept work demonstrated the safety and feasibility of integrating HP ^{13}C MR biomarkers to the SOC mpMRI workflow to guide MR-TRUS fusion biopsies.

4.2 Introduction

Multiparametric prostate MRI (mpMRI) is a standard-of-care imaging tool in the clinical workup of men with either known or suspected prostate cancer. Many practice guidelines such as National Comprehensive Cancer Network, American Urological Association, and European Association of Urology[1] have incorporated mpMRI into the workflow of prostate cancer diagnosis, although the indications for which mpMRI should be ordered, and at what frequency, still vary from guideline to guideline. This stems from divergent views regarding mpMRI's overall role and importance in the prostate cancer risk assessment.

Active surveillance is a preferred management strategy for men with low-risk, and selected intermediate-risk, localized prostate cancer to minimize treatment-associated morbidity without compromising oncologic outcomes. This is evidenced by the 10-year cancer-specific survival rate of nearly 99% for men undergoing active surveillance.[2] Whereas conventional mpMRI is widely used to guide prostate biopsies, its role in the surveillance setting has long been a subject of controversy.[3,4] Although mpMRI-guided confirmatory biopsy led to decreased active surveillance

failures,[5] a few randomized and retrospective studies failed to confirm the clinical utility of mpMRI in active surveillance.[6-8] These contradicting results not only lead to discrepant endorsement among guidelines regarding the use of surveillance mpMRI but highlighted the unmet need to improve both the diagnostic accuracy and yield of mpMRI in this setting.

Hyperpolarized (HP) carbon-13 (^{13}C)-pyruvate MRI is a new rapid molecular imaging technique that can detect increased pyruvate-to-lactate conversion rates (k_{PL}) in clinically significant, aggressive prostate cancer as compared to more indolent tumors[9,10]. The emerging technology uses dynamic nuclear polarization to increase the SNR of ^{13}C-enriched compounds by more than 50,000-fold through means of temporarily rearranging the spins to increase their nuclear polarization[11,12]. This enables interrogation of previously inaccessible in vivo metabolic pathways with unprecedented signal quality and quantitative accuracy. Several studies have explored the technical aspects of HP ^{13}C MRI in men with localized and metastatic prostate cancer,[13-15] as well as correlating ^{13}C markers to histological and molecular signatures of this malignancy.[16,17]

MR-guided transrectal ultrasound (TRUS) fusion biopsy was designed to utilize MRI's superior tissue contrast compared to ultrasound to detect prostatic lesions and improve prostate cancer diagnosis and grading. The fusion technology combines targeting information from a prior diagnostic MR exam with real-time, intraprocedural ultrasound guidance for accurate prostate tissue sampling[18]. MR-guided TRUS fusion biopsies, together with systematic biopsies, are usually conducted in urologists' offices as a simple outpatient procedure without requiring an operating room or general anesthesia.

Thus far HP ^{13}C MRI of the localized prostate cancer has been studied primarily in the context of a high-risk cohort, looking at pathological correlation with the prostatectomy specimen[16,17]. Prior to this study, it had not been applied to prospectively guide confirmatory or surveillance biopsies. This

technical development project aimed to integrate the metabolically-defined research targets based on HP ^{13}C-pyruvate MRI into mpMRI workflow, and guide MR-transrectal ultrasound (TRUS) fusion biopsies to improve the identification of clinically significant disease.

4.3 Methods

4.3.1 Hyperpolarized ^{13}C MRI and SOC multiparametric MRI Protocols

The MRI exams were conducted on a clinical 3 Tesla MRI scanner (MR750, GE Healthcare, Chicago IL) equipped with multinuclear spectroscopy capability. The MR coils and imaging setup have been previously described.[19] Briefly, HP ^{13}C imaging was performed using a clamshell Helmholtz transmitter and an endorectal coil for receive. For proton imaging, the body coil was used as a transmitter, and signal reception was accomplished using a 4-channel torso array combined with the endorectal probe. The endorectal receiver was a specialized proton (^{1}H)/^{13}C dual-element design.[19]

The proton mpMRI exam consisted of T_1-weighted fast spin echo (FSE), T_2-weighted FSE (in-plane resolution = 0.35 mm, 3 mm slices, TR/TE = 6000/102 ms), 3D T_2-FSE, and small FOV (Field-of-view optimized and constrained undistorted single-shot, FOCUS) DWI (TR/TE = 4000/78, pixel bandwidth = 1305, b = 0 and 600 s/mm^2, and 3 mm slice thickness) sequences. Dynamic contrast-enhanced imaging using a 3D fast spoiled gradient-recalled echo (SPGR) sequence (TR/TE = 3.5/0.9 ms, flip angle = 5°, and 3 mm slice thickness) with gadobutrol (Bayer Pharmaceuticals, Leverkusen, Germany) was acquired as the final series of the exam after the conclusion of the ^{13}C-pyruvate acquisition and other proton imaging. The multiparametric portion of the exam was consistent with the standard mpMRI[20] indicated for prostate cancer care at the University of California, San Francisco (UCSF).

For the hyperpolarized ^{13}C pyruvate study, pharmacy kits containing a mixture of 1.432 g of GMP grade [1-^{13}C] pyruvic acid (MilliporeSigma, Miamisburg OH) and 28 mg electron paramagnetic agent (AH111501; GE Healthcare, Oslo, Norway) were prepared and polarized in a 5 Tesla clinical-research polarizer (SPINLab, GE Healthcare, Chicago IL) at 0.77 K for 2.5–3 hours. Subsequently, the pyruvic acid was rapidly dissoluted and neutralized with tris-EDTA buffer solution, yielding sterile doses meeting release criteria of pyruvate concentration (median: 248 mM, 238–271 mM), polarization (median: 38.4%, 34.6%–40.6%), pH (median: 7.7, 7.4–8.2), temperature (<37 °C), and electron paramagnetic agent concentration (median: 1.5 μM, 0.7–1.9 μM). Following terminal sterilization, pharmaceutical release was issued after confirming quality control parameters and filter bubble point test as previously published.[21] The dosage of pyruvate solution delivered to the patient was 0.43 mL/kg at an injection rate of 5 mL/s (up to 40 mL), immediately followed by a 20 mL saline flush at the same rate.

A symmetric EPI sequence was prescribed for the HP ^{13}C study.[22] Key sequence parameters included TR/TE = 1 s/25.2 ms; resolution = 6.5–8 mm in-plane, 8 mm through-plane; FOV = 10.4 × 10.4–12.8 × 12.8 cm in-plane, and 11.2 cm through-plane. Independent flip angles were applied to pyruvate (15°) and lactate (30°) resonances. The acquisition started 10 s after the completion of the pyruvate injection and saline flush. A rapid, low-resolution T_2-FSE axial series (in-plane resolution = 0.35 × 0.8 mm, 3 mm slices, ~1 min length) was acquired immediately after the ^{13}C scan to measure possible motion shift during the exam, which could result from patient movements or bladder filling, and the resulting misalignment in between series. ^{13}C center frequency and power were calibrated using a built-in 8 M urea phantom inside the endorectal coil. Transmit power was increased to ~133% of the nominally calibrated power to compensate for the inductive coupling losses between clamshell transmitter and the ^{13}C element of the endorectal coil.

4.3.2 Image Processing

The ^{13}C-pyruvate EPI images were reconstructed using the GE Orchestra Toolbox (GE Healthcare, Chicago IL). Nyquist ghost correction was conducted using the ^{1}H reference scan method, as previously described.[22] Global phases of the pyruvate and lactate images were independently calculated and accounted for. The HP ^{13}C metabolic biomarker, k_{PL}, was quantified using an inputless 2-site exchange model that makes no assumptions about the dynamic or bolus profile of pyruvate but rather derives k_{PL} values solely based on measured pyruvate and lactate signals for improved robustness.[23]

Any misalignment was manually calculated between the high-quality T_2-weighted series, acquired near the beginning of the exam, and the quick, post-^{13}C-injection T_2-FSE series, and the ^{13}C data were shifted accordingly in 3D to compensate for motion offset. This improved the alignment precision between the k_{PL} maps and the high-quality T_2 series on the targeting software Dynacad (Philips Invivo Corp., Gainsville, FL), and thereby allowed more accurate lesion identification and outlining.

4.3.3 Transfer of ^{13}C-Pyruvate MRI Data to PACS and Fusion Targeting Software

The k_{PL} maps were interpolated to the T_2-FSE resolution, matching the exact same registration and matrix size as the T_2 series for easy visualization and overlays. A predefined series number was assigned to the k_{PL} maps. For example, if the high-quality T_2 were series 5, the k_{PL} map would have been series 502.

The k_{PL} map series was labeled as *nondiagnostic HP-13C kPL (diffusion)* to easily distinguish it from clinical ^{1}H mpMRI sequences. The color k_{PL} map was overlaid on T_2-weighted images. Using the keyword "(Diffusion)" masqueraded the k_{PL} maps as a diffusion-weighted series. This nomenclature allowed us to repurpose the built-in color overlay function on Dynacad (Philips Invivo Corp.; referred

to as "fusion" overlays on the UI) that was intended for overlay of DWI as a pseudo color map over grayscale T_2-weighted images.

The k_{PL} maps were first uploaded to the picture archiving and communication system (PACS). Following a quality control check on one of the PACS workstations to ensure correct registration, the k_{PL} maps were transferred to the Dynacad (Philips Invivo Corp.), a commercial targeting software that radiologists routinely use to identify and outline suspicious prostate MRI lesions as a part of biopsy planning. All the processing and data transfer occurred between our internal radiology network and PACS system and were therefore compliant with the Health Insurance Portability and Accountability Act.

4.3.4 Prostate Lesion Targeting and Fusion Biopsy

Figure 4.1 illustrates the workflow of HP ^{13}C MR research targeting of the prostate. The conventional ^{1}H mpMRI exam was interpreted by board-certified radiologists according to the standard departmental workflow, and any lesions were categorized using Prostate Imaging Reporting and Data System (PIRADS) v2.1.[24] Any suspicious lesions were outlined in Dynacad (Philips Invivo Corp.) in preparation for targeted biopsy. One of 3 board-certified abdominal radiologists, each with more than 10 years of experience reading prostate MRI, additionally outlined the ^{13}C research targets on the k_{PL}-T_2w color overlay displayed on Dynacad (Philips Invivo Corp.) (Figure 2A). The ^{13}C research targets were identified and delineated following the general recommendation of delineating focal lesions on the k_{PL}map with k_{PL} value >0.02(s^{-1}), a biomarker of suspected cancer.[17] The recommended k_{PL}threshold of 0.02(s^{-1}) for this initial technical development study was selected based on a prior high-risk cohort of patients (Supporting Information Figure S1), who after ^{13}C-pyruvate MRI scans underwent radical prostatectomy with step-section histopathology (gold standard), representing the k_{PL} differences of high- versus low-grade tumors (corrected for different MR

sequence TEs[25]). Radiologists' experience and judgment play an important role in target selection (similar to selection of ^{1}H MRI targets). Their discretion to include/exclude a target is allowed based on lesion focality, shape, and visual features, as well as likelihood of tumor presence in a given anatomical zone. The ^{1}H mpMRI-defined clinical targets and ^{13}C-defined research targets were independently labeled for urologist review.

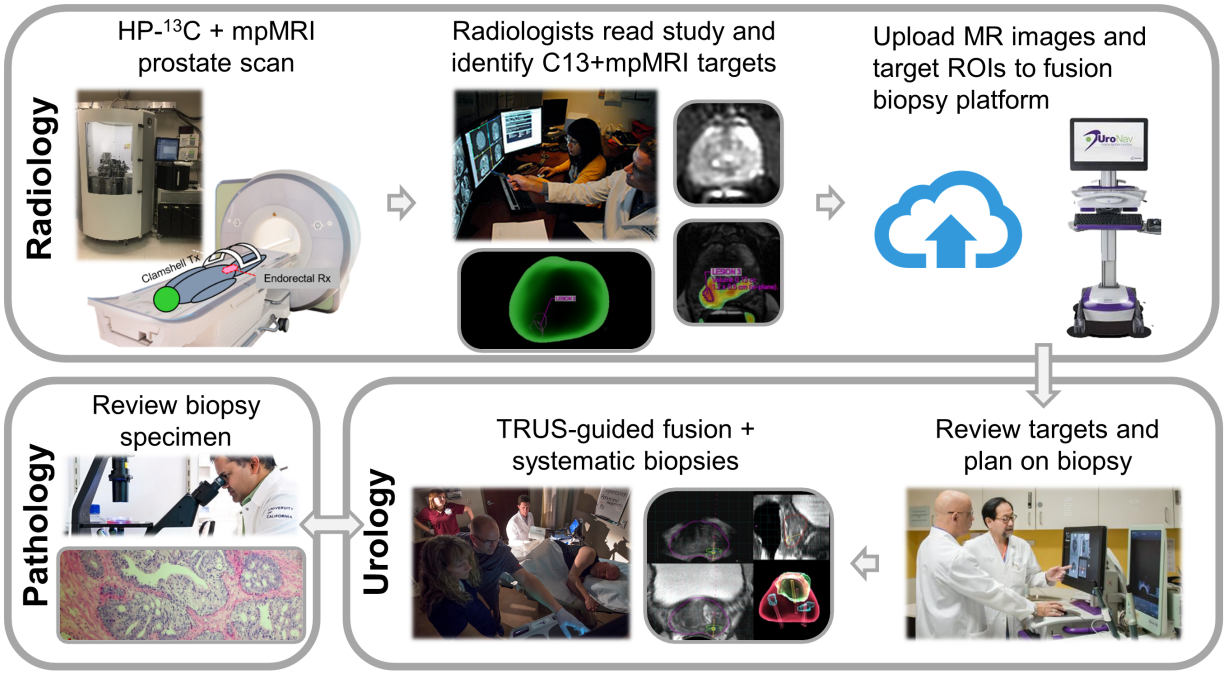

Figure 4.1: The workflow developed in this project for HP ^{13}C MR research targeting of prostate biopsies, based on abnormally high pyruvate-to-lactate conversion k_{PL} values. The HP ^{13}C MR exam and research targeting were integrated into the SOC MRI fusion and systematic biopsy procedures at our institution. First, the patient undergoes an integrated mpMRI exam of the prostate, including a 1-minute acquisition following the HP ^{13}C-pyruvate injection. The k_{PL} map is calculated and uploaded to PACS and a software targeting platform (DynaCAD, Phillips Invivo Corp., Gainsville FL). A radiologist reads the study and outlines the research targets based on ^{13}C k_{PL} findings, in addition to those from the PIRADS lesions based on the ^{1}H mpMRI. The targets and a report are uploaded to the fusion biopsy system (Uronav, Phillips Invivo Corp., Gainsville FL) in the urologist's offices, where they review the targeting and plan for the procedure. After US/MRI fusion guided biopsies are performed, the tissue specimens are submitted to Pathology for processing and diagnosis. Thus, the HP ^{13}C research biopsy integration takes advantage of the existing infrastructure and minimizes the additional workload for the researchers and clinicians involved.

(A)

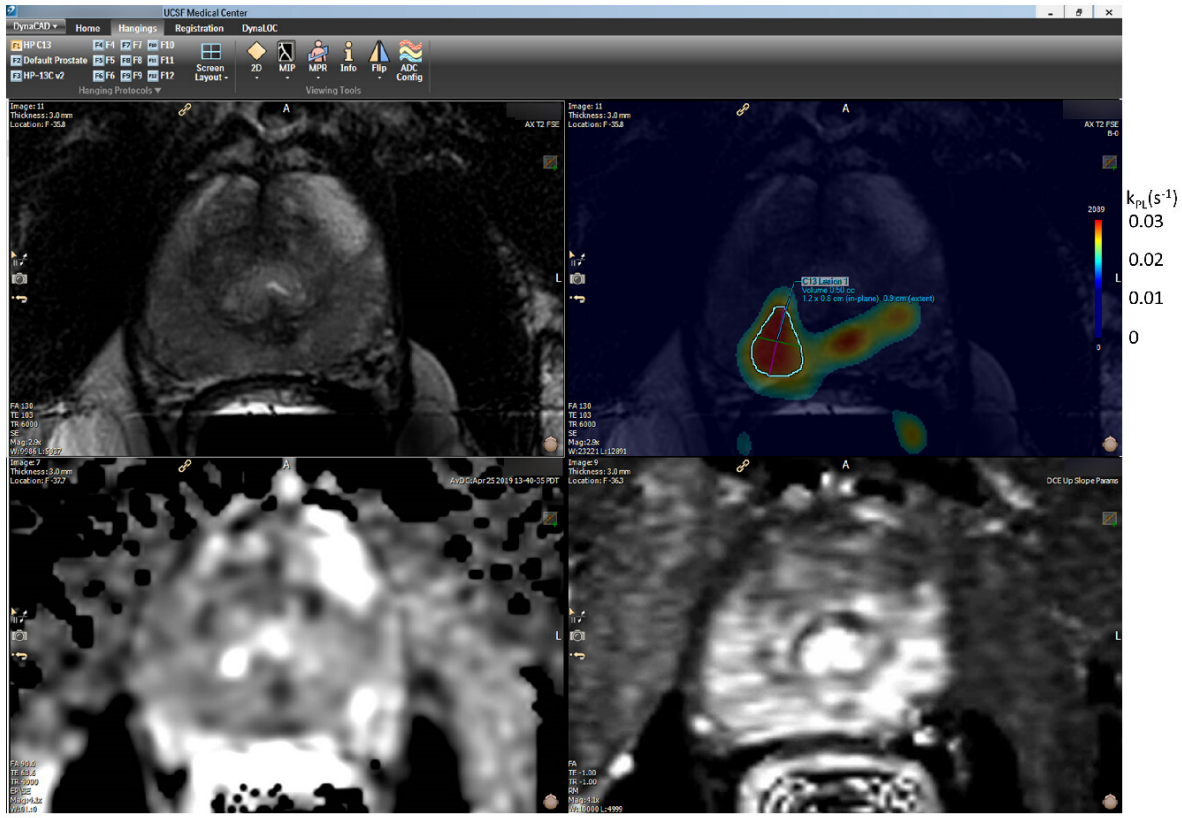

(B)

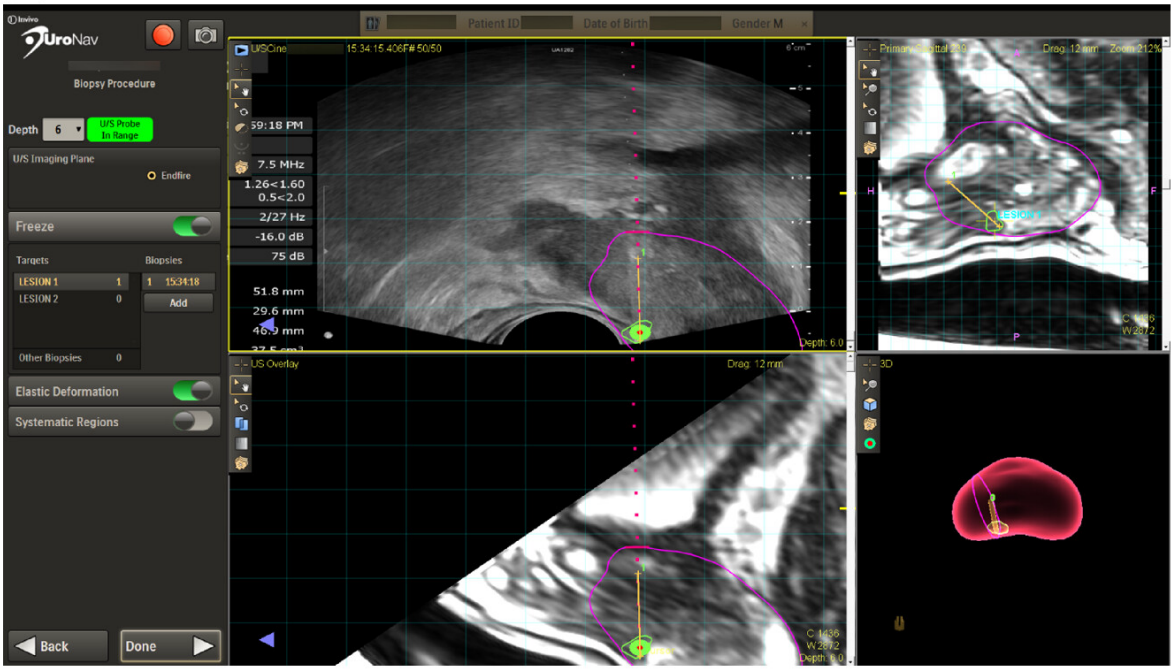

Figure 4.2: (A) A representative targeting protocol using a commercial prostate biopsy targeting platform (DynaCAD, Phillips Invivo Corp., Gainesville, FL). This protocol can also be found in Supplemental information Video S1. (Figure caption continued on the next page.)

(Figure caption continued from the previous page.) The 3D k_{PL} image series was named with the keyword "diffusion" to allow a fusion overlay, displaying k_{PL} as a pseudocolor over T_2-weighted series. The overlay was displayed side-by-side with T_2, ADC and DCE maps, enabling the radiologist to correlate between series and outline 3D ROI for both SOC PIRADS and ^{13}C research biopsy targets. Whereas the recommended k_{PL} threshold for identifying potentially high-grade ^{13}C lesions was set to $0.02(s^{-1})$, the lowest value of the heatmap was set to 0.01 for display purposes. This is designed to provide radiologists context on the shape/size of the lesion. The corresponding k_{PL} scales is shown next to the original color bar. **(**B**)** Both clinical and research targets are transferred to a commercial TRUS-fusion biopsy platform (Uronav, Philips Invivo Corps.), where the research biopsy targets were counted as systematic biopsies. The urologist sampled these targets under TRUS fusion guidance during a biopsy session, assisted by TRUS-MRI fusion (left panel: US axial, top right: MR sagittal) and 3D-rendered segmentation (bottom right panel) of the prostate. The biopsied tissues were submitted for histopathology analyses.

Both ^{13}C research and standard ^{1}H mpMRI targeted biopsies were conducted by 1 of the 3 board-certified urological oncologists, each with more than 10 years of experience, who used a commercial fusion-biopsy platform (Uronav, Philips Invivo Corp., Gainsville, FL) following the standard mpMRI-targeted biopsy procedure at our institution (Figure 2B). The transrectal biopsy approach was used by our urologists per institutional practice. The MRI-generated overlays delineating $^{13}C/^{1}H$ targets were fused with real-time TRUS images in the UroNav system (Philips Invivo Corp.) to guide the biopsy sampling. Systematic TRUS biopsies (12–14 cores) were also conducted in the same session, and the biopsy cores of any ^{13}C research target replaced the systematic biopsy in the same sextant. As such, the ^{13}C research biopsy did not increase the total number of cores.

A sample overlay and targeting procedure is illustrated in Supporting Information Video S1.

4.3.5 Patient Characteristics

Five patients with biopsy-confirmed prostate cancer were enrolled (NCT03933670). Eligible patients were 18 years or older, had a biopsy-confirmed diagnosis of prostate cancer, ECOG score 0 or 1, and were either candidates for or currently on an active surveillance protocol as defined by the UCSF urologic oncology practices at the time of enrollment.[26] The key exclusion criteria entailed prior

treatments for prostate cancer, biopsy within 14 days prior to ^{13}C MRI, poorly controlled hypertension, or contraindication for endorectal coil placement. The patient studies were conducted with informed consent in compliance with Food and Drug Administration- and Institutional Review Board-approved protocols (NCT03933670).

4.3.6 Pathology Assessment

The specimens from the ^{13}C research biopsies were submitted to pathology along with the other samples from the same session. All formalin-fixed–paraffin-embedded cores were read by experienced urologic pathologists in a standardized fashion[27] and included in the final pathology report. UCSF–Cancer of the Prostate Risk Assessment (CAPRA) score[28] was recalculated based on the updated biopsy findings and the most recent prostate-specific antigen values.

4.4 Results:

4.4.1 Safety and Technical Feasibility

Integrated MRI exams and the ensuing biopsies for all 5 patients were safe, successful, and without adverse events. The k_{PL} (HP ^{13}C metabolic biomarker) map was calculated and uploaded to PACS/Dynacad (Philips Invivo Corp.) along with the mpMRI exam. Image postprocessing and upload of k_{PL} maps were done the same day, typically within 1–2 h after the end of the exam. The average turnaround time for the MRI report and targeting was less than 3 days after each exam. A ^{13}C research biopsy targeting report (a representative instance given in Figure 4.3) was generated and showed the target locations in the 3D segmented prostate, as well as the ^{13}C-k_{PL}/T_2 overlay, diffusions, and T_1-weighted images arranged side by side to assist the urologists planning the biopsies.

Figure 4.3: Shows a representative biopsy targeting report a radiologist created using DynaCAD (Phillips Invivo Corp., Gainsville FL). The report and targets were then sent to the UroNav system (Phillips Invivo Corp., Gainsville FL) to assist the urological oncologist identify the ^{1}H mpMRI (PIRADs) and ^{13}C research targets and plan for the biopsy procedure. The report, shown as montage here, illustrates the target locations on the 3D segmented prostate for visual reference (left panel). In the center panel, the ^{13}C-k_{PL}/T_2 overlay, DWI, and T_1-weighted images arranged side by side. A ^{13}C-k_{PL} lesion was identified and outlined at the right mid PZ. The right panel reports the automatically calculated volumes and mean ADC values over the outlined ^{13}C target.

4.4.2 HP ^{13}C MRI Targeting and MR-Guided TRUS Fusion Biopsy

The patient demographics (N = 5) and clinical characteristics are summarized in Figure 4.4. The patients enrolled in this study had low- to intermediate-risk disease with median age 71 (range: 62–79), prostate-specific antigen 8.4 ng/mL (range: 1.3–17), and CAPRA score 2 (range: 1–3). The median number of ^{13}C research targets was 1 (range: 1–2), and that of proton mpMRI was 1 (range: 0–2). The ^{13}C targets measured 1 cm (range: 0.6–1.9) in diameter; the median k_{PL} was 0.0319 s^{-1} (range:

0.0198–0.0410); and the intralesion distribution is given in Table 4.1. The mean k_{PL} in the segmented prostate excluding ^{13}C targets was $0.0110 \pm 0.0022\ s^{-1}$. The index lesions on proton mpMRI had a median PIRADS score 4 (range: 2–5). The ^{1}H targets had a median 1.1 cm (range: 0.9–2) diameter. All 5 patients underwent TRUS/MRI fusion and systematic biopsies after the integrated mpMRI exam, with 2–3 cores sampled per target.

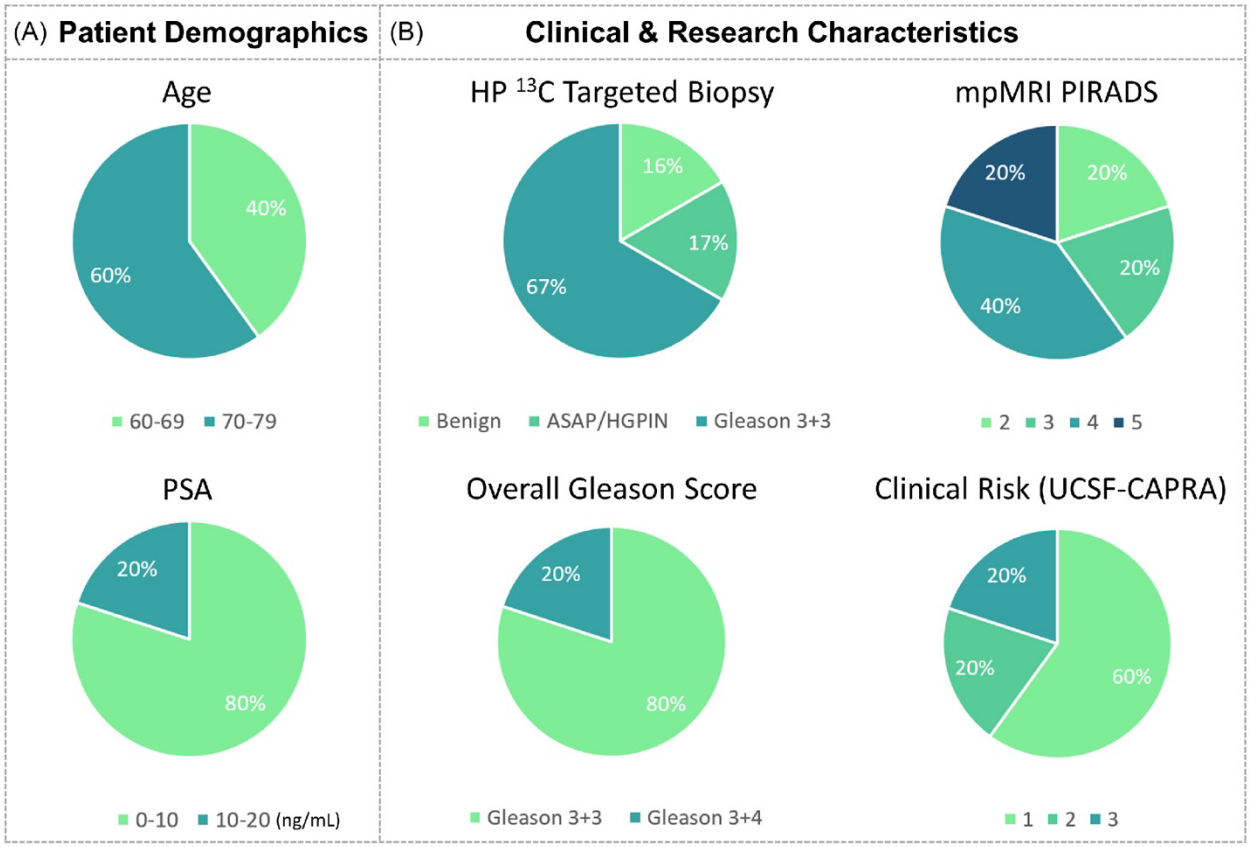

Figure 4.4: (A) Pie chart summarizing the serum PSA and age of this initial cohort. (B) Pie chart summarizing the pathologic characteristics of the HP ^{13}C research biopsies, PIRADS scores of ^{1}H mpMRI biopsies, overall Gleason score, and clinical risk (CAPRA score). The Gleason 3 + 4 findings in patient 3 in the left midgland (contralateral to the ^{13}C target) was small-volume (1 out of 4 cores in the sextant, <5% involvement per core) and only detected by systematic biopsy. The k_{PL} value per lesion was calculated from the maximum voxel.

Table 4.1: Summary of the clinical characteristics and biopsy findings from the five patients in this study. All the integrated 13C-1H mpMRI studies and the associated biopsies were safe and successful without adverse events. The mean number of 13C targets was 1 (range:1-3) per patient, measuring 1cm (range:0.6-1.9) in diameter, with a median kPL of 0.0266s-1 (range:0.0136-0.0410). Low-grade cancer involvement was found in the cores corresponding to the 13C targets in 3 out of 5 patients. These findings were consistent with clinically low- to intermediate-risk disease.

Patient No.	Patient 1	Patient 2	Patient 3
PSA	9.6	8.4	4.2
UCSF CAPRA score	1	1	3
Risk group	Low	Low	Intermediate
No. of ^{13}C targets	1	1	1
k_{PL} at ^{13}C target(s^{-1})	0.0378 (σ = 0.0050)	0.0198 (σ = 0.0018)	0.0325 (σ = NA)
No. of (+) cores/total cores in targeted + systematic biopsy	4/17	5/18	10/18
Overall grade	3+3	3+3	3+4
No. of (+) ^{13}C cores/total ^{13}C cores	1/2	1/2	0/3
^{13}C core grade	3+3	3+3	Benign

4.4.3 Correlation between k_{PL} and Histopathologic Findings from Biopsy

Overall, 1 patient (patient 3) had Gleason 3 + 4, and 4 patients (patient 1,2,4,5) had 3 + 3 disease (number of biopsy cores positive for cancer per patient, median: 4/17, range: 3/19–10/18), combining pathological findings from standard and ^{13}C research-targeted biopsies (Table 4.1) (Figure 4.5) (Supporting Information Table S1). On a per patient basis, the maximum involvement of any core was 16%–52% (median: 16%). The cores sampled from ^{13}C research targets were Gleason 3 + 3 in 4 patients (patient 1,2,4,5), with median 16% involvement (range: 1%–16%). One patient (patient 5) had atypical small acinar proliferation and high-grade prostatic intraepithelial neoplasia

among the ^{13}C cores in 1 target, and the ^{13}C target in another patient (patient 3) contained benign prostate tissue.

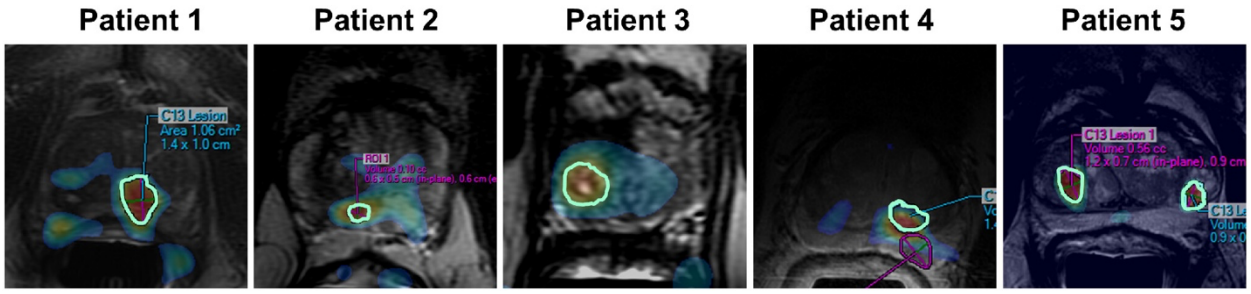

Figure 4.5: HP ^{13}C targets from the 5 cases summarized in Table 1 and Supporting Information Table 4.S1.

Figure 4.6 illustrates a representative case (patient 1) who underwent fusion plus systematic biopsies with a ^{13}C research target (k_{PL} = 0.0378 s^{-1}) at the left mid-apex peripheral zone and a ^{1}H mpMRI target (PIRADS 4) at the right mid-base transition zone. Pathological diagnosis of the tissue sample from the ^{13}C target was Gleason 3 + 3 cancer (16% involvement, ½ cores), whereas that from the ^{1}H-MRI target was described in the histology report as "rare atypical glands." Systematic biopsy found 3/12 cores with low volume 3 + 3 disease. Altogether, patient 1 had CAPRA score of 1, consistent with the clinically low-risk diagnosis.

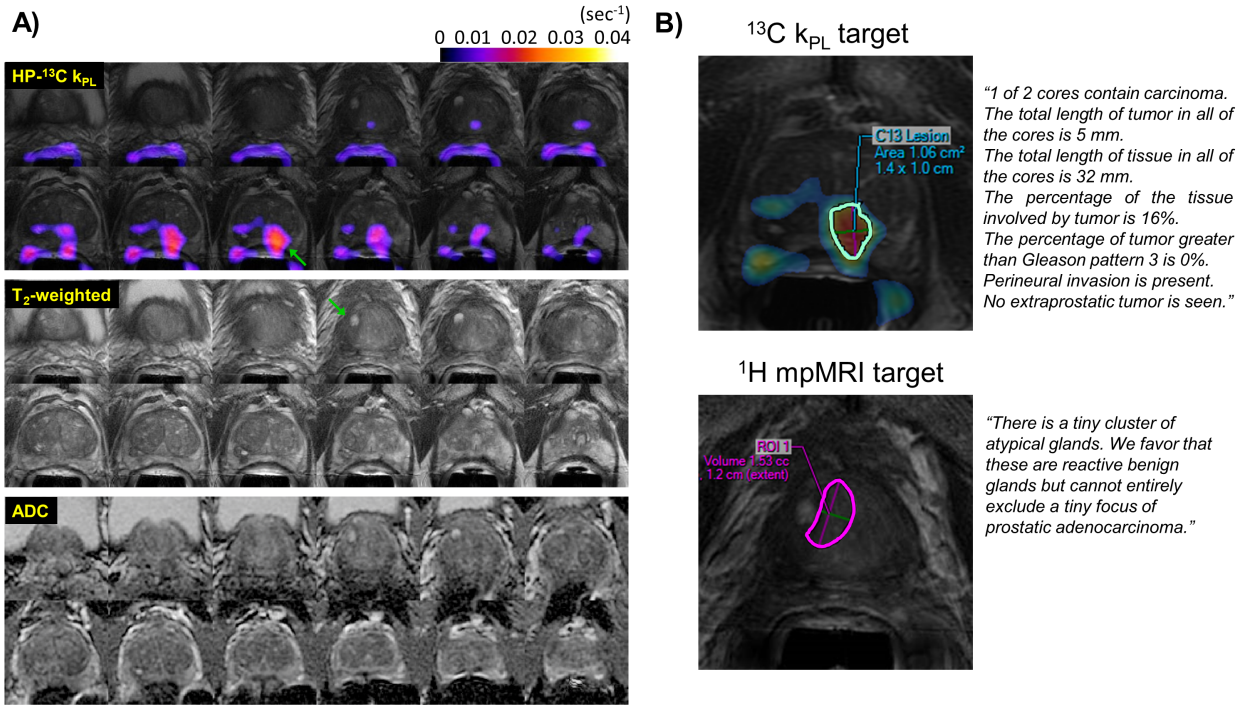

Figure 4.6: (A) Shows an example of an integrated HP-^{13}C research and standard ^{1}H mpMRI study (patient 1) including key multiparametric T_2-weighted, diffusion, and k_{PL} images identifying the biopsy target. One ^{1}H target (PIRADS 4) was identified at right mid-base transition zone and one ^{13}C research target (k_{PL} = 0.0378 s^{-1}) at left mid-apex peripheral zone, as indicated by the arrows. (B) ^{13}C and ^{1}H mpMRI biopsy targets as drawn by an experienced abdominal radiologist. Pathological diagnosis of the tissue sample from the ^{13}C target was Gleason 3 + 3 cancer (16% involvement, ½ cores), whereas that from the ^{1}H-MRI target was described in the histology report as "rare atypical glands".

Taken together with other clinical biomarkers, the biopsy findings in these 5 patients were consistent with clinically low- to intermediate-risk disease (summarized in Table 4.1), indicating that these patients are appropriate candidates for active surveillance. Four patients continued active surveillance after the study, whereas 1 patient later elected to undergo definitive treatment.

4.5 Discussion

We investigated for the first time the safety and technical feasibility of integrating a rapid, 1-min hyperpolarized ^{13}C-pyruvate MRI acquisition into standard-of-care ^{1}H mpMRI exams for guiding TRUS fusion prostate biopsies. No HP ^{13}C MRI- or biopsy-related adverse events were reported in

this initial cohort, which is in agreement with the excellent safety record of 600+ hyperpolarized ^{13}C MRI studies conducted worldwide thus far on patients and volunteers, as well as that of the active surveillance biopsy procedure at our institution and many other centers globally.[29,30] These results support future investigations focused on determining whether HP ^{13}C-^{1}H mpMRI could benefit men who are either candidates for or undergoing active surveillance of prostate cancer.

Using the existing infrastructure, we incorporated the rapid HP ^{13}C-pyruvate scan and the associated metabolic biomarker k_{PL} into the routine prostate MRI workflow, for which the major components includes image postprocessing, radiology read with lesion targeting, MR-guided TRUS fusion biopsies, and finally pathology evaluation. The integrable nature of this approach proved effective to improve efficiency and minimize additional effort.

The new ^{13}C targeting feature took advantage of the existing overlay and lesion outlining functions on a commercial, out-of-the-box prostate mpMRI processing, and targeting platform (Dynacad, Philips Invivo Corp.). This not only enabled easy deployment of the ^{13}C targeting capabilities on any PACS workstation within our radiology network, without the burden of additional software installations or modifications, but also allowed directly exporting the ^{13}C targets from the PACS/Dynacad (Philips Invivo Corp., Gainsville FL) to the fusion biopsy platform (UroNav, Philips Invivo Corp.) in the urological oncologists' offices, along with the ^{1}H mpMRI targets. We envision the same rationale and workflow are generalizable to other commercial targeting and fusion biopsy platforms[31,32] in a vendor-independent fashion. Our approach is presumably suitable for either transrectal or transperineal biopsy techniques because most commercial platforms support both by default.[33]

The ^{13}C research biopsy results were readily incorporated in the pathology report, and the pathological information of the ^{13}C biopsy cores, including the Gleason scores, total percentage of

tumor involvement, percentage of Gleason ≥4 pattern, and presence of adverse pathological features, were directly factored into the patients' clinical risk calculations, such as the UCSF-CAPRA score utilized at our institution. This paves the way for easy incorporation into routine clinical practice in the future.

Five patients were enrolled to test this new approach in a pilot, technical feasibility study. Interestingly, 4 out of 6 ^{13}C-k_{PL} targets did not correlate to a PIRADS lesion on ^{1}H mpMRI on a per-lesion basis. The discrepancy is consistent with the knowledge that HP ^{13}C MRI offers unique, complementary information based on prostate tumor metabolism in addition to the anatomical and functional features provided by ^{1}H mpMRI. It also highlights the need to investigate, in a larger cohort, whether a HP ^{13}C-^{1}H mpMRI protocol may overcome the known limitation in sensitivity with conventional prostate MRI for detection of occult but clinically significant tumors in the surveillance setting.[34]

Our study design substituted systematic biopsy cores with ^{13}C-targeted biopsy cores in the same sextant. The rationale was to reduce oversampling bias as a confounder when comparing the diagnostic accuracy between men who received fusion biopsies, including the ^{13}C targets, versus those who only received standard-of-care targeted and systematic biopsies. Our approach was consistent with that taken by the Active Surveillance Magnetic Resonance Imaging (ASIST) trial,[35] also designed to evaluate the utility of mpMRI-guided biopsy. An additional benefit was to fulfill the technique development aim for ^{13}C-guided fusion biopsy without introducing additional biopsy-related morbidity to the men who participated in this technical feasibility study.

Distinct from standard mpMRI series, the ^{13}C-k_{PL} series was labeled *nondiagnostic* on PACS. On Dynacad (Philips Invivo Corp.), the k_{PL} target lesions were labeled as *C13 lesion #*, setting them apart from the ^{1}H mpMRI targets, which were named *lesion 1*, *lesion 2*, etc. Using separate labels reduced

equivocal nomenclature and improved communications between imaging researchers and the patients' multidisciplinary care team by making the distinction between ^{13}C research imaging results and associated target lesions from those of ^{1}H mpMRI.

Whereas this study successfully demonstrated the safety and technical feasibility of guiding fusion prostate biopsies using the HP ^{13}C MRI-derived k_{PL} biomarker, a few limitations and challenges need to be acknowledged. First, a consensus in the field of prostate mpMRI is trending away from the use of endorectal coils. Similar to current conventional ^{1}H MRI coils, new flexible ^{13}C array coils are becoming commercially available to provide wider spatial coverage and higher SNR. Combining with the recent developments in ^{13}C parallel imaging[36] and denoising algorithms,[37,38] these advancements will likely obviate the need of endorectal coils for future ^{13}C-pyruvate prostate studies.

Second, the k_{PL} cutoff value ($0.02\ s^{-1}$), representing the dichotomy between high-grade prostate adenocarcinoma and low-grade tumor/benign tissue, was derived from the histopathology of a high-risk cohort who underwent radical prostatectomy.[17] This high-risk cohort likely possesses quite distinct underlying biology from the lower-risk, active surveillance population who may benefit the most from HP ^{13}C MRI. Whether the same k_{PL}cutoff value is appropriate for detecting occult high-grade disease in the surveillance population thus needs to be further explored and validated. Additionally, developing and testing a PIRADS-like grading schema for HP ^{13}C would benefit future clinical research but will require a broader evaluation in larger patient populations, as well as input from research radiologists on the methods developed in this project.

Although replacing the systematic cores with ^{13}C-k_{PL} cores reduces oversampling bias, a potential downside would be the missed opportunity to determine whether the standard 12–14 core systematic TRUS biopsy would have also found the 3 + 3 disease as the ^{13}C-guided biopsy in the same sextant on an individual-patient basis.

The primary factor affecting biopsy accuracy is the imperfect registration of MR-TRUS software fusion and mechanical deflection of the biopsy needles, which can similarly affect ^{1}H mpMRI targeted biopsies.[39] Therefore, biopsies are not considered a gold standard like postprostatectomy step-section histopathology is.

Finally, this technical feasibility study was neither designed nor powered to calculate the sensitivity/specificity of HP ^{13}C MRI-guided biopsy, and it would not be appropriate to report the clinical utility or biological significance results given the limited data and lack of a gold standard. The clinical question of whether ^{13}C MRI improves diagnostic accuracy of prostate cancer needs to be tested in a future larger-scale clinical trial. We believe such a trial is feasible given multiple NCI-designated cancer centers are now equipped with HP ^{13}C MRI capabilities and are either already performing or planning to conduct ^{13}C prostate cancer research.[40,41] Assuming HP ^{13}C MRI is proven to increase detection of clinically significant prostate cancer, whether this improvement ultimately translates into better disease-specific outcome will require long-term follow-up studies.

4.6 Conclusions

This technical development study demonstrated the feasibility of adding HP ^{13}C-pyruvate MRI to guide TRUS fusion prostate biopsies. HP ^{13}C MRI biomarkers were integrated into the diagnostic mpMRI workflow, complete with identification of ^{13}C research targets and sampling of these targets in fusion biopsies. These initial results support future studies in a larger cohort of patients to evaluate the role of HP ^{13}C MRI–guided targeted biopsy for improving prostate cancer risk stratification.

Supporting Information

Table 4.S1: Summary of Clinical Characteristics and biopsy findings from Patient 4 and 5.

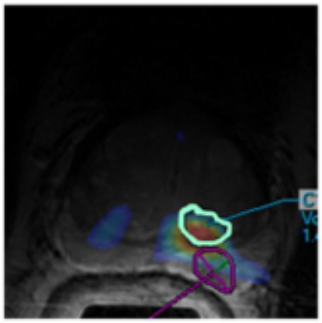

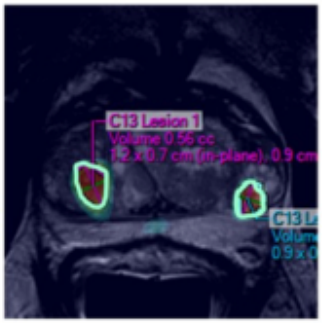

Patient #	Patient 4	Patient 5
PSA	1.3	17
UCSF CAPRA Score	2	1
Risk Group	Low	Low
# of ^{13}C Targets	1	2
k_{PL} at ^{13}C Target(s^{-1})	0.0410 (σ = 0.0012)	0.0279/0.0312 (σ = 0.0019)
# of (+) cores/total cores in targeted + systematic biopsy	8/23	3/19
Overall Grade	3+3	3+3
# of (+) ^{13}C cores/ total ^{13}C cores	2/2	2/3 (left), See below(right)
^{13}C Core Grade	3+3	3+3 (left), ASAP/HGPIN(right)

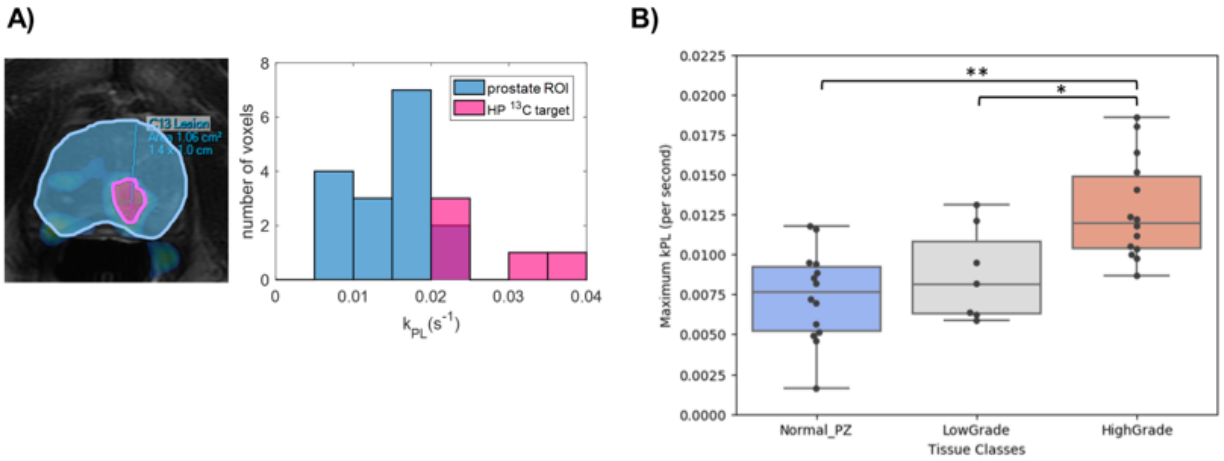

Figure 4.S1: A) an example case showing the comparison of k_{PL} in the ^{13}C targeted lesion versus segmented prostate outside of the lesion. Pathological diagnosis of the biopsy tissue was Gleason 3+3 tumor with 16% involvement. B) k_{PL} dichotomy between pathologist-defined low-grade prostate cancer (PCa) (Gleason ≤ 3+4), and high-grade prostate cancer (Gleason score ≥ 4+3). $^{*}p = 0.034$; $^{**}p = 0.0003$. The recommended k_{PL} threshold = $0.02(s^{-1})$ used in our study was corrected for the different MR sequence echo times between the EPSI acquisition in the cited reference verses the EPI in our study[24]. Figure reproduced with permission[17].

Supplemental Information Video 4.1. This video illustrates the protocol to create ^{13}C-k_{PL}/T_2fusion overlays. The new ^{13}C biopsy targeting feature takes advantage of the existing overlay and lesion outlining functions on a commercial, out-of-the-box prostate mpMRI processing and targeting platform (Dynacad). This not only enabled easy deployment of the ^{13}C biopsy targeting capabilities on any PACS workstation within our radiology network - without the burden of additional software installations or modifications, but also allows directly exporting the ^{13}C targets from the PACS/Dynacad to the fusion biopsy platform (UroNav).

4.7 References

1. Mottet N, van den Bergh RCN, Briers E, et al. EAU-EANM-ESTRO-ESUR-SIOG guidelines on prostate Cancer-2020 update. Part 1: screening, diagnosis, and local treatment with curative intent. *Eur Urol.* 2021; **79**: 243-262.
2. Hamdy FC, Donovan JL, Lane JA, Mason M, Metcalfe C, Holding P, et al. 10-Year Outcomes after Monitoring, Surgery, or Radiotherapy for Localized Prostate Cancer. N Engl J Med 2016;375(15):1415-24.
3. Ploussard G, Renard-Penna R. MRI-guided active surveillance in prostate cancer: not yet ready for practice. Nature Reviews Urology 2020:1-2.
4. Stavrinides V, Giganti F, Emberton M, Moore CM. MRI in active surveillance: a critical review. Prostate Cancer Prostatic Dis 2019;22(1):5-15.
5. Klotz L, Pond G, Loblaw A, Sugar L, Moussa M, Berman D, et al. Randomized Study of Systematic Biopsy Versus Magnetic Resonance Imaging and Targeted and Systematic Biopsy in Men on Active Surveillance (ASIST): 2-year Postbiopsy Follow-up. Eur Urol 2020;77(3):311-7.
6. Chesnut GT, Vertosick EA, Benfante N, Sjoberg DD, Fainberg J, Lee T, et al. Role of Changes in Magnetic Resonance Imaging or Clinical Stage in Evaluation of Disease Progression for Men with Prostate Cancer on Active Surveillance. Eur Urol 2020;77(4):501-7.
7. Chu CE, Lonergan PE, Washington SL, Cowan JE, Shinohara K, Westphalen AC, et al. Multiparametric magnetic resonance imaging alone is insufficient to detect grade reclassification in active surveillance for prostate cancer. European Urology 2020;78(4):515-7.
8. Ma TM, Tosoian JJ, Schaeffer EM, Landis P, Wolf S, Macura KJ, et al. The Role of Multiparametric Magnetic Resonance Imaging/Ultrasound Fusion Biopsy in Active Surveillance. Eur Urol 2017;71(2):174-80.

9. Albers MJ, Bok R, Chen AP, Cunningham CH, Zierhut ML, Zhang VY, et al. Hyperpolarized 13C lactate, pyruvate, and alanine: noninvasive biomarkers for prostate cancer detection and grading. Cancer Res 2008;68(20):8607-15.
10. Sriram R, Van Criekinge M, DeLos Santos J, Ahamed F, Qin H, Nolley R, et al. Elevated Tumor Lactate and Efflux in High-grade Prostate Cancer demonstrated by Hyperpolarized (13)C Magnetic Resonance Spectroscopy of Prostate Tissue Slice Cultures. Cancers (Basel) 2020;12(3).
11. Ardenkjaer-Larsen JH, Fridlund B, Gram A, Hansson G, Hansson L, Lerche MH, et al. Increase in signal-to-noise ratio of > 10,000 times in liquid-state NMR. Proc Natl Acad Sci U S A 2003;100(18):10158-63.
12. Golman K, in 't Zandt R, Thaning M. Real-time metabolic imaging. Proc Natl Acad Sci U S A 2006;103(30):11270-5.
13. Chen HY, Larson PEZ, Gordon JW, Bok RA, Ferrone M, van Criekinge M, et al. Technique development of 3D dynamic CS-EPSI for hyperpolarized (13) C pyruvate MR molecular imaging of human prostate cancer. Magn Reson Med 2018;80(5):2062-72.
14. Gordon JW, Chen HY, Autry A, Park I, Van Criekinge M, Mammoli D, et al. Translation of Carbon-13 EPI for hyperpolarized MR molecular imaging of prostate and brain cancer patients. Magnetic resonance in medicine 2018.
15. Chen HY, Aggarwal R, Bok RA, Ohliger MA, Zhu Z, Lee P, et al. Hyperpolarized (13)C-pyruvate MRI detects real-time metabolic flux in prostate cancer metastases to bone and liver: a clinical feasibility study. Prostate Cancer Prostatic Dis 2020;23(2):269-76.
16. Granlund KL, Tee SS, Vargas HA, Lyashchenko SK, Reznik E, Fine S, et al. Hyperpolarized MRI of Human Prostate Cancer Reveals Increased Lactate with Tumor Grade Driven by Monocarboxylate Transporter 1. Cell Metab 2020;31(1):105-14 e3.

17. Korn N, Larson PEZ, Chen H-Y, Gordon JW, Bok RA, Van Criekinge M, et al. The Rate of Hyperpolarized [1-13C] Pyruvate to [1-13C] Lactate Conversion Distinguishes High-Grade Prostate Cancer from Low-Grade Prostate Cancer and Normal Peripheral Zone Tissue in Patients. Proceedings of the 26th Annual Meeting of ISMRM 2018.
18. Logan JK, Rais-Bahrami S, Turkbey B, et al. Current status of MRI and ultrasound fusion software platforms for guidance of prostate biopsies. *BJU Int.* 2014; **114**: 641-652.
19. Nelson SJ, Kurhanewicz J, Vigneron DB, Larson PEZ, Harzstark AL, Ferrone M, et al. Metabolic Imaging of Patients with Prostate Cancer Using Hyperpolarized [1-C-13]Pyruvate. Science Translational Medicine 2013;5(198).
20. Tran GN, Leapman MS, Nguyen HG, Cowan JE, Shinohara K, Westphalen AC, et al. Magnetic Resonance Imaging-Ultrasound Fusion Biopsy During Prostate Cancer Active Surveillance. Eur Urol 2017;72(2):275-81.
21. Autry AW, Gordon JW, Chen HY, LaFontaine M, Bok R, Van Criekinge M, et al. Characterization of serial hyperpolarized (13)C metabolic imaging in patients with glioma. Neuroimage Clin 2020;27:102323.
22. Gordon JW, Vigneron DB, Larson PE. Development of a symmetric echo planar imaging framework for clinical translation of rapid dynamic hyperpolarized (13) C imaging. Magn Reson Med 2017;77(2):826-32.
23. Larson PEZ, Chen HY, Gordon JW, Korn N, Maidens J, Arcak M, et al. Investigation of analysis methods for hyperpolarized 13C-pyruvate metabolic MRI in prostate cancer patients. NMR Biomed 2018:e3997.
24. Turkbey B, Rosenkrantz AB, Haider MA, Padhani AR, Villeirs G, Macura KJ, et al. Prostate Imaging Reporting and Data System Version 2.1: 2019 Update of Prostate Imaging Reporting and Data System Version 2. Eur Urol 2019;76(3):340-51.

25. Chen HY, Gordon JW, Bok RA, et al. Pulse sequence considerations for quantification of pyruvate-to-lactate conversion kPL in hyperpolarized 13C imaging. *NMR Biomed.* 2019; **32**:e4052.
26. Welty CJ, Cowan JE, Nguyen H, Shinohara K, Perez N, Greene KL, et al. Extended followup and risk factors for disease reclassification in a large active surveillance cohort for localized prostate cancer. J Urol 2015;193(3):807-11.
27. Klein EA, Cooperberg MR, Magi-Galluzzi C, Simko JP, Falzarano SM, Maddala T, et al. A 17-gene assay to predict prostate cancer aggressiveness in the context of Gleason grade heterogeneity, tumor multifocality, and biopsy undersampling. Eur Urol 2014;66(3):550-60.
28. Cooperberg MR, Pasta DJ, Elkin EP, Litwin MS, Latini DM, Du Chane J, et al. The University of California, San Francisco Cancer of the Prostate Risk Assessment score: a straightforward and reliable preoperative predictor of disease recurrence after radical prostatectomy. J Urol 2005;173(6):1938-42.
29. Cooperberg MR, Zheng Y, Faino AV, Newcomb LF, Zhu K, Cowan JE, et al. Tailoring Intensity of Active Surveillance for Low-Risk Prostate Cancer Based on Individualized Prediction of Risk Stability. JAMA Oncol 2020;6(10):e203187.
30. Loeb S, van den Heuvel S, Zhu X, Bangma CH, Schroder FH, Roobol MJ. Infectious complications and hospital admissions after prostate biopsy in a European randomized trial. Eur Urol 2012;61(6):1110-4.
31. Baco E, Rud E, Eri LM, Moen G, Vlatkovic L, Svindland A, et al. A Randomized Controlled Trial To Assess and Compare the Outcomes of Two-core Prostate Biopsy Guided by Fused Magnetic Resonance and Transrectal Ultrasound Images and Traditional 12-core Systematic Biopsy. Eur Urol 2016;69(1):149-56.

32. Filson CP, Natarajan S, Margolis DJ, Huang J, Lieu P, Dorey FJ, et al. Prostate cancer detection with magnetic resonance-ultrasound fusion biopsy: The role of systematic and targeted biopsies. Cancer 2016;122(6):884-92.

33. Xiang J, Yan H, Li J, Wang X, Chen H, Zheng X. Transperineal versus transrectal prostate biopsy in the diagnosis of prostate cancer: a systematic review and meta-analysis. *World J Surg Oncol*. 2019; **17**: 31.

34. Johnson DC, Raman SS, Mirak SA, Kwan L, Bajgiran AM, Hsu W, et al. Detection of individual prostate cancer foci via multiparametric magnetic resonance imaging. European urology 2019;75(5):712-20.

35. Klotz L, Loblaw A, Sugar L, Moussa M, Berman DM, Van der Kwast T, et al. Active Surveillance Magnetic Resonance Imaging Study (ASIST): Results of a Randomized Multicenter Prospective Trial. Eur Urol 2019;75(2):300-9.

36. Feng Y, Gordon JW, Shin PJ, von Morze C, Lustig M, Larson PEZ, et al. Development and testing of hyperpolarized (13)C MR calibrationless parallel imaging. J Magn Reson 2016;262:1-7.

37. Brender JR, Kishimoto S, Merkle H, Reed G, Hurd RE, Chen AP, et al. Dynamic Imaging of Glucose and Lactate Metabolism by 13 C-MRS without Hyperpolarization. Scientific reports 2019;9(1):1-14.

38. Chen HY, Autry AW, Brender JR, Kishimoto S, Krishna MC, Vareth M, et al. Tensor image enhancement and optimal multichannel receiver combination analyses for human hyperpolarized (13) C MRSI. Magn Reson Med 2020;84(6):3351-65.

39. Cool DW, Zhang X, Romagnoli C, Izawa JI, Romano WM, Fenster A. Evaluation of MRI-TRUS fusion versus cognitive registration accuracy for MRI-targeted, TRUS-guided prostate biopsy. *AJR Am J Roentgenol*. 2015; **204**: 83-91.

40. Kurhanewicz J, Vigneron DB, Ardenkjaer-Larsen JH, Bankson JA, Brindle K, Cunningham CH, et al. Hyperpolarized (13)C MRI: Path to Clinical Translation in Oncology. Neoplasia 2019;21(1):1-16.
41. Brindle KM, Keshari KR. Editorial commentary for the special issue: technological developments in hyperpolarized (13)C imaging-toward a deeper understanding of tumor metabolism in vivo. MAGMA 2021;34(1):1-3.

Chapter 5: Development of Specialized Magnetic Resonance Acquisition Techniques for Human HP [^{13}C,$^{15}N_2$]Urea + [1-^{13}C]Pyruvate Simultaneous Perfusion and Metabolic Imaging

5.1 Abstract

5.1.1 Purpose

This study aimed to develop and demonstrate the in vivo feasibility of a 3D stack-of-spiral balanced steady-state free precession(3D-bSSFP) urea sequence, interleaved with a metabolite-specific gradient echo (GRE) sequence for pyruvate and metabolic products, for improving the SNR and spatial resolution of the first hyperpolarized ^{13}C-MRI human study with injection of co-hyperpolarized [1-^{13}C]pyruvate and [^{13}C,$^{15}N_2$]urea.

5.1.2 Methods

A metabolite-specific bSSFP urea imaging sequence was designed using a urea-specific excitation pulse, optimized TR, and 3D stack-of-spiral readouts. Simulations and phantom studies were performed to validate the spectral response of the sequence. The image quality of urea data acquired by the 3D-bSSFP sequence and the 2D-GRE sequence was evaluated with 2 identical injections of co-hyperpolarized [1-^{13}C]pyruvate and [^{13}C,$^{15}N_2$]urea formula in a rat. Subsequently, the feasibility of the acquisition strategy was validated in a prostate cancer patient.

5.1.3 Results

Simulations and phantom studies demonstrated that 3D-bSSFP sequence achieved urea-only excitation, while minimally perturbing other metabolites (<1%). An animal study demonstrated that compared to GRE, bSSFP sequence provided an ~2.5-fold improvement in SNR without perturbing

urea or pyruvate kinetics, and bSSFP approach with a shorter spiral readout reduced blurring artifacts caused by J-coupling of [^{13}C,$^{15}N_2$]urea. The human study demonstrated the in vivo feasibility and data quality of the acquisition strategy.

5.1.4 Conclusion

The 3D-bSSFP urea sequence with a stack-of-spiral acquisition demonstrated significantly increased SNR and image quality for [^{13}C,$^{15}N_2$]urea in co-hyperpolarized [1-^{13}C]pyruvate and [^{13}C,$^{15}N_2$]urea imaging studies. This work lays the foundation for future human studies to achieve high-quality and high-SNR metabolism and perfusion images.

5.2 Introduction

Hyperpolarized MRI has become essential for the characterization, treatment selection, and monitoring treatment response of tumors.[1-3] Although performing these assessments based on anatomy and structure is valuable, other functional imaging targets such as metabolism and perfusion provide information at the cellular and tissue level to improve such assessments.[4-7] Combining metabolism and perfusion is particularly attractive because alterations in both processes are hallmarks of cancer.[4-7] Concurrence or mismatch in the changes in metabolism and perfusion has been shown to be particularly valuable for cancer assessment.[8-12]

Hyperpolarized ^{13}C-MRI offers the unique capability to simultaneously image perfusion and metabolism using co-hyperpolarized [1-^{13}C]pyruvate and [^{13}C,$^{15}N_2$]urea, where each compound and downstream metabolic products can be separately imaged according to their chemical shifts.[4,13-15] This is a distinct advantage over positron emission tomography (PET), where metabolic and perfusion probes cannot be distinguished from each other and therefore, would require separate injections.

Our recent work has developed the co-polarization procedure of [1-^{13}C]pyruvate and [^{13}C,$^{15}N_2$]urea on a clinical SPINlab dynamic nuclear polarization polarizer, investigated its safety profile, and demonstrated the imaging feasibility of this imaging probe in pre-clinical studies using a 3T clinical MRI scanner.[15] Regulatory approvals from the US Food and Drug Administration (FDA) for the investigational use of co-hyperpolarized [1-^{13}C]pyruvate and [^{13}C,$^{15}N_2$]urea in human studies was subsequently obtained.

In this work, we developed and demonstrated the in vivo feasibility of a specialized acquisition strategy for co-hyperpolarized [1-^{13}C]pyruvate and [^{13}C,$^{15}N_2$]urea to provide high SNR and improved spatial resolution. The design was based on an SNR-efficient 3D balanced steady-state free precession (bSSFP) sequence[13,16-18] for urea combined with rapid metabolite specific imaging for pyruvate.[19,20] This approach builds off our recent work using the metabolite-specific bSSFP for ^{13}C-lactate[21] that provided an over 2-fold SNR improvement and was translated into human studies. The co-hyperpolarized [1-^{13}C]pyruvate and [^{13}C,$^{15}N_2$]urea strategy was tested in simulation, validated, and characterized in phantoms and animal models before being applied in first-in-human study demonstrating feasibility in prostate.

5.3 Methods

5.3.1 Sequence Design and Simulations

The strategy developed for co-hyperpolarized [1-^{13}C]pyruvate and [^{13}C,$^{15}N_2$]urea uses a metabolite-specific gradient echo (GRE)[19, 20] for pyruvate and its metabolic products (lactate in this

work) interleaved with a metabolite-specific bSSFP sequence for urea that we hypothesized will provide SNR benefits because of refocusing and the long T_2 relaxation times of [^{13}C, $^{15}N_2$]urea.[13]

The metabolite-specific 3D bSSFP urea sequence (Figure 5.1) designed in this study consists of spectrally selective multiband radiofrequency (RF) pulses, corresponding catalyzation RF pulses with amplitude increment/decrement, center-out uniform density stack-of-spiral readouts, and a spoiler gradient. The RF pulse applied to excite [^{13}C,$^{15}N_2$]urea resonance was designed based on a published multiband RF pulse design approach[21, 22] for minimizing the pulse duration. The parameters of this RF pulse include 6 ms pulse duration, 0.252G maximum B_1, 60 Hz passband on urea frequency, which can cover ±20 Hz J_{CN} splitting frequencies, 40 Hz-stopband with 0.4% ripples on pyruvate (240 Hz) frequency, and 40 Hz-stopband with 0.45% ripples on alanine (425 Hz), pyruvate hydrate (507 Hz), and lactate (635 Hz) frequencies (Figure 5.2A,B). To decrease the excitation intensity on the bicarbonate frequency from to initial designs,[15] the center frequency of passband was higher to move the bicarbonate frequency out of passband of urea (Supporting Information Figure 5.S2A and C). Correspondingly, the signal response of bSSFP is decreased by 50% in the new designed RF pulse (Supporting Information Figure 5.S2B and D). In the bSSFP sequence, the excitation train was set as a series of alternating flip angle pulses to oscillate magnetization around z-axis. To suppress signal oscillation and obtain a stable frequency response from the first readout, a set of catalyzation pulses were applied before acquisition. They were composed of 6 identical pulses with a nonlinear amplitude increment (i.e., 2.5°, 6°, 19°, 34.5°, 46.5°, and 50°). The acquisition used the 3D stack-of-spiral readout with 4 interleaves and 16 stacks for kz encoding. All gradients were balanced within each TR. After the acquisition, the magnetization was returned to z-axis by a set of reversed order catalyzation pulses.

Considering the catalyzation pulses can be affected by B_1 field inhomogeneity, one spoiler gradient was applied in *z*-axis to crush residual magnetization in *xy*-plane at the end of the sequence.

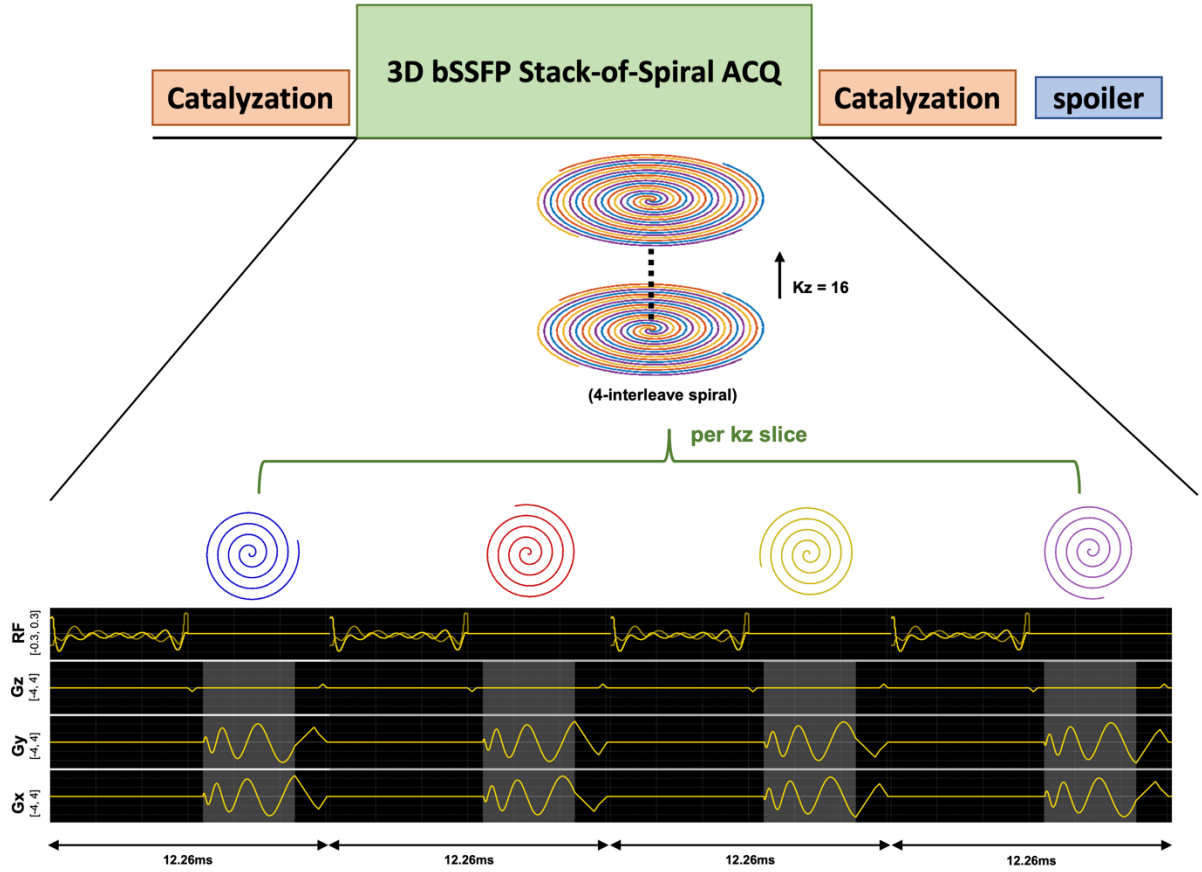

Figure 5.1: The proposed 3D urea bSSFP sequence consists of catalyzation, 3D-bSSFP stack-of-spiral acquisition (urea-selective RF excitation pulse and stack-of-spiral readout), and spoiler gradients. The stack-of-spiral readout has 16 slices per stack, and each slice has 4 interleaves. The highlighted gray region denotes the spiral readout duration (4 ms).

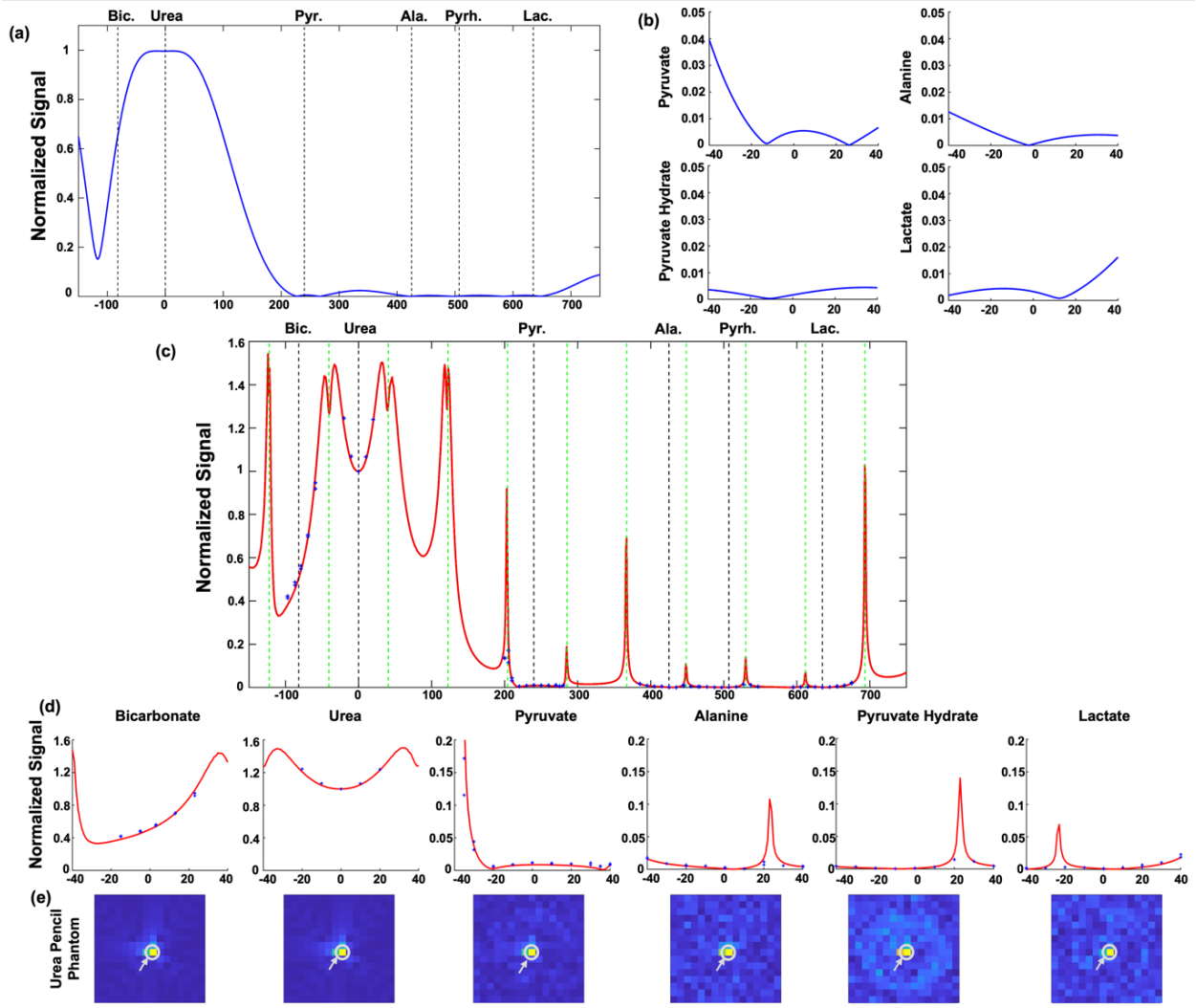

Figure 5.2: The corresponding excitation profiles of metabolite-specific bSSFP urea sequence and urea phantom results. (A) Bloch simulation of the excitation profile for the RF pulse alone; (B) zoomed views (±40 Hz) of excitation profiles at each metabolite frequency. The excitation pulse has a 6 ms duration, 60 Hz passband on urea (0 Hz), 40 Hz stopband with 0.4% ripples on pyruvate (240 Hz) frequency, 0.45% ripples on alanine (425 Hz), pyruvate hydrate (507 Hz), and lactate (635 Hz) frequencies. (C) The simulated excitation profile (red line) including the RF pulse and bSSFP sequence using the averaged magnetization of 64 pulses. The vertical green dot lines show the frequency locations of banding artifacts. (D) Zoomed views (±40 Hz) of excitation profiles at each metabolite frequency. (E) ^{13}C urea phantom images. The gray circles and arrows show the location of the urea phantom. The normalized signals of urea phantom measurements are indicated pointed by the blue cross points. The experimental results showed excellent agreement with simulation.

The steady state magnetization of the bSSFP sequence is sensitive to the off-resonance frequencies that cause dephasing within the repetition time (TR) and cause banding artifacts that occur

periodically at intervals of $\pm \frac{1}{2TR}$.[23] A longer TR allows longer readouts with higher SNR efficiency, but is more sensitive to the off-resonance frequencies. In this sequence, the optimal TR was set as 12.26 ms to maximize the distance between the banding artifacts frequencies and the other metabolite frequencies. Meanwhile, the banding artifacts can be suppressed by a larger flip angle, but the optimal flip angle of bSSFP sequence is smaller in the short T_2 tissues (Figure 5.3A). To compare the bSSFP sequence and GRE sequence, the flip angle of bSSFP was chosen as 50°, whose effective flip angle equaled to the optimal flip angle of GRE (25°), providing a tradeoff between banding artifacts and residual magnetization for dynamic metabolic imaging. This 3D bSSFP urea sequence was implemented on a 3T GE MRI scanner (MR750, GE Healthcare, Waukesha, WI, USA) using an additional scanner control commercial software (RTHawk Research, HeartVista, Los Altos, CA, USA) to implement the bSSFP sequence for [^{13}C,$^{15}N_2$]urea acquisition and the metabolite-specific 2D-GRE sequence for acquisition of haptoglobin (HP) [1-^{13}C]pyruvate and its metabolites.

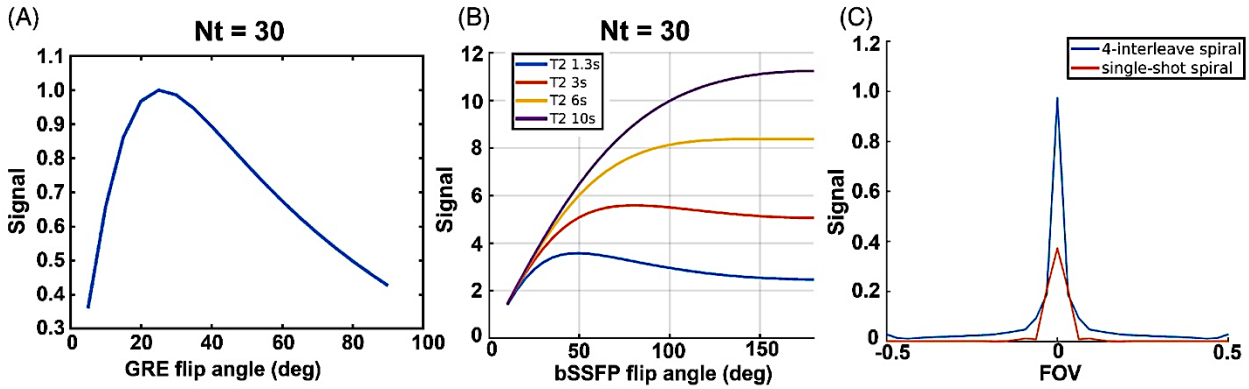

Figure 5.3: (A,B) Simulations of GRE and bSSFP urea AUC signal with 30 time points and a 3 s temporal resolution. (C) Simulated PSFs of a 4-interleave spiral readout as used in the bSSFP sequence and single-shot spiral readout as used in the GRE sequence for [^{13}C,$^{15}N_2$]urea with J_{CN} splitting frequencies (±20 Hz).

The RF pulse excitation profile was calculated using Bloch simulation. The simulation parameters were 6 catalyzation RF pulses with ramp increasing flip angles, T_1 = 30 s, T_2 = 1 s,

TR = 12.26 ms, number of TR = 64, and flip angle = 50°. The excitation profile shown in Figure 5.2C is the averaged transverse magnetization of all bSSFP acquisitions.

The GRE and bSSFP signal in a dynamic urea acquisition were simulated using analytic models.[24] The simulation parameters of the GRE sequence were T_1 = 30s, readout duration = 22 ms, TR = 3 s, time points = 30. The simulation parameters of bSSFP sequence were readout duration = 4 ms, TR = 12.26 ms, T_1 = 30 s, number of TR per time point = 64, temporal resolution = 3 s, time points = 30. The simulated area under curve (AUC) signals are shown as a function of applied flip angles in Figures 5.3A,B and normalized by the maximum signal of the GRE sequence.

The point spread functions (PSF) with J_{CN} splitting frequencies of [^{13}C,^{15}N$_2$]urea were simulated for the 4-interleaved spiral readout used in the bSSFP sequence and the single-shot spiral readout used in the GRE sequence. The simulation parameters were J_{CN} coupling frequencies = ±20 Hz, peak ratio = 1:2:1, readout duration of 4-interleaved spiral = 4 ms, readout duration of single-shot spiral = 22 ms, sampling rate = 200 kHz. The PSF of 2 spiral readouts are shown in Figure 5.3C.

5.3.2 Phantom Experiment

To measure the excitation profile of the RF pulse, phantom experiments were performed on a ^{13}C-enriched sodium 8 M urea phantom (diameter = 1 cm, length = 6.5 cm) doped with a Gd-based contrast agent ($T_1 \approx 1$ s) with a single-channel ^{13}C transceiver birdcage coil. The ^{13}C images were acquired at the frequencies of bicarbonate, urea, pyruvate, alanine, pyruvate hydrate, and lactate. For bicarbonate and urea frequencies, ^{13}C images were acquired with a frequency offset from −20 to

20 Hz. For the frequencies of other 4 metabolites, ^{13}C images were acquired with a frequency offset from −40 to 40 Hz. In this acquisition of phantom study, the frequency step size was set as 10 Hz. Other main parameters included diameter of urea phantom = 1 cm, resolution = 1×1 cm^2, TR = 500 ms, flip angle = 50°, and number of signal averages = 400.

5.3.3 Animal Experiment

The co-hyperpolarized [1-^{13}C]pyruvate and [^{13}C,$^{15}N_2$]urea animal study was performed on a healthy adult Sprague Dawley rat (490 g, 24 weeks old) with 2 identical injections of co-hyperpolarized [1-^{13}C]pyruvate and [^{13}C,$^{15}N_2$]urea to compare the metabolite-specific 3D bSSFP sequence (3D-bSSFP) with metabolite-specific 2D-GRE sequence. All animal experiments were performed according to the University of California, San Francisco Institutional Animal Care and Use Committee (IACUC) approved protocols. All animal data were acquired by a $^1H/^{13}C$ transceiver single channel birdcage coil.

The co-hyperpolarized [1-^{13}C]pyruvate and [^{13}C,$^{15}N_2$]urea imaging contrast agents were prepared and polarized as previously reported.[15] Briefly, 0.378 g [^{13}C,$^{15}N_2$]urea (ISOTEC MilliporeSigma, Burlington, MA, USA) prepared in sterile water (9.6 M) with AH111501 sodium salt (12.5 mM) was loaded in a cryovial first. Subsequently, a mixture of 1.098 g [1-^{13}C]pyruvic acid (ISOTEC, MilliporeSigma) and AH111501 (12.5 mM in pyruvic acid) was loaded to the cryovial on the top of [^{13}C,$^{15}N_2$]urea. The resulting mixture was loaded into a 5T SPINlab system (GE Healthcare) and polarized at 0.8 K with 139.96 GHz microwaves for ~5 h. After polarization, the polarized frozen sample was rapidly dissolved in 41 mL pressurized superheated (130°C) sterile water and then neutralized by a buffer solution prepared as a mixture of 13.5 g of neutralization media consisting of

NaOH (600 mM) and Tris (333 mM) and 19.0 g of sterile water to produce a hyperpolarized [1-^{13}C]pyruvate and [^{13}C,$^{15}N_2$]urea solution with pH of 7.2-7.5. The final concentrations of formulation are pyruvate 146.3-153.9 mM, urea 33.5-37.7 mM, Tris ~66.6 mM. The osmolality measured by a micro osmometer (μ OSMETTE, Precision Systems, Natick, MA, USA) is ~390 (mOsm/kg H_2O). For each scan, the rat was intravenously injected with 2.5 mL of the solution via tail vein in 12 s. The rat's respiration was checked before and after injection.

The sequence parameters of co-hyperpolarization study for the animal experiments were shown in Table 5.1. The signal of [1-^{13}C]pyruvate and its downstream metabolite [1-^{13}C]lactate were acquired by the metabolite-specific 2D-GRE sequence in both injections. ^{13}C-urea signal was acquired by the metabolite-specific 3D-bSSFP in the first injection (experiment A) and the metabolite-specific 2D-GRE in the second injection (experiment B).

The metabolite-specific 2D-GRE sequence consists of a spectral-spatial excitation pulse,[25] single-shot spiral readouts, and spoiler gradients. The parameters of RF pulse include the pulse duration 25.17 ms, passband 80 Hz, and stopband 770 Hz. The readout gradient is a single-shot spiral gradient with 22 ms duration. The spatial resolution, temporal resolution, and total acquisition time points were kept the same for both injection experiments. The acquisitions were automatically triggered at 5 s after the injection started. In each acquisition, the frequency of [1-^{13}C]pyruvate was calibrated before imaging acquisition, which was automatically triggered at 5 s after the start of injection.[26] A real-time B_1^+calibration[27] was performed following the frequency calibration in experiment A. In experiment B, the acquisition was the same except that the B_1 scaling was not updated, but fixed to the value in experiment A for comparison consistency.

Table 5.1: A summary of ^{13}C sequence parameters used in animal study and human study. (a) For the animal study, two experiments (A and B) were performed to compare urea signal acquired by 2 sequences. In experiment A, urea signal was acquired with metabolite specific 3D-bSSFP sequence, whereas pyruvate and lactate signals were acquired with metabolite specific 2D-GRE sequence. In experiment B, all metabolite signals were acquired by metabolite specific 2D-GRE sequence. (b) For the human study, urea data was acquired by metabolite specific 3D-bSSFP sequence for validating feasibility. Immediately following imaging, 2 ^{13}C spectra data were acquired for calibration measurements. (FOV = Field of View).

(a) Sequence parameters for animal experiments		
	Experiment A	Experiment B
Pyruvate Lactate	Metabolite-Specific 2D-GRE, lactate to pyruvate frequency 395Hz, FOV 8×8×21cm, resolution 2.5×2.5×21mm, Tread 22ms, TR 100ms, temporal resolution 3s, flip angle 10° for pyruvate, flip angle 30° for lactate, 30 timepoints	
Urea	Metabolite-Specific 3D-bSSFP, urea to pyruvate frequency -240Hz, FOV 8×8×33.6cm, resolution 2.5×2.5×21mm, Tread 4ms, TR 12.26ms, flip angle 50°	Same sequence as pyruvate and lactate except urea to pyruvate frequency -240Hz, flip angle 25° for urea
(b) Sequence parameters for human study		
Pyruvate Lactate	Metabolite-Specific 2D-GRE, lactate to pyruvate frequency 395Hz, FOV 22.4×22.4×11.6cm, resolution 7×7×11.6mm, Tread 22ms, TR 80ms, temporal resolution 2.6s, flip angle 15° for pyruvate, flip angle 30° for lactate, 20 timepoints	
Urea	Metabolite-Specific 3D-bSSFP, urea to pyruvate frequency -240Hz, FOV 21.7×21.7×18.56cm, resolution 7×7×11.6mm, Tread 4ms, TR 12.26ms, flip angle 50°	
Frequency Calibration & Spectrum Acquisition	Slice-selective spectrum, slice thickness = 3cm, TR 150ms, flip angle 3° for calibration before metabolite imaging acquisition, flip angle 90° for spectrum acquisition after metabolite imaging acquisition	
B_1^+ Mapping	Pyruvate-specific 2D-GRE with Bloch-Siegert pulse, FOV 33.6×33.6 cm, resolution 11.2×11.2 mm, slice thickness = 3cm, TR 200ms, flip angle 8^0, $\omega_{RF} \pm 4.5$ kHz	

5.3.4 Human Clinical Study

To demonstrate imaging feasibility of the optimized 3D-bSSFP urea sequence acquisition strategy in patients, a pre-surgical patient with histologically confirmed localized prostate cancer was recruited and consented after obtaining FDA IND (IND 109956) and University of California San Francisco (UCSF) Institutional Review Board approval.

The formulation and composition of co-hyperpolarized [1-^{13}C]pyruvate and [^{13}C,$^{15}N_2$]urea solution for the human clinical studies were identical as the above-mentioned animal studies, but was performed using Good Manufacturing Practices (GMP) products under aseptic conditions in an ISO 5 environment with specific pharmacy kits (GE Healthcare). The mixture was loaded and polarized using an automated hyperpolarizer and quality control instrument of 5 T SPINlab polarizer (GE Healthcare) for 4.35 h before rapidly dissolved with 41 mL of 130°C sterile water and forced through a mechanical filter to remove electron paramagnetic agent (EPA). The solution was subsequently neutralized using equivalent NaOH and Tris (hydroxyethyl) aminomethane. The receive assembly that accommodated quality-control processes provided rapid measurements of pyruvate concentration (176 mM), pH (7.7), EPA concentration (0.8 μM), temperature (37.4^{0}C), and hyperpolarization (36.5%) before the injection. In parallel, the co-hyperpolarized probe went through an integrity of the 0.2 μm sterile filter (Saint-Gobain Life Sciences, Solon, OH, USA). Finally, the co-hyperpolarized probes were injected at a dosage of 0.43 mL/kg body weight with a rate of 5 mL/s followed by a 20 mL saline flush at 5 mL/s.

The co-hyperpolarization human clinical study was performed on a 57-year-old man with a biopsy-proven prostate adenocarcinoma (Gleason score 4 + 5 = 9) located posteriorly in the peripheral zone of the mid-portion and apex of the prostate on the left. The ^{1}H/^{13}C imaging data from the human prostate was acquired using a clamshell transmit coil for signal excitation and a double-tuned ^{1}H/^{13}C endorectal coil for signal reception. The transmit gain of the coil was calibrated by a

non-selective spectrum pre-scan using a built-in urea phantom (Supporting Information Figure 5.S8). The parameters for ^{13}C data acquisition are shown in Table 5.1. Data acquisition started at 8 s after injection of co-polarized [1-^{13}C]pyruvate and [^{13}C,$^{15}N_2$]urea and saline flush was completed. A real-time [1-^{13}C]pyruvate frequency calibration was performed over the region of the prostate before the perfusion/metabolic images were acquired. A single slice Bloch-Siegert B_1^+ map was acquired as a reference, but was not used to update the transmit gain. With the acquisition design used for the animal study in experiment A, the [1-^{13}C]pyruvate and [1-^{13}C]lactate data were acquired using a metabolite-specific 2D-GRE sequence and [^{13}C,$^{15}N_2$]urea data using the metabolite-specific 3D-bSSFP urea sequence. After dynamic metabolic imaging, a spectral profile was acquired from the whole prostate volume to measure the frequencies of all the metabolites in vivo.

5.3.5 Reconstruction and Data Analysis

All data were processed using MATLAB 2021a (The MathWorks, Natick, MA, USA). Spiral data were gridded using a Kaiser–Bessel gridding method[28] (http://web.stanford.edu/class/ee369c/mfiles/gridkb.m). For the animal studies, the k-space data were directly inverse Fourier transformed to the image domain after gridding. For the human study, a bulk off-resonance correction was applied during the reconstruction process. The off-resonance frequencies of different metabolites were measured from the frequency calibration data and the spectrum acquisition data. To overlay the ^{13}C images on the proton localizer images, the reconstructed images were 0-padded to match the resolution of fast spin echo (FSE) images with a 2D fermi filter to reduce truncation artifacts. The lactate-to-pyruvate ratio images were measured by the division of lactate AUC images to pyruvate AUC images with flip angle compensation. Hyperpolarized spectra were apodized by a Lorentzian function in time domain before applying Fourier transform.

In the phantom study, the signals of phantom voxel were measured by the AUC of the complex data. The signals at all offset frequencies were normalized by the signal at urea on-resonance frequency.

In the animal study, the AUC images and dynamic signals were normalized according to the concentrations of [1-^{13}C]pyruvate and [^{13}C,$^{15}N_2$]urea between 2 injections measured using a ^{13}C-NMR spectrometer and the noise levels calculated using the mean of signals in the last time point of each metabolite data. The dynamic signals were measured by the region of interest (ROI) on the right kidney of the rat.

In the human study, the AUC images and dynamic signals were normalized by the mean of noise at the last time point of each metabolite data. The dynamic signals of all metabolite data were measured using symmetrical ROIs placed on regions of healthy- and malignant appearing prostate on T_2 and diffusion weighted images. For display, the urea phantom in the endorectal coil has been masked in the urea dynamic images.

5.4 Results

5.4.1 Excitation Simulation and Phantom Imaging

The Bloch simulated excitation profile of the 3D-bSSFP urea sequence using the averaged transverse magnetization over all readouts are shown in Figure 5.2C. The banding artifacts (green dash lines) are separated from the other metabolites by at least 36 Hz for pyruvate, 24 Hz for alanine, and 23 Hz for pyruvate hydrate and lactate. For the 50° excitation simulated here, a ±20 Hz frequency shift leads to a 21% signal intensity increase for urea. Because the frequency difference between the resonance of central [^{13}C, $^{15}N_2$]urea and bicarbonate is only 82 Hz, the RF pulse is unable to suppress

excitation at bicarbonate frequency with a reasonably short pulse duration. In the simulation, the excitation signal intensity at bicarbonate frequency is 50.5% of that of urea.

A urea phantom study was performed for validating the excitation profile of the 3D-bSSFP urea sequence by measuring the signal intensity under different excitation frequencies in the Figure 5.2E. Overall, these showed excellent agreement with simulation results. The pyruvate hydrate phantom image has a blurring artifact, which we believe was caused by the transient excitation from the nearby banding artifact of the sequence.

The levels of all the metabolites signals () in the 3D-bSSFP urea sequence were estimated by the concentration ratio () between all metabolites, the stopbands (δ) of the bSSFP signal response, and the of the proposed readout at different offset frequencies with the equation .[21] Based on experiment B of the animal study, the concentration ratio of lactate to pyruvate was estimated by the signal level with a flip angle compensation (). The molar concentration ratio of pyruvate to urea was measured by NMR spectroscopy (). The stopband amplitudes were measured in the phantom study as 0.9% for pyruvate and 0.1% for lactate. The simulated off-resonance PSF amplitudes of the proposed readout were 0.197 for pyruvate and 0.085 for lactate (Supporting Information Figure 5.S1). Therefore, the signal level of undesired metabolites when imaging urea using the proposed 3D-bSSFP sequence were 0.75% for pyruvate and 0.002% for lactate.

To compare the signal response between 2 sequences, [^{13}C,$^{15}N_2$]urea signal was simulated and point spread analysis was performed for GRE and bSSFP sequences. For the GRE sequence, the AUC signal only depends on T_1 and flip angle. The total signal reaches its highest value when excited by a 25° flip angle, the same value used for our in vivo experiments. Meanwhile, the AUC signal of bSSFP sequence commonly depends on T_1 and T_2 and flip angle. In vivo [^{13}C,$^{15}N_2$]urea has a relatively long T_2, with T_2 = 1.3 s measured in the vascular pool, T_2 values of 3 s to 10 s in the kidneys.[29] As shown in Figure 5.3B, the optimal flip angle increases with a longer T_2. The 50° flip angle used for

our in vivo experiments is near optimal for the shortest T_2 = 1.3 s, but these results suggest that larger bSSFP flip angles may improve SNR if the urea T_2 is longer. The PSF in Figure 5.3C shows the signal response of short and long readout duration of spiral readouts used in the bSSFP and GRE sequences, respectively. The peak PSF amplitudes are 0.974 for bSSFP and 0.373 for GRE, whereas the full-width half-maximum (FWHM) are ±0.02 FOV for bSSFP and ± 0.05 FOV GRE. This demonstrates the severity of blurring introduced by the J-coupling of [^{13}C,$^{15}N_2$]urea in the presence of long readout durations.

5.4.2 Animal Imaging

In the animal study, we compared HP ^{13}C imaging results from 2 acquisition methods using 3D-bSSFP and 2D-GRE sequences on a rat's kidney, liver, and cardiac slices (Figure 5.4). In the comparison of the urea AUC maps between experiment A and experiment B, no banding artifacts in the 3D-bSSFP images were observed. These could be ascribed to the loss of urea signal or spiral off-resonance artifacts if other metabolites were excited. This is consistent with the measured B_0 map, because the frequencies of the tissues in all 3 organ slices fell in the span of banding artifact frequency ($\Delta B_0 < \pm \frac{1}{2TR} = \pm 40$ Hz). In the field map, the heart slice exhibits a much larger B_0 inhomogeneity. In 2D-GRE sequence, the readout time was 22 ms, which is much longer than 4 ms of 3D-bSSFP sequence. Therefore, in the 2D-GRE images, the heart has a more severe off-resonance blurring artifact, whereas in the 3D-bSSFP images, the heart has a sharper edge that corresponds better with the anatomic image. Comparing the kidneys and liver slices in 2 experiments, the vessel signals in the pyruvate images appear identical, but the vessel signals in the urea images are different—more blurred vessel signals were observed with the 2D-GRE urea acquisition. The B_0 maps showed an accurate resonance frequency in the kidneys and liver slice. Therefore, the blurred vessel signals were caused

by the J_{CN} dephasing of [^{13}C,^{15}N$_2$]urea during the readout,[13,14] which agrees with a larger resolution loss of GRE simulated in Figure 5.3B.

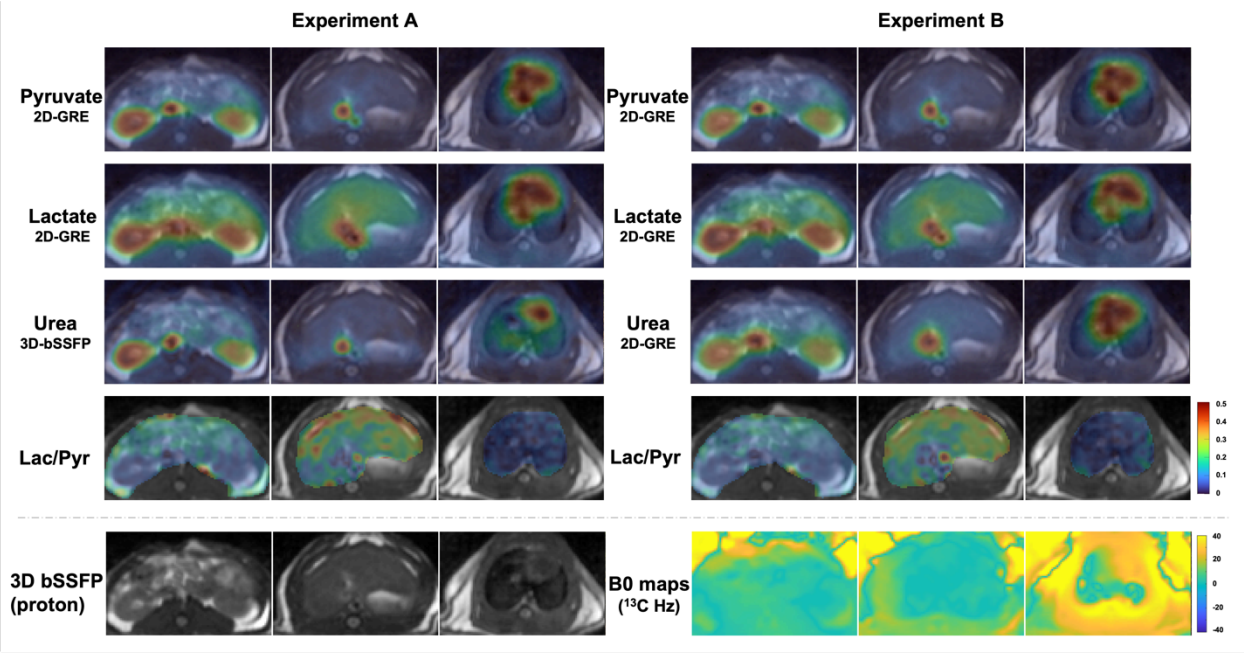

Figure 5.4: Comparison of the 3D-bSSFP urea sequence with a 2D-GRE sequence on a healthy Sprague Dawley rat: experiment A (pyruvate/lactate 2D-GRE, urea 3D-bSSFP) and experiment B (pyruvate/lactate/urea 2D-GRE) AUC images. Each AUC image is scaled by its own maximum signal to visualize metabolite distribution. Lactate-to-pyruvate AUC ratio images are displayed with the fixed scale range [0, 0.5]. The 3D-bSSFP urea sequence shows improved image quality compared to the MS-GRE sequence, with better delineation of the vasculature, kidneys and heart because of the shorter readout length.[15,21] The 2D-GRE sequence particularly suffers from more severe blurring artifacts in the heart than the 3D-bSSFP sequence where there is larger $\mathbf{B}_0$ inhomogeneity. Even when $\mathbf{B}_0$ inhomogeneity is small, the vessel signal acquired by 3D-bSSFP has a sharper edge in the kidneys and liver slices than data acquired by 2D-GRE because of the J_{CN} coupling of [^{13}C,^{15}N$_2$]urea.

The dynamic curves and dynamic renal images acquired by the 2D-GRE and 3D-bSSFP urea sequences were compared in Figure 5.5. The vessel is sharper acquired by the 3D-bSSFP sequence as was also shown in the AUC images. With a shorter readout time, the 3D-bSSFP sequence suffers less from off-resonance and J-coupling artifacts compared to the 2D-GRE sequence.

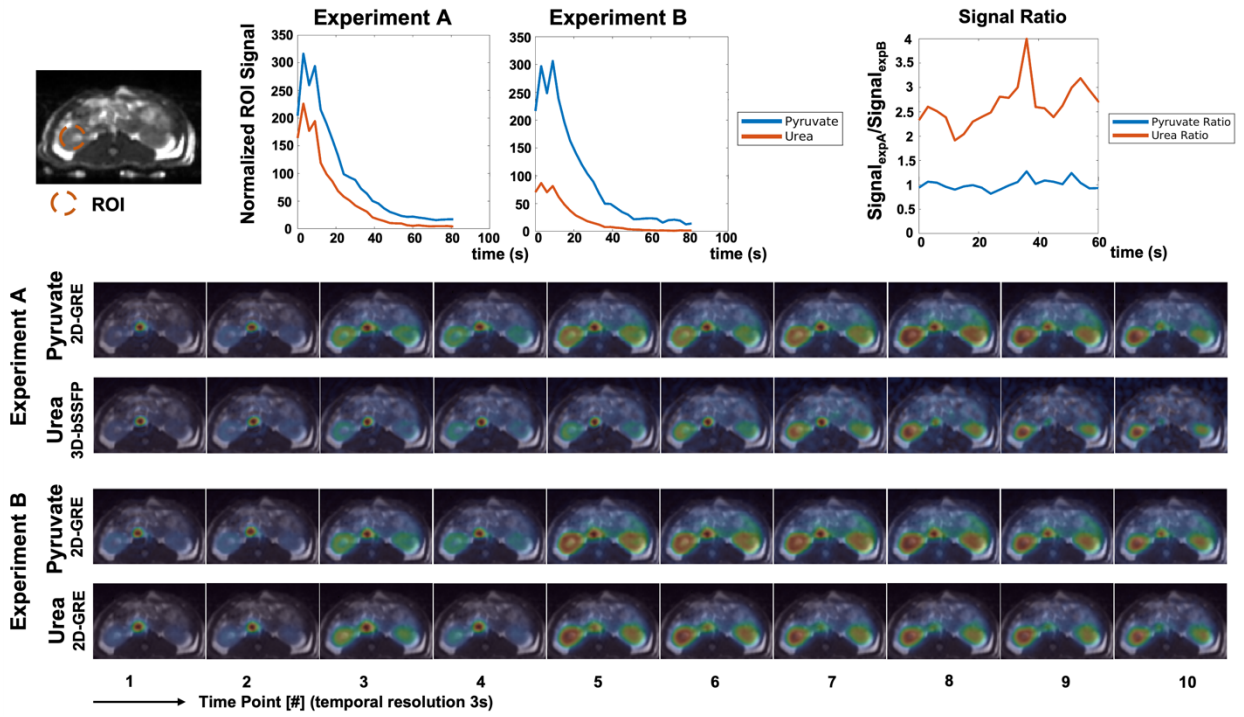

Figure 5.5: Comparison of the 3D-bSSFP urea sequence with a 2D-GRE sequence with dynamic kidney images of a healthy Sprague Dawley rat. Experiment A (pyruvate/lactate 2D-GRE, urea 3D-bSSFP) and experiment B (pyruvate/lactate/urea 2D-GRE) were described in the methods. Dynamic curves of pyruvate and urea signals and their signal ratios were measured on the ROI region in the kidney region. All signals have been normalized by the concentration measured by ^{13}C NMR spectrometer of each injection and corresponding noise levels. The urea signal levels were further divided by a factor of 4 according to the concentration equivalence of probes to present in the plots. Each dynamic figure is displayed with an independent color scale. The 3D-bSSFP urea sequence shows an ~2.5× SNR improvement over the 2D-GRE urea sequence.

As shown in Figure 5.5, compared to the 2D-GRE urea sequence, the 3D-bSSFP urea sequence shows an ~2.5× SNR improvement over the 2D-GRE urea sequence, demonstrating a substantial improvement in performance. Furthermore, the SNR improvement is consistent across the acquisition, indicating no incidental saturation of pyruvate or accelerated urea signal loss because of the 3D-bSSFP urea sequence. The 3D-bSSFP urea sequence also has a similar signal decay rate as that of the 2D-GRE pyruvate signal.

5.4.3 Human Imaging

In the human prostate cancer study, a real-time frequency calibration was applied to calibrate based on the pyruvate frequency before the metabolite imaging acquisition. Figure 5.6C shows the spectrum profile of the frequency calibration. As shown in the first pyruvate image in Figure 5.6B, after the frequency calibration, both the right recto-prostatic angle and left femoral vessels regions have high signal. This was 8 s after the end of injection. Meanwhile, the B_0 map (Figure 5.6A) shows the ^{13}C off-resonance frequency in the left femoral vessels region has a 20 Hz shift compared to the prostate region. Therefore, the spectrum data in the Figure 5.6C has 2 peaks with 20 Hz difference. However, because of the higher signal in the left femoral vessels region when the pyruvate frequency was calibrated, there was an inadvertent offset in the prostate region. This was identified through the measurements shown in Figure 5.6C, and the frequency offset was corrected in the prostate region. Furthermore, 20 Hz shift is still within the passbands/stopbands of the imaging acquisitions.

Because of being the first clinical human study, 1 more slice-selective ^{13}C spectrum data was acquired after the metabolite imaging to check the in vivo frequencies of all the metabolites. The spectrum profile is shown in Figure 5.6D. The frequency differences of urea to pyruvate, alanine to pyruvate, and lactate to pyruvate were −244.6 Hz, 195.7 Hz, and 401.1 Hz, respectively.

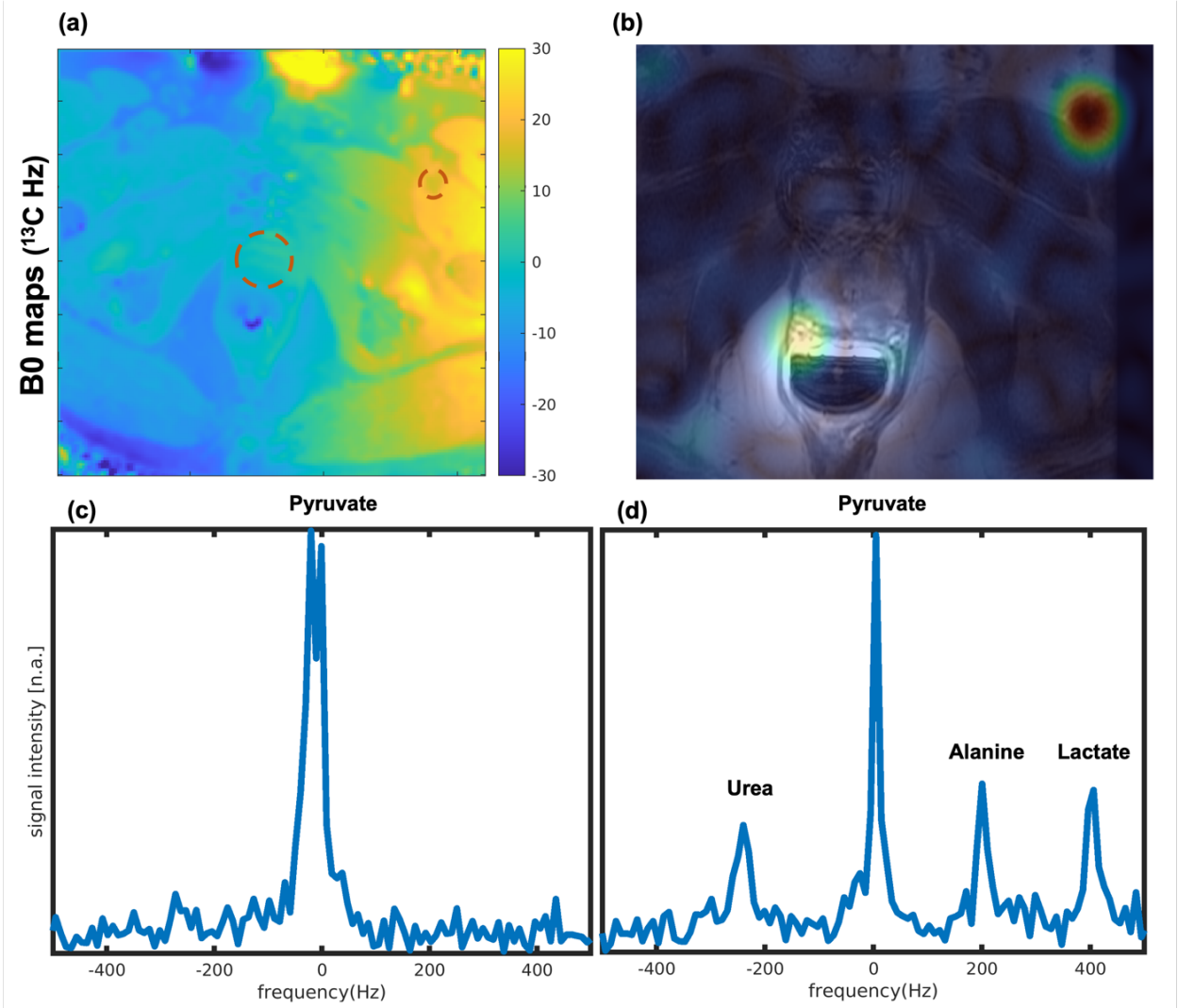

Figure 5.6: Co-hyperpolarized [1-^{13}C]pyruvate and [^{13}C, ^{15}N2]urea human imaging study. (A) $\mathbf{B}_0$ field map (scaled to ^{13}C frequency), (B) pyruvate image acquired after frequency calibration, and (C,D) The ^{13}C spectrum. The spectrum data before metabolite imaging acquisition in (C) has 2 [1-^{13}C]pyruvate peaks with 20 Hz difference. This can be explained by the $\mathbf{B}_0$ map in (A) that shows an off-resonance in the left superficial femoral vein region with 20 Hz shift compared to the prostate region, and the initial pyruvate images in (B) showing signal near the prostate and the left superficial femoral vein. The spectrum data after metabolite imaging acquisition in the (D) shows frequency of urea to pyruvate is −244.6 Hz, alanine to pyruvate is 195.7 Hz, and lactate to pyruvate is 401.1 Hz, with single peaks for each metabolite because of localization to the prostate region.

The AUC maps of pyruvate, lactate, urea, and lactate-to-pyruvate ratio images are shown in Figure 5.7. The T_2-weighted, DWI/ADC, and DCE images were used to clinically characterize the tumor. All 3 metabolite images show a higher AUC in the tumor than that in the contra-lateral healthy-

appearing prostate region. Comparing the pyruvate AUC images with urea AUC images, urea data shows higher relative signals in the vessels within the rectal wall. This phenomenon shows the difference in information between metabolite imaging and perfusion imaging.

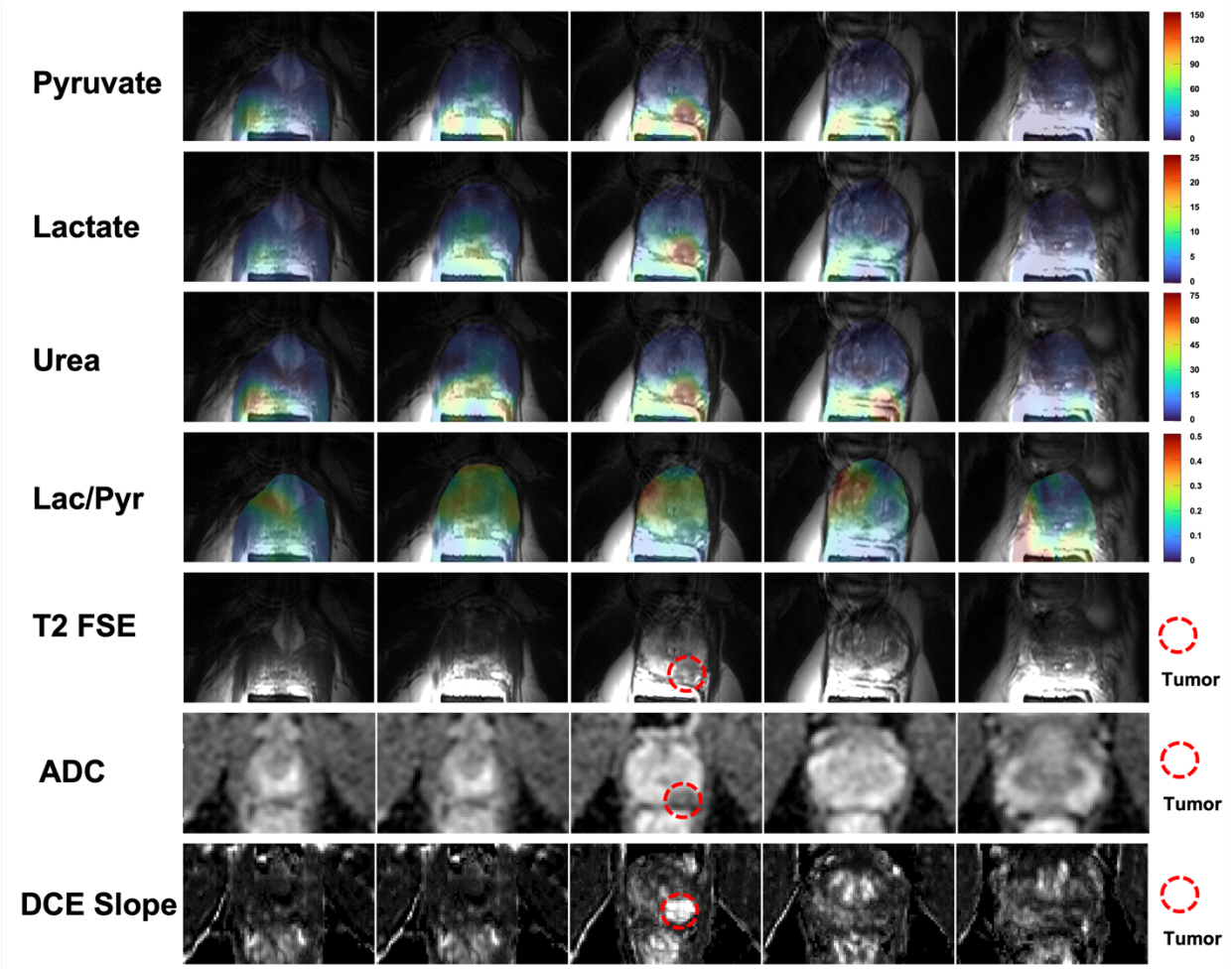

Figure 5.7: AUC maps of pyruvate, lactate, and urea, and lactate-to-pyruvate ratio images in the prostate across 5 slices. The biopsy-confirmed prostate tumor showed hypointensity on T2-weighted images, restricted diffusion on DWI/ADC, and early arterial enhancement on DCE images. All images of each metabolite used the same display range. The lactate-to-pyruvate ratio images were measured by the division of lactate AUC images to pyruvate AUC images with flip angle compensation. These show good image quality with no apparent artifacts.

The dynamic metabolite signal intensity over time curves between prostate tumor and contra-lateral prostate regions were shown in Figure 5.8. The [1-^{13}C]pyruvate and [1-^{13}C]lactate signals were acquired by the metabolite-specific 2D-GRE sequence and [^{13}C,^{15}N$_2$]urea signal was acquired by the

3D-bSSFP urea sequence. The tumor signals of both pyruvate and urea reach their peaks at around 10.4 s after acquisition. As to maximal signal intensity, the tumor voxel was ~2.5 times higher than the contralateral healthy-appearing prostate.

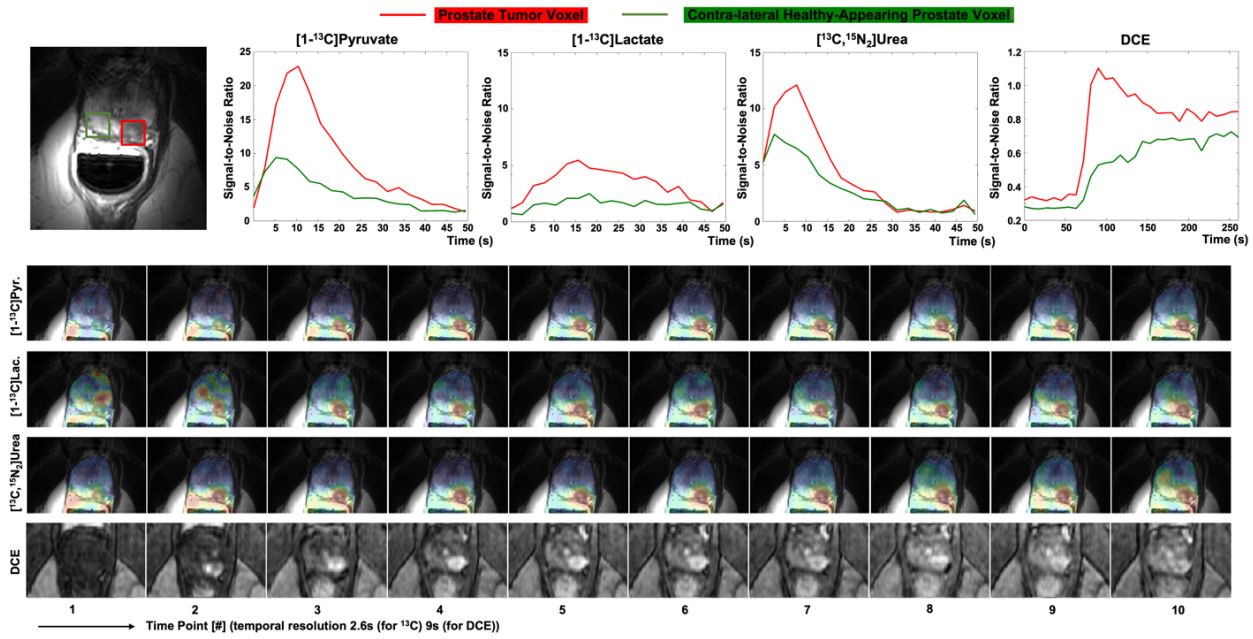

Figure 5.8: Dynamic prostate images with pyruvate, lactate, and urea signals, in SNR units and extracted dynamic curves of DCE images. Each dynamic figure is displayed with the independent color scale. The tumor signal of both pyruvate and urea reaches peak at around 10.4 s after acquisition. The signal peak of tumor voxel is ~2.5 times higher than the signal peak of the contralateral prostate voxel in urea data, which agrees with the signal peak shown in the DCE curve.

5.5 Discussion

5.5.1 Urea Excitation for the bSSFP Sequence

In the design of the urea-only excitation sequence, we used a short TR in the bSSFP sequence and constrained the multiband RF pulse (Figure 5.1) for spectrally selective excitation on urea frequency, while minimizing the excitation of other metabolites. We determined the minimum pulse duration to be 6 ms, which was constrained by the 240 Hz frequency difference between urea and

pyruvate at 3 T. The efficiency of the bSSFP urea sequence would be reduced by using a longer duration pulse that would be required for avoiding excitation at the bicarbonate frequency.

We optimized the TR of the bSSFP sequence according to the banding pattern and excitation profile of the RF pulse. In the ^{13}C bSSFP sequences, the banding can result in 2 types of artifacts: nulling of signals for the desired metabolite in the high-flip regime and exciting undesired metabolites in the low-flip regime for which we have observed ring-shaped artifacts. Therefore, we aimed at using a shorter TR for both a larger frequency interval of banding artifacts and a larger difference between the banding artifacts frequencies and the other undesired metabolite frequencies. Considering the feasibility of the pulse duration and readout duration, we chose 12.26 ms as the optimal TR of the bSSFP urea sequence.

Exciting undesired metabolites can introduce artifacts and reduce their magnetization. Comparing the AUC images in Figure 5.4 and the dynamic pyruvate signal ratio in Figure 5.5, there is no significant difference in pyruvate and lactate signals between using the 3D-bSSFP and 2D-GRE urea sequences. This is in good agreement with numeric simulation that estimate only 0.74% pyruvate and 0.002% lactate would be excited by the 3D-bSSFP urea sequence.

5.5.2 3D-bSSFP versus 2D-GRE

The 3D-bSSFP urea sequence is based on an interleaved spiral readout, which has a shorter readout duration than a single-shot spiral readout used in 2D-GRE sequence. This short readout duration can improve the efficiency of acquisition and provides a higher SNR in bSSFP sequence. Another advantage of short readout duration is to reduce the dephasing of the spins from J-coupling

and T_2^* effects, which can provide a higher signal intensity in bSSFP sequence, as shown in Figure 5.3C. A rough estimation of imaging SNR improvement in the dynamic imaging of bSSFP sequence to GRE sequence is shown in Figure 5.3A,B, which shows an expected improvement of 3× for bSSFP. However, this simulation does not account for spatial filtering and blurring differences because of J-coupling or flow and bolus effects, which could explain why the actual SNR improvement of 3D-bSSFP is lower than the simulation results. In the animal study, 3D-bSSFP urea sequence shows a 2.5× SNR improvement compared to the 2D-GRE sequence. This is very similar to the previous 3D-bSSFP lactate sequence results that showed a 2 to 2.5× SNR improvement compared to a 2D-GRE sequence. Owing to a relatively long T_2 (~1.3-10s) of [^{13}C,^{15}N$_2$]urea in vivo,[29] the transverse magnetization can be efficiently used in the 3D-bSSFP sequence for improving the SNR of the urea images. For example, in the human study (Figure 5.8), the ratio of the dynamic signal of pyruvate to urea is around 2× in the prostate tumor and 1.3× in the contra-lateral prostate region. With the flip angle compensation, the signal ratios become $2 \times \sin(50°/2)/\sin 15° = 3.27$ and $1.3 \times \sin(50°/2)/\sin 15° = 2.12$, both of which are smaller than the molar equivalent of pyruvate to urea of 4 in the injected solution.

We also noticed that both 3D-bSSFP sequence and 2D-GRE sequence are sensitive to B_0 inhomogeneity, and a good shimming before ^{13}C spiral acquisition is essential to improve the image quality. In the 3D-bSSFP sequence, the excitation intensity will be perturbed because of a limited excitation bandwidth and a small flip angle. In the 2D-GRE sequence, the off-resonance effects lead to the blurring artifacts because of the long readout time combined with the J_{CN} coupling (20 Hz) of [^{13}C,^{15}N$_2$]urea. Even with very good shimming, we still observed a blurring artifact in the vessel (Figure 5.4) because of dephasing from J_{CN} coupling (20 Hz) that was previously reported and cannot be eliminated.[15] As the comparison results demonstrated in the animal study, the bSSFP sequence

provides a new method to remove blurring artifacts caused by J-coupling splitting frequencies through an interleaved readout with a shorter TR, which was only addressed by multi-echo imaging in previous studies.[30]

5.5.3 Spiral Readout vs Cartesian Readout

We used an interleaved spiral readout gradient in the 3D-bSSFP urea sequence for accelerating the acquisition. This differs from the previous studies where [^{13}C,$^{15}N_2$]urea data were acquired by a SSFP sequence with Cartesian readout.[13, 14, 31] In these studies, only single slice [^{13}C,$^{15}N_2$]urea data were acquired with low temporal resolution. In our spiral readout acquisition pipelines, multi-slice [1-^{13}C]pyruvate, [1-^{13}C]lactate and 3D [^{13}C,$^{15}N_2$]urea data can be acquired one by one with 2.6 s temporal resolution.

5.5.4 Human Study

Our previous HP ^{13}C prostate cancer studies have used echo-planar readouts (EPI) for multiple metabolite dynamic imaging.[6, 32 -34] They had a set of typical parameters including matrix size 16 × 16, resolution 8 × 8 mm, and corresponding FOV is 12.8 × 12.8 cm. The spiral readout used in our acquisitions used a higher in-plane spatial resolution of 7 × 7 mm and larger FOV of 22 × 22 cm. As shown in Figure 5.6B and Supporting Information Figure 5.S3, 5.S5, and 5.S7, the increased FOV allows us to observe the left femoral vessels signal in the first 3 time points, providing a valuable information for analyzing the probe perfusion in the blood vessels, for example, by using the arterial input function (AIF) in the analysis.[35] This region is relatively far from the endorectal coil, which has dimensions of 2.5 × 8.5 cm, and this determined the FOV used in the prior studies. Despite the distance from the endorectal surface coil, the vessel had sufficiently high signal to observe the bolus arrival. Moreover, the spiral readout has shorter TE than the EPI readout and will improve the SNR

for ^{13}C metabolites with a shorter T_2^*. These advantages of a spiral readout provide the potential to improve spatial resolution and coverage for HP ^{13}C imaging.

Furthermore, we demonstrated the advancement of our sequences to the prior ^{13}C MRI prostate cancer studies, which relied on lactate-to-pyruvate conversion. As shown in Figure 5.7, we can now simultaneously observe lactate production, pyruvate perfusion, and urea perfusion. The hyperpolarized [^{13}C,$^{15}N_2$]urea is metabolically inert and almost exclusively experiences perfusion effects in vivo. However, the pyruvate, in addition to perfusion, is also metabolically active and undergoes cellular transport, so it is not an ideal measurement of perfusion. Therefore, the hyperpolarized [^{13}C,$^{15}N_2$]urea plays an important role of characterizing the perfusion, and through co-polarization can also provide a simultaneous measurement to pyruvate for analysis. In particular, the urea signal can potentially be used to correct the vascular pyruvate signals that will confound metabolism measurements based on tissue perfusion.

Compared to using 2 separate injections, the co-injection of [1-^{13}C]pyruvate and [^{13}C,$^{15}N_2$]urea is more practical to minimize effects from patient physiology differences, motion between scans, and provides data for more accurate perfusion and metabolic signal modeling. However, in consideration of the safety issue of high osmolality in the injection, lower concentrations of pyruvate and urea must be applied in co-injection studies compared to separate injections, leading to an expected lower SNR. Considering the concentration of urea is only a quarter of pyruvate, it is necessary to design a more efficient bSSFP acquisition method for [^{13}C,$^{15}N_2$]urea imaging. In addition, having more frequencies of metabolites present makes the spectral-selective RF pulse design and bSSFP sequence design more constrained.

One Bloch-Siegert B_1^+ map was acquired at the pyruvate frequency after the real-time frequency calibration. However, the pyruvate only has a high concentration in the vasculature in the early stage of the acquisition when calibration was performed. Therefore, the B_1^+ map could not be accurately measured in the prostate region. This could be improved by moving the real-time B_1^+ mapping in the middle of acquisition in the future.

A urea phantom was placed in the endorectal coil for calibration and was excited by the 3D-bSSFP urea sequence. Because of the short readout time, the edge of phantom image is quite sharp. From the image acquired at last time point after the hyperpolarization has decayed (Supporting Information Figure 5.S4), we determined that the phantom signal would not affect signal in the prostate region.

5.5.5 Limitations of Using 3D-bSSFP Sequence

For future human studies with co-hyperpolarized [1-^{13}C]pyruvate and [^{13}C,$^{15}N_2$]urea probes, we are aware of several important precautions in our data acquisition methods.

First, the short duration of the bSSFP RF pulse may lead to the signal contamination from bicarbonate, which has a small frequency to urea (−82 Hz at 3T). However, this is not a major concern for prostate imaging because of the low level of bicarbonate typically seen in the prostate and surrounding tissues.[32] ^{13}C-bicarbonate will appear later in the dynamic acquisition, therefore, reducing its effect on the urea signal particularly in the early time points that can be used for perfusion analysis. For the organs with high bicarbonate signal (i.e., brain and heart), a variable TR approach[36] or a quadratic RF phase[37] may be able to control the bicarbonate excitation profile developed in the MR-

fingerprinting acquisition.[38] Another possible approach is to add multi-echo technique in the acquisition and separate bicarbonate and urea signal in the reconstruction process.[39]

Second, because of the sensitivity of the bSSFP sequence to B_0 inhomogeneity, a real-time frequency calibration and shimming are crucial for good imaging quality. In the human prostate study, the high superficial femoral vein signal at the beginning of the acquisition affected the frequency calibration because of the field inhomogeneity. Therefore, local shimming should be applied to a FOV covering the entire region where ^{13}C signal maybe detected.

Third, the [^{13}C,$^{15}N_2$]urea signal was acquired by a 3D imaging acquisition, which are more sensitive to motion effects compared to 2D methods. In comparison, [1-^{13}C]pyruvate and [1-^{13}C]lactate signal were acquired by a 2D imaging that is very fast and robust with motion. To minimize the motion sensitivity, we used a center-out spiral acquisition that will reduce motion-related artifacts in 3D-bSSFP urea sequence.

Fourth, because the T_2 relaxation and excitation are different between pyruvate and urea, a more detailed model of the magnetization evolution will be useful to simultaneously analyze metabolic imaging of [1-^{13}C]pyruvate and perfusion imaging of [^{13}C,$^{15}N_2$]urea.

Last, to the advantage of longer T_2 values, the 3D bSSFP urea sequence could use larger flip angles to provide a larger expected SNR improvement (Figure 5.3B). In this study, we used a 50° flip angle to match to the effective GRE flip angle. Because the T_2 value is variable among different tissues,[29] optimization of flip angle for the different anatomies is worthwhile to improve future human studies.

5.6 Conclusion

We have developed a highly efficient method for imaging co-hyperpolarized ^{13}C pyruvate and urea for human studies. Using a metabolite-specific bSSFP strategy with RF pulses and a TR optimized for urea provided ~2.5-fold improvement in SNR compared to a GRE approach because of the repeated usage of the transverse magnetization. Furthermore, bSSFP had reduced blurring artifacts in vivo because of short readout durations, whereas the *J*-coupling of [^{13}C,$^{15}N_2$]urea leads to noticeable blurring with GRE methods. The dynamic urea perfusion imaging capability was not affected by the bSSFP method, and ^{13}C pyruvate imaging, performed with a metabolite-specific GRE approach, was also not affected by the bSSFP method. Finally, we demonstrated excellent results in the first-in-human study using co-hyperpolarized ^{13}C pyruvate and urea, which is both the first-time multiple agents have been injected into a human as well as the first non-pyruvate agent used in a human subject. This work lays the foundation for future human studies to achieve high-quality, high-SNR, simultaneous metabolism, and perfusion imaging.

Supplemental Information:

Animal Experiment Supplemental Methods

The rat was cannulated in the lateral tail vein and anesthetized with 1-2% isoflurane/100% oxygen at a rate of 1 L/min. During the experiment, the anesthetized rat, with respiration rate at ~ 60-80/min was secured on a warm water heating pad at 37° C. The catheter was flushed periodically with 100μL of 8IU/mL heparin in normal saline every 20 minutes to prevent clotting.

After the hyperpolarized 13C imaging studies, an anatomical localizer was acquired by proton bSSFP sequence (FOV 16×16×12cm3, resolution 1×1×2mm3). In addition, the B0 field map was acquired by proton IDEAL IQ sequence (FOV 20×20cm2, resolution 1.25×1.25×10mm3) with local shimming. The shimming values were also used for 13C data acquisition.

After the hyperpolarized experiment, the concentrations of [1-13C]pyruvate and [13C,15N2]urea were determined using a calibration curve, which correlates the NMR signal intensities and the concentrations of standard solutions of [1-13C]pyruvate and [13C, 15N2]urea in the range of 40-160mM and 10-40mM, respectively. The NMR data were acquired using a 400MHz (proton) 2-channel NMR spectrometer (Bruker Avance III HD 400) equipped a standard probe - 5 mm BBFO Z-gradient SmartProbe with automatic tune and match. All the data were acquired under the identical settings in the aspects of experiment, width, and receiver with the main parameters.

Human Clinical Study Supplemental Methods

Proton anatomical images were acquired with a 2D fast spin echo (FSE) sequence with an FOV of 18×18×7.2cm3 and a resolution of 0.47×0.47×3mm3. The B0 field maps were measured using an IDEAL IQ sequence (FOV 48×48cm2, resolution 1.25×1.25×10mm3, 7 slices) and localized gradient shimming of the selected prostate volume to improve the B0 field homogeneity prior to the

hyperpolarized 13C MR acquisition. In addition to the T2 weighted anatomic images, diffusion weighted imaging (DWI) data (FOV 18×9cm2, resolution 1.4×1.4×3mm3, b = 1350s/mm2, 6 directions) and dynamic contrast-enhanced (DCE) data (FOV 26×26cm2, resolution 1.35×2×3mm3, temporal resolution 9s) were acquired to identify regions of prostate cancer based on reduced T2 and apparent diffusion coefficient (ADC) in regions of cancer relative to surrounding benign tissues.

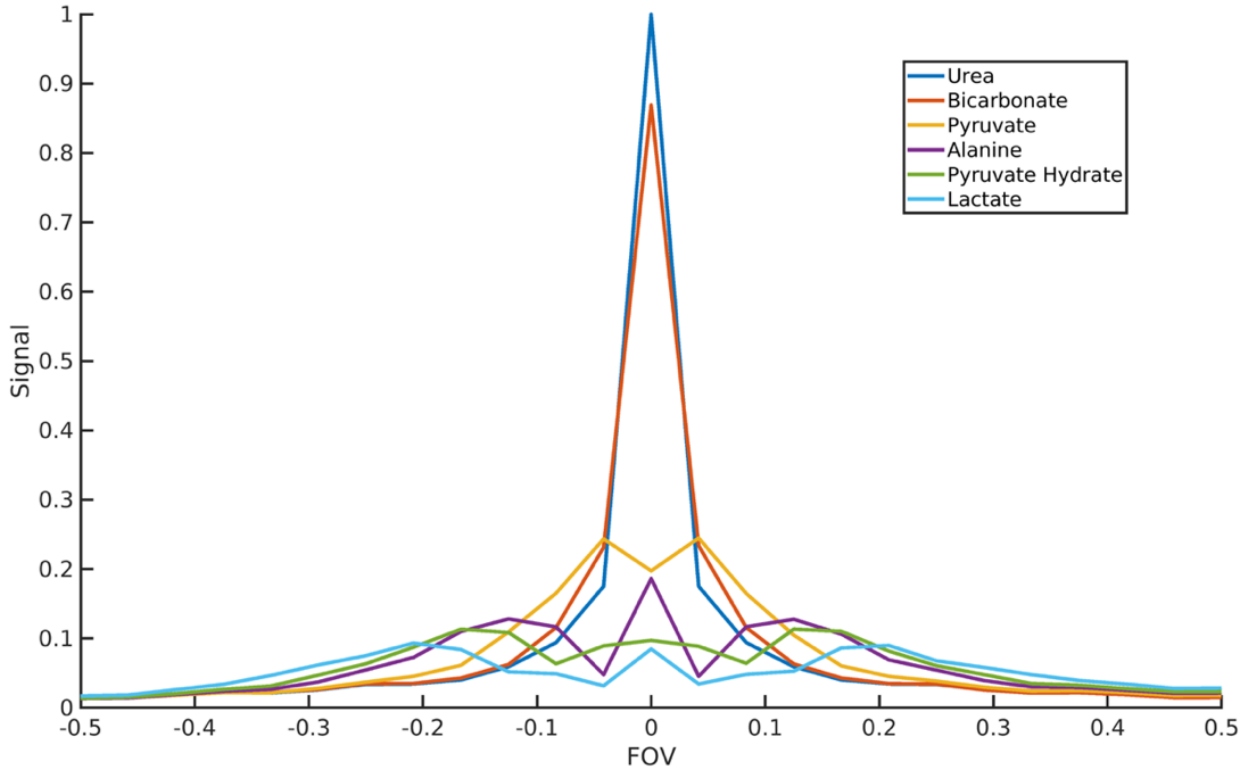

Figure 5.S1: Simulations of off-resonance PSF of stack-of-spiral readouts with 4 interleaves, 4ms readout. Frequencies of each metabolite are urea at 0Hz, bicarbonate at -82Hz, pyruvate at 240Hz, alanine at 425Hz, pyruvate hydrate at 507Hz, and lactate at 635Hz.

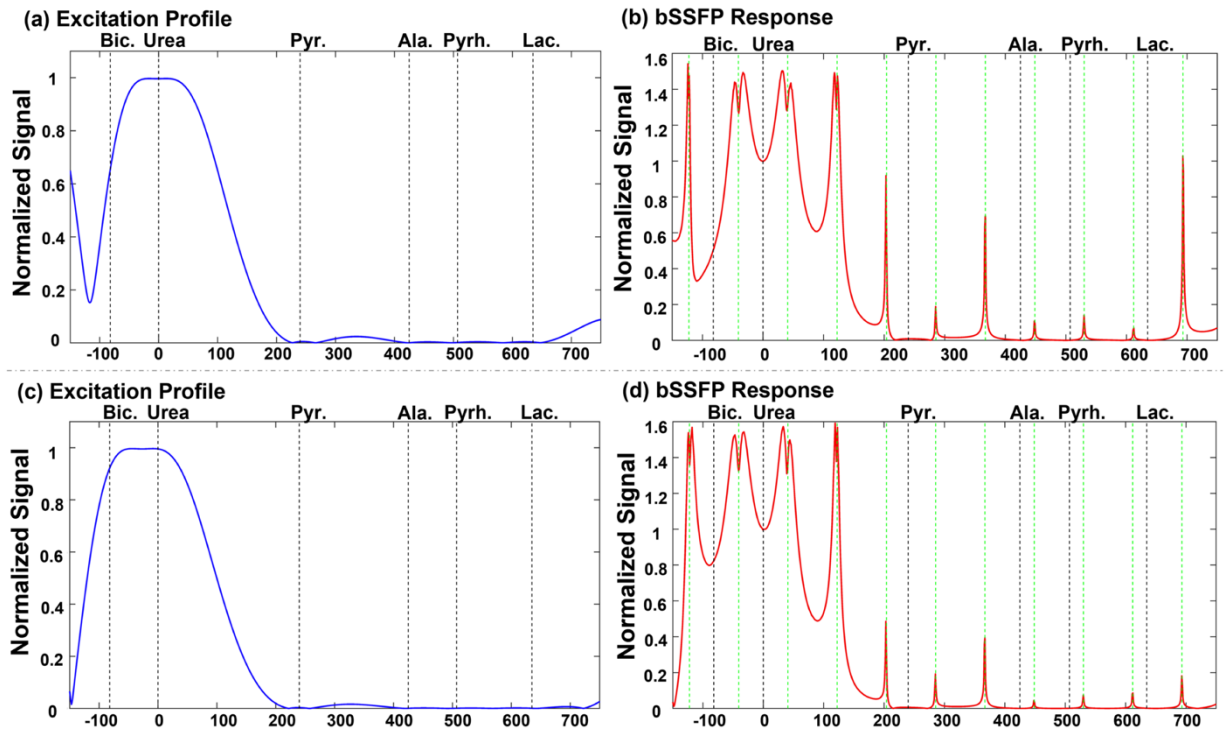

Figure 5.S2 (a) The excitation profiles of newly designed multiband urea-selective RF pulse. (c) The excitation profiles of the initial multiband urea-selective RF pulse design15. (b&d) The corresponding simulated bSSFP response using the averaged magnetization of 64 pulses. The vertical green dot lines show the frequency locations of banding artifacts. The bSSFP response has signal improvements on these frequency locations comparing with the excitation profile of GRE sequence.

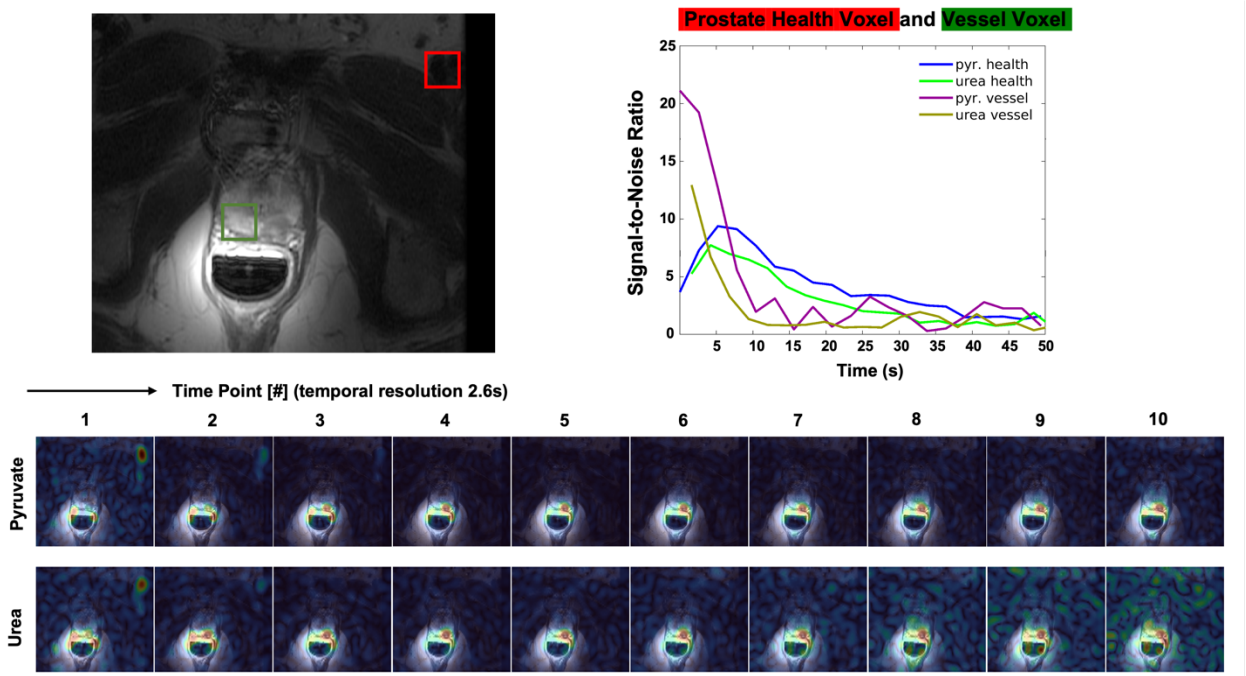

Figure 5.S3: Dynamic images with extracted dynamic curves of pyruvate and urea signals measured on ROIs in a healthy-appearing prostate region and the left superficial femoral vein region. All signals have been normalized by the corresponding noise signals. Each dynamic figure is displayed with the independent color scale. Even with the endo-rectal receive coil, we observed vessel signals during the early time-points, where the acquisition started 8s after completion of the injection.

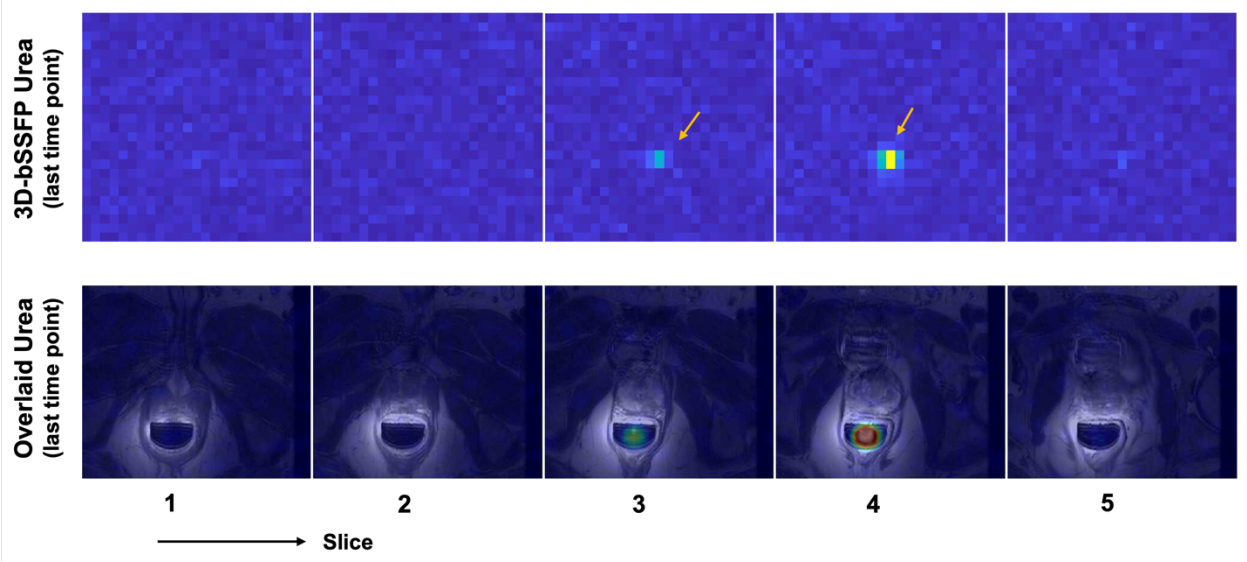

Figure 5.S4: Urea phantom image acquired by 3D-bSSFP sequence.

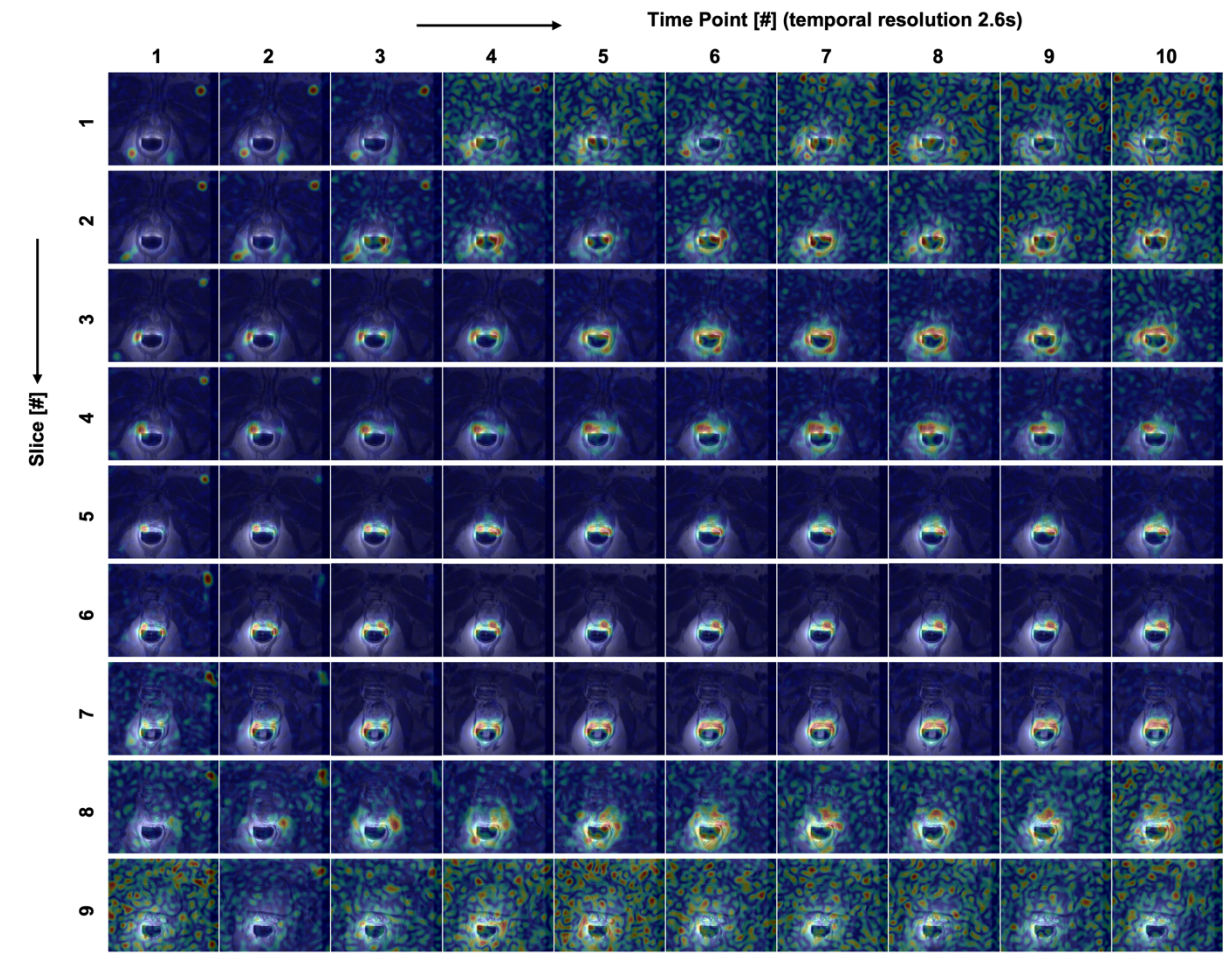

Figure 5.S5: Dynamic [1-^{13}C]pyruvate prostate images with 9 slices acquired by 2D-GRE sequence. All dynamic figures are displayed with the independent color scale.

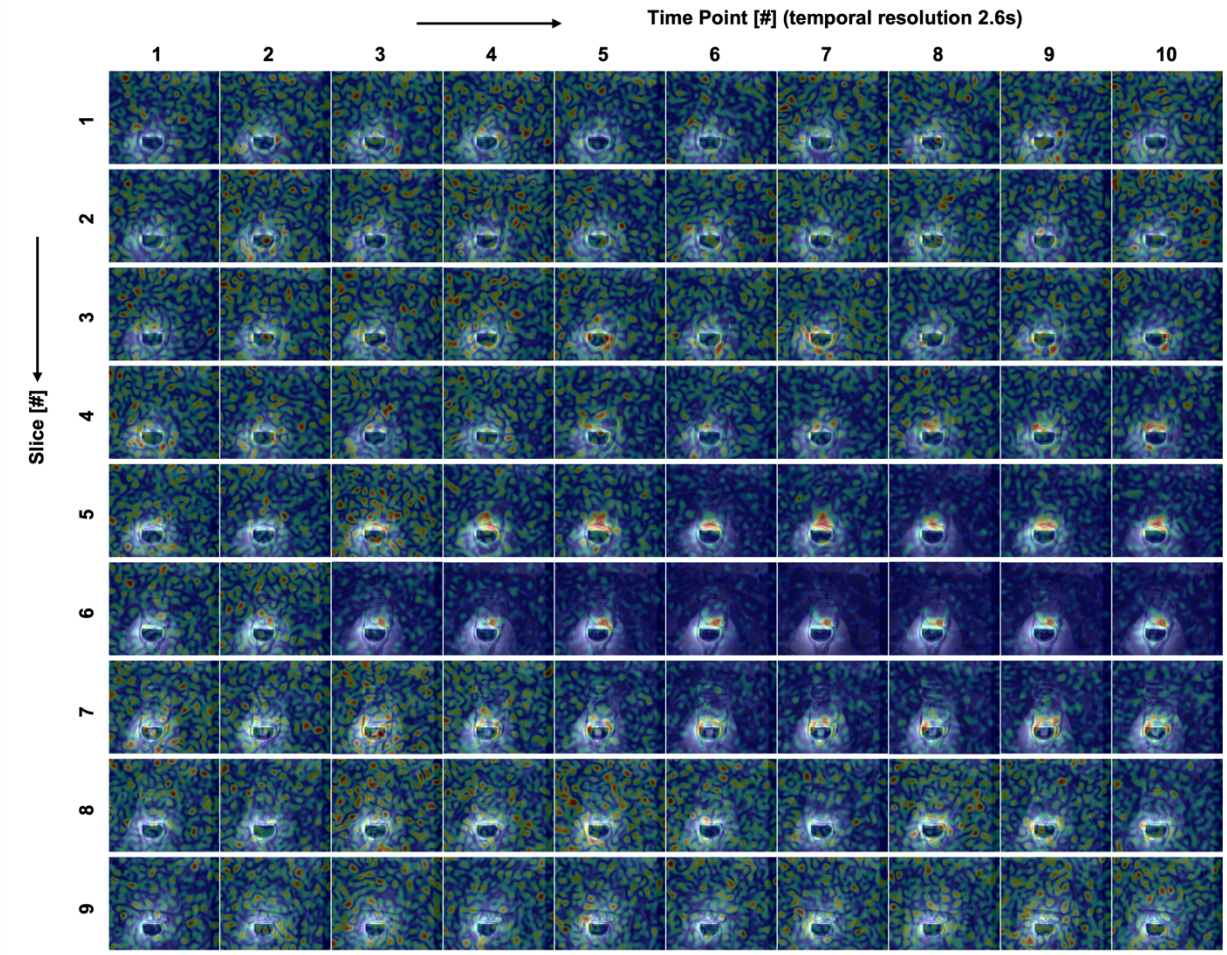

Figure 5.S6: Dynamic [1-^{13}C]lactate prostate images with 9 slices acquired by 2D-GRE sequence. All dynamic figures are displayed with the independent color scale.

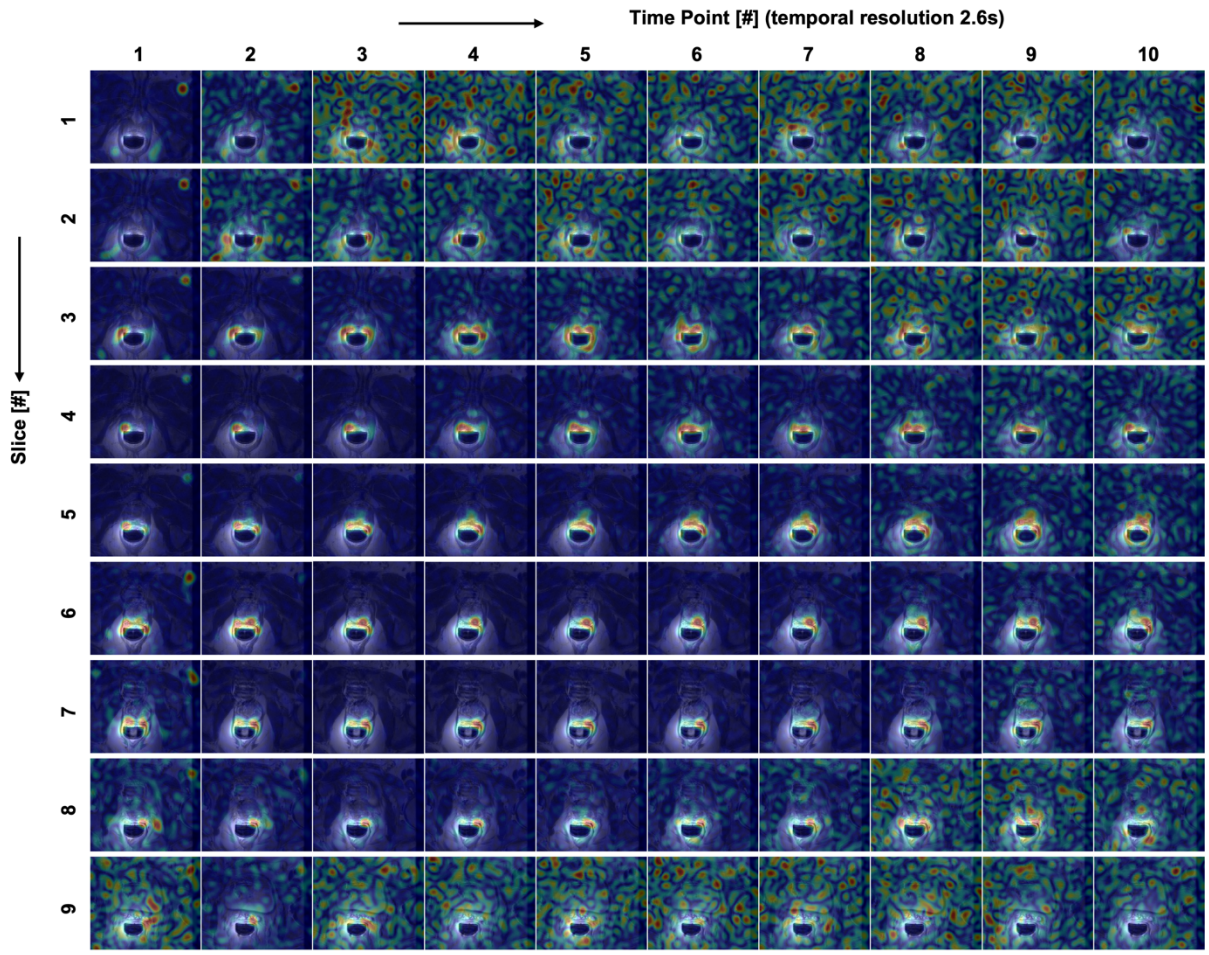

Figure 5.S7: Dynamic [^{13}C, $^{15}N_2$]urea prostate images with 9 slices acquired by 3D-bSSFP sequence. All dynamic figures are displayed with the independent color scale.

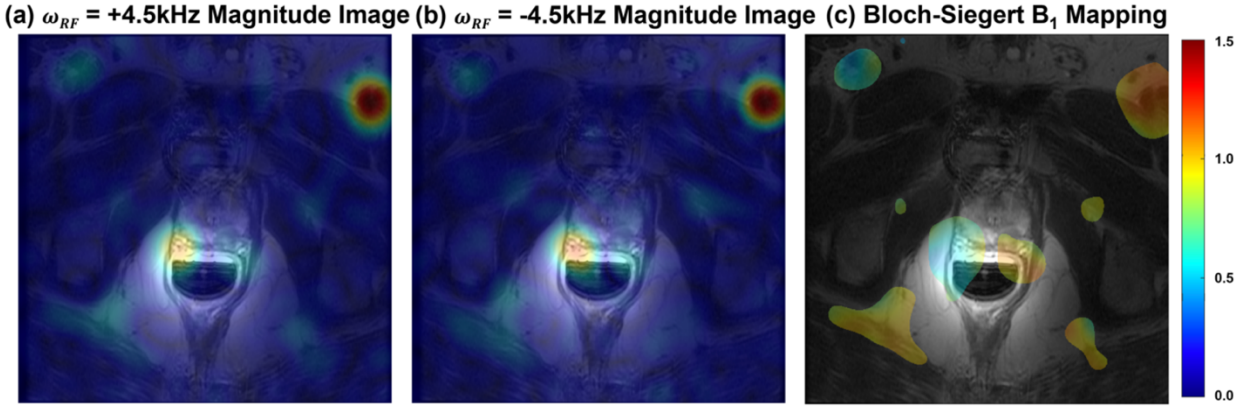

Figure 5.S8: B_1 Mapping by Bloch-Siegert method. (a&b) The magnitude image acquired with 12ms off-resonance Fermi pulse, ωRF = 4.5kHz. (c) Bloch-Siegert B1 map, a mask generated by the magnitude images (a) with SNR threshold higher than 3.

5.7 References

1. Hanahan D, Weinberg RA. Hallmarks of cancer: the next generation. *Cell*. 2011; **144**: 646-674.
2. Hanahan D, Weinberg RA. The Hallmarks of Cancer. Cell. 2000;100: 57-70.
3. Welch DR, Hurst DR. Defining the hallmarks of metastasis. *Cancer Res*. 2019; **79**: 3011-3027
4. von Morze C, Larson PEZ, Hu S, et al. Investigating tumor perfusion and metabolism using multiple hyperpolarized 13C compounds: HP001, pyruvate and urea. *Magn Reson Imaging*. 2012; **30**: 305-311.
5. Wilson DM, Keshari KR, Larson PEZ, et al. Multi-compound polarization by DNP allows simultaneous assessment of multiple enzymatic activities in vivo. *J Magn Reson*. 2010; **205**: 141-147.
6. Bok, R., Lee, J., Sriram, R., Keshari, K., Sukumar, S., Daneshmandi, S., Korenchan, D. E., Flavell, R. R., Vigneron, D. B., Kurhanewicz, J., & Seth, P. (2019). The role of lactate metabolism in prostate cancer progression and metastases revealed by dual-agent hyperpolarized 13 C MRSI. *Cancers*, *11*(2). https://doi.org/10.3390/cancers11020257
7. Mu, C., Korenchan, D. E., Wang, S., Wilson, D. M., & Flavell, R. R. (2021). Tumor Microenvironment Biosensors for Hyperpolarized Carbon-13 Magnetic Resonance Spectroscopy. In *Molecular Imaging and Biology* (Vol. 23, Issue 3, pp. 323–334). Springer Science and Business Media Deutschland GmbH. https://doi.org/10.1007/s11307-020-01570-0
8. Kurhanewicz, J., Vigneron, D. B., Ardenkjaer-Larsen, J. H., Bankson, J. A., Brindle, K., Cunningham, C. H., Gallagher, F. A., Keshari, K. R., Kjaer, A., Laustsen, C., Mankoff, D. A., Merritt, M. E., Nelson, S. J., Pauly, J. M., Lee, P., Ronen, S., Tyler, D. J., Rajan, S. S., Spielman, D. M., … Rizi, R. (2019). Hyperpolarized 13C MRI: Path to Clinical Translation in Oncology. In *Neoplasia (United States)* (Vol. 21, Issue 1, pp. 1–16). Neoplasia Press, Inc. https://doi.org/10.1016/j.neo.2018.09.006

9. Wang, Z. J., Ohliger, M. A., Larson, P. E. Z., Gordon, J. W., Bok, R. A., Slater, J., Villanueva-Meyer, J. E., Hess, C. P., Kurhanewicz, J., & Vigneron, D. B. (2019). Hyperpolarized 13C MRI: State of the art and future directions. In *Radiology* (Vol. 291, Issue 2, pp. 273–284). Radiological Society of North America Inc. https://doi.org/10.1148/radiol.2019182391
10. Kabir Anaraki, A., Ayati, M., & Kazemi, F. (2019). Magnetic resonance imaging-based brain tumor grades classification and grading via convolutional neural networks and genetic algorithms. *Biocybernetics and Biomedical Engineering*, *39*(1), 63–74. https://doi.org/10.1016/j.bbe.2018.10.004
11. van Elmpt, W., Zegers, C. M. L., Reymen, B., Even, A. J. G., Dingemans, A. M. C., Oellers, M., Wildberger, J. E., Mottaghy, F. M., Das, M., Troost, E. G. C., & Lambin, P. (2016). Multiparametric imaging of patient and tumour heterogeneity in non-small-cell lung cancer: quantification of tumour hypoxia, metabolism and perfusion. *European Journal of Nuclear Medicine and Molecular Imaging*, *43*(2), 240–248. https://doi.org/10.1007/s00259-015-3169-4
12. Chen HY, Larson PEZ, Bok RA, von Morze C, Sriram R, Santos RD, Santos JD, Gordon JW, Bahrami N, Ferrone M, Kurhanewicz J, Vigneron DB. Assessing prostate cancer aggressiveness with hyperpolarized dual-agent 3D dynamic imaging of metabolism and perfusion. *Cancer Res.* 2017; **77**: 3207-3216.
13. Reed, G. D., von Morze, C., Bok, R., Koelsch, B. L., van Criekinge, M., Smith, K. J., Shang, H., Larson, P. E. Z., Kurhanewicz, J., & Vigneron, D. B. (2014). High resolution 13C MRI with hyperpolarized urea: In vivo T 2 mapping and 15N labeling effects. *IEEE Transactions on Medical Imaging*, *33*(2), 362–371. https://doi.org/10.1109/TMI.2013.2285120
14. Nielsen, P. M., Szocska Hansen, E. S., Nørlinger, T. S., Nørregaard, R., Bonde Bertelsen, L., Stødkilde Jørgensen, H., & Laustsen, C. (2016). Renal ischemia and reperfusion assessment with three-dimensional hyperpolarized 13C,15N2-urea. *Magnetic Resonance in Medicine*, *76*(5), 1524–1530. https://doi.org/10.1002/mrm.26377

15. Qin, H., Tang, S., Riselli, A. M., Bok, R. A., Delos Santos, R., van Criekinge, M., Gordon, J. W., Aggarwal, R., Chen, R., Goddard, G., Zhang, C. T., Chen, A., Reed, G., Ruscitto, D. M., Slater, J., Sriram, R., Larson, P. E. Z., Vigneron, D. B., & Kurhanewicz, J. (2022). Clinical translation of hyperpolarized 13C pyruvate and urea MRI for simultaneous metabolic and perfusion imaging. *Magnetic Resonance in Medicine*, *87*(1), 138–149. https://doi.org/10.1002/mrm.28965
16. Milshteyn, E., von Morze, C., Gordon, J. W., Zhu, Z., Larson, P. E. Z., & Vigneron, D. B. (2018). High spatiotemporal resolution bSSFP imaging of hyperpolarized [1-13C]pyruvate and [1-13C]lactate with spectral suppression of alanine and pyruvate-hydrate. *Magnetic Resonance in Medicine*, *80*(3), 1048–1060. https://doi.org/10.1002/mrm.27104
17. Leupold, J., Månsson, S., Stefan Petersson, J., Hennig, J., & Wieben, O. (2009). Fast multiecho balanced SSFP metabolite mapping of 1H and hyperpolarized 13C compounds. *Magnetic Resonance Materials in Physics, Biology and Medicine*, *22*(4), 251–256. https://doi.org/10.1007/s10334-009-0169-z
18. Tang, S., Bok, R., Qin, H., Reed, G., VanCriekinge, M., Delos Santos, R., Overall, W., Santos, J., Gordon, J., Wang, Z. J., Vigneron, D. B., & Larson, P. E. Z. (2020). A metabolite-specific 3D stack-of-spiral bSSFP sequence for improved lactate imaging in hyperpolarized [1-13C]pyruvate studies on a 3T clinical scanner. *Magnetic Resonance in Medicine*, *84*(3), 1113–1125. https://doi.org/10.1002/mrm.28204
19. Cunningham, C. H., Chen, A. P., Lustig, M., Hargreaves, B. A., Lupo, J., Xu, D., Kurhanewicz, J., Hurd, R. E., Pauly, J. M., Nelson, S. J., & Vigneron, D. B. (2008). Pulse sequence for dynamic volumetric imaging of hyperpolarized metabolic products. *Journal of Magnetic Resonance*, *193*(1), 139–146. https://doi.org/10.1016/j.jmr.2008.03.012

20. Gordon, J. W., Vigneron, D. B., & Larson, P. E. Z. (2017). Development of a symmetric echo planar imaging framework for clinical translation of rapid dynamic hyperpolarized 13C imaging. *Magnetic Resonance in Medicine*, *77*(2), 826–832. https://doi.org/10.1002/mrm.26123

21. Tang, S., Meng, M. v., Slater, J. B., Gordon, J. W., Vigneron, D. B., Stohr, B. A., Larson, P. E. Z., & Wang, Z. J. (2021). Metabolic imaging with hyperpolarized 13C pyruvate magnetic resonance imaging in patients with renal tumors—Initial experience. *Cancer*, *127*(15), 2693–2704. https://doi.org/10.1002/cncr.33554

22. Shang, H., Larson, P. E. Z., Kerr, A., Reed, G., Sukumar, S., Elkhaled, A., Gordon, J. W., Ohliger, M. A., Pauly, J. M., Lustig, M., & Vigneron, D. B. (2016). Multiband RF pulses with improved performance via convex optimization. *Journal of Magnetic Resonance*, *262*, 81–90. https://doi.org/10.1016/j.jmr.2015.11.010

23. Scheffler, K., & Lehnhardt, S. (2003). Principles and applications of balanced SSFP techniques. *European Radiology*, *13*(11), 2409–2418. https://doi.org/10.1007/s00330-003-1957-x

24. Svensson J, Månsson S, Johansson E, Petersson JS, Olsson LE. Hyperpolarized 13C MR angiography using trueFISP. *Magn Reson Med*. 2003; **50**: 256-262.

25. Hyperpolarized-MRI-Toolbox. **https://github.com/LarsonLab/hyperpolarized-mri-toolbox**.

26. Tang, S., Jiang, W., Chen, H. Y., Bok, R., Vigneron, D. B., & Larson, P. E. Z. (2015). A 2DRF pulse sequence for bolus tracking in hyperpolarized 13C imaging. *Magnetic Resonance in Medicine*, *74*(2), 506–512. https://doi.org/10.1002/mrm.25427

27. Tang, S., Milshteyn, E., Reed, G., Gordon, J., Bok, R., Zhu, X., Zhu, Z., Vigneron, D. B., & Larson, P. E. Z. (2019). A regional bolus tracking and real-time B1 calibration method for hyperpolarized 13C MRI. *Magnetic Resonance in Medicine*, *81*(2), 839–851. https://doi.org/10.1002/mrm.27391

28. Jackson, J. I., Meyer, C. H., Nishimura, D. G., & Macovski, A. (1991). Selection of a Convolution Function for Fourier Inversion Using Gridding. *IEEE Transactions on Medical Imaging*, *10*(3), 473–478. https://doi.org/10.1109/42.97598

29. Reed, G. D., von Morze, C., Verkman, A. S., Koelsch, B. L., Chaumeil, M. M., Lustig, M., Ronen, S. M., Bok, R. A., Sands, J. M., Larson, P. E. Z., Wang, Z. J., Larsen, J. H. A., Kurhanewicz, J., & Vigneron, D. B. (2016). Imaging Renal Urea Handling in Rats at Millimeter Resolution Using Hyperpolarized Magnetic Resonance Relaxometry. *Tomography*, *2*(2), 125–137. https://doi.org/10.18383/j.tom.2016.00127

30. Furuyamaa, J. K., Nagarajan, R., Roberts, C. K., Lee, C. C., Hahn, T. J., & Thomas, M. A. (2014). A pilot validation of multi-echo based echo-planar correlated spectroscopic imaging in human calf muscles. *NMR in Biomedicine*, *27*(10), 1176–1183. https://doi.org/10.1002/nbm.3171

31. Bertelsen LB, Nielsen PM, Qi H, Norlinger TS, Zhang X, Stødkilde-Jørgensen H, Laustsen C. Diabetes induced renal urea transport alterations assessed with 3D hyperpolarized 13C,15N-urea. *Magn Reson Med*. 2017; **77**: 1650-1655. **https://doi.org/10.1002/mrm.26256**

32. Nelson, S. J., Kurhanewicz, J., Vigneron, D. B., Larson, P. E. Z., Harzstark, A. L., Ferrone, M., van Criekinge, M., Chang, J. W., Bok, R., Park, I., Reed, G., Carvajal, L., Small, E. J., Munster, P., Weinberg, V. K., Ardenkjaer-Larsen, J. H., Chen, A. P., Hurd, R. E., Odegardstuen, L. I., … Murray, J. A. (2013). Metabolic imaging of patients with prostate cancer using hyperpolarized [1-13C]pyruvate. In *Science Translational Medicine* (Vol. 5, Issue 198). https://doi.org/10.1126/scitranslmed.3006070

33. Crane, J. C., Gordon, J. W., Chen, H. Y., Autry, A. W., Li, Y., Olson, M. P., Kurhanewicz, J., Vigneron, D. B., Larson, P. E. Z., & Xu, D. (2021). Hyperpolarized 13C MRI data acquisition and analysis in prostate and brain at University of California, San Francisco. In *NMR in Biomedicine* (Vol. 34, Issue 5). John Wiley and Sons Ltd. https://doi.org/10.1002/nbm.4280

34. Larson, P. E. Z., Chen, H. Y., Gordon, J. W., Korn, N., Maidens, J., Arcak, M., Tang, S., Criekinge, M., Carvajal, L., Mammoli, D., Bok, R., Aggarwal, R., Ferrone, M., Slater, J. B., Nelson, S. J., Kurhanewicz, J., & Vigneron, D. B. (2018). Investigation of analysis methods for hyperpolarized 13C-pyruvate metabolic MRI in prostate cancer patients. *NMR in Biomedicine*, *31*(11). https://doi.org/10.1002/nbm.3997

35. Bankson JA, Walker CM, Ramirez MS, Stefan W, Fuentes D, Merritt ME, Lee J, Sandulache VC, Chen Y, Phan L, Chou P, Rao A, Yeung SJ, Lee M, Schellingerhout D, Conrad CA, Malloy C, Sherry AD, Lai SY, Hazle JD. Kinetic modeling and constrained reconstruction of hyperpolarized [1-^{13}C]-pyruvate offers improved metabolic imaging of tumors. *Cancer Res*. 2015; **75**: 4708-4717. https://doi.org/10.1158/0008-5472.CAN-15-0171

36. Assländer J, Glaser SJ, Hennig J. Pseudo steady-state free precession for MR-fingerprinting. *Magn Reson Med*. 2017; **77**: 1151-1161. https://doi.org/10.1002/mrm.26202

37. Wang, C. Y., Coppo, S., Mehta, B. B., Seiberlich, N., Yu, X., & Griswold, M. A. (2019). Magnetic resonance fingerprinting with quadratic RF phase for measurement of T2* simultaneously with δf, T1, and T2. *Magnetic Resonance in Medicine*, *81*(3), 1849–1862. https://doi.org/10.1002/mrm.27543

38. Jiang, Y., Ma, D., Seiberlich, N., Gulani, V., & Griswold, M. A. (2015). MR fingerprinting using fast imaging with steady state precession (FISP) with spiral readout. *Magnetic Resonance in Medicine*, *74*(6), 1621–1631. https://doi.org/10.1002/mrm.25559

39. Lau, A. Z., Miller, J. J., Robson, M. D., & Tyler, D. J. (2017). Simultaneous assessment of cardiac metabolism and perfusion using copolarized [1-13C]pyruvate and 13C-urea. *Magnetic Resonance in Medicine*, *77*(1), 151–158. https://doi.org/10.1002/mrm.26106

Chapter 6: Dual Hyperpolarized [1-^{13}C]Pyruvate and [^{13}C]Urea Magnetic Resonance Imaging of Prostate Cancer

GRAPHICAL ABSTRACT

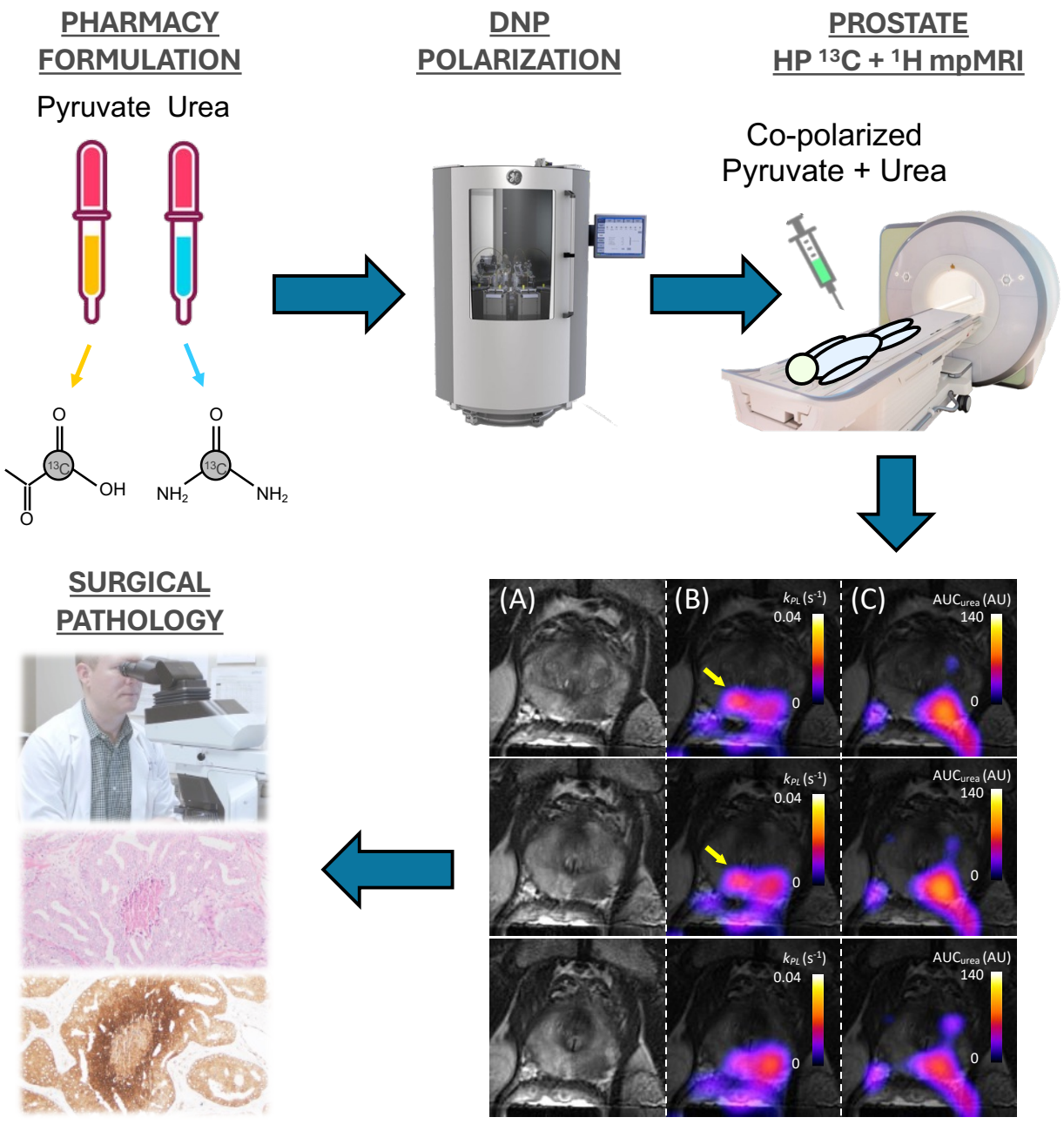

6.1 ABSTRACT

6.1.1 Background

Although multiparametric (mp) ^{1}H magnetic resonance imaging (MRI) is increasingly used to detect and localize prostate cancer (PC), its correlation with tumor grade is limited. Hyperpolarized (HP) carbon-13 (^{13}C) MR is an emerging imaging technique, which can be used to interrogate key biologic processes through in vivo detection of various HP probes. A distinct attribute of HP ^{13}C MRI is the ability to detect multiple HP probes within a single acquisition. Here we report on the first simultaneous dual HP [1-^{13}C]pyruvate and [^{13}C]urea MRI with correlations to histopathologic findings in a patient with localized PC scheduled for radical prostatectomy.

6.1.2 Material and Methods

Paired HP ^{13}C and standard mp ^{1}H MRI were performed in a patient with biopsy-proven Gleason score 4 + 3 = 7 adenocarcinoma of the prostate scheduled for radical prostatectomy through a first-in-human pilot study of dual-agent HP MRI (NCT02526368). HP ^{13}C MRI was performed using a clinical 3T scanner with ^{13}C transmit-and-receive capabilities. Dynamic series of HP ^{13}C pyruvate, lactate and urea imaging were acquired following intravenous (IV) injection of co-hyperpolarized [^{13}C]urea (25 mM) and [1–^{13}C]pyruvate (125 mM). The [1-^{13}C]pyruvate-to-[1-^{13}C]lactate conversion rate (k_{PL}) was calculated using an inputless two-site exchange model; AUC_{urea} was the [^{13}C]urea signal summed over time. Following radical prostatectomy, whole-mount prostate histopathological slides were prepared and reviewed by an experienced genitourinary pathologist.

6.1.3 Results

Following informed consent, the patient underwent paired mp ^{1}H MRI and dual-agent HP MRI. mp ^{1}H MRI revealed a 1.2 cm lesion in the left apical posterior zone. Dual-agent HP MRI

identified a focus of increased [1-^{13}C]pyruvate-to-[1-^{13}C]lactate conversion rate (k_{PL}) extending from the left apical posterior peripheral zone to the right gland. A corresponding area of abnormal tissue perfusion (AUC_{urea}) was seen in the left gland. Metabolism-perfusion mismatch (with several foci of increased k_{PL}/AUC_{urea}) was observed throughout the tumor. Tumor extension to the right midgland was confirmed at the time of radical prostatectomy and staining for lactate dehydrogenase-A was increased throughout the tumor relative to surrounding benign prostatic tissue.

6.1.4 Conclusion

This first-in-human radiopathologic study demonstrates the feasibility of dual-agent HP MRI in PC patients. Simultaneous assessment of tumor metabolism and perfusion was able to detect occult disease as well as to show a significant mismatch between intra-tumoral metabolism and tissue perfusion in high-grade PC. Prospective validation of these findings is warranted.

6.1.5 Highlights

- Dual-agent hyperpolarized ^{13}C MRI was used to simultaneously assess tumor metabolism and tissue perfusion in a patient with localized prostate cancer;
- Hyperpolarized [1-^{13}C]pyruvate MRI was able to detect areas of clinically occult prostate cancer not seen on multiparametric MRI;
- The addition of hyperpolarized [^{13}C]urea suggested a significant mismatch between intra-tumoral metabolism and tissue perfusion.

6.2 Introduction

Multiparametric (mp) ^{1}H magnetic resonance imaging (MRI) is increasingly used to detect prostate cancer (PC) and guide diagnostic and treatment decisions. While it provides a whole gland assessment with high patient-level sensitivity, clinically significant PC can still be found up to 20 % of patients with a negative mpMRI[1]. Currently, MRI evaluation of suspected PC in the treatment-naïve prostate gland is performed according to the Prostate Imaging Reporting & Data System (PI-RADS v2.1)[2] scoring system. This is a qualitative score, which is associated with significant inter-reader variability[3] and generally poor correlations with tumor grade[4]. These limitations, together with the increased use of focal therapies for intermediate risk disease, highlight the need for improved and quantitative biomarkers of aggressive PC.

Hyperpolarized (HP) carbon-13 (^{13}C) MRI is an emerging imaging technique that enables in vivo detection of a range of HP probes with high spatiotemporal resolution[5]. The most widely studied of these, HP [1-^{13}C]pyruvate, is a key substrate of anaerobic glycolysis upregulated in cancer. Measurement of [1-^{13}C]pyruvate-to-[1-^{13}C]lactate conversion rate (k_{PL}) provides a non-invasive, quantitative assessment of lactate dehydrogenase activity and tumor metabolic reprogramming. Increased k_{PL} can distinguish PC from benign surrounding prostate tissue and has been shown to correlate with histologic grade[6]. In addition to [1-^{13}C]pyruvate, the metabolically inert probe [^{13}C]urea has successfully been used to assess tumor hypoxia[7]—another key hallmark of aggressive PC[8,9]. In pre-clinical models of PC, decreased tumor perfusion (represented by a lower urea signal summed over time, AUC_{urea}) has been correlated with histologic grade and markers of hypoxia[10].

A distinct attribute of HP ^{13}C MRI over other functional imaging modalities is the ability to detect multiple HP probes within a single acquisition by taking advantage of their chemical shift

differences. Dual-agent [1-^{13}C]pyruvate and [^{13}C]urea HP MRI thus enables simultaneous quantification of tumor metabolism (via measurement of the [1-^{13}C]pyruvate-to-[1-^{13}C]lactate conversion rate, k_{PL}) and perfusion (via measurement of the AUC_{urea} of metabolically inert [^{13}C]urea, AUC_{urea}). Here we present the first dual HP [1-^{13}C]pyruvate and [^{13}C]urea MRI with pathologic correlation in a patient with localized PC.

6.3 Material and methods

6.3.1 Patient characteristics

The patient was 57 year-old man with clinically localized prostate cancer. Initial prostate-specific antigen level was 5.7 ng/dL. Staging ^{1}H mpMRI revealed a 1.2 cm lesion confined to the left apical posterior peripheral zone, without macroscopic extraprostatic extension or seminal vesicle invasion. MRI-ultrasound fusion biopsies confirmed the presence of prostatic adenocarcinoma in the left apical posterior peripheral zone (Gleason score 4 + 3 = 7). US-guided biopsies revealed additional foci of Gleason score 4 + 3 = 7 and 3 + 4 = 7 adenocarcinoma in the left mid region and left apex, respectively. Dual HP [1-^{13}C]pyruvate and [^{13}C]urea MRI was performed as part of an Institutional Review Board approved protocol (NCT02526368). Key eligibility criteria for this study included a diagnosis of biopsy-proven adenocarcinoma of the prostate and planned radical prostatectomy within 12 weeks of the on-study MRI. Participants were required to have an Eastern Cooperative Oncology Group (ECOG) performance status score of 0 to 1, and adequate organ functions (including an absolute neutrophil count ≥ 1500 cells/μL, hemoglobin ≥ 9.0 gm/dL, platelets ≥ 75,000 cells/μL, estimated creatinine clearance ≥ 50 mL/min by the Cockcroft Gault equation, as well as bilirubin, aspartate and alanine aminotransferase levels less than 1.5 times the institutional upper limit of normal). Eligible participants were required to be able to undergo MR imaging without any contra-

indication to MRI, injection of gadolinium contrast, or endorectal coil insertion. Prior local therapy to the prostate (including prior transurethral resection of prostate or cryosurgery) or androgen deprivation therapy (current or prior) were not allowed.

6.3.2 Pharmaceutical Preparation of [1-^{13}C]pyruvate and [^{13}C]urea Agents for Co-Hyperpolarization

The pharmaceutical manufacturing followed an FDA-approved research IND for co-hyperpolarization of Good Manufacturing Practice [1-^{13}C]pyruvate and [^{13}C]urea[11]. Briefly, 0.378 g of 9.6 M [^{13}C]urea (MilliporeSigma, OH) aqueous solution (mixture with 12.5 mM electron paramagnetic agent, or EPA) and 1.098 g of 14.4 M pyruvate (MilliporeSigma, mixture with 12.5 mM EPA) were added to the pharmacy kit's cryogenic vial sequentially. The drug mixture was polarized in a 5T GE SPINlab (GE Healthcare, Chicago IL) polarizer for 3 h. The dissolution yielded 125/25 mM pyruvate/urea solution with an averaged 36.5 % polarization, 0.8uM residual trityl radical, 7.7 pH, and temperature of 37.4 °C. The quality control (QC) parameters were measured using the SPINlab's QC unit during the pharmaceutical release, and solution-state HP ^{13}C agent concentrations were characterized post-release using a 500 MHz NMR spectrometer (Avance DRX500, Bruker, MA).

6.3.3 Dual-Agent HP ^{13}C and ^{1}H mpMRI

Imaging was conducted on a clinical 3T scanner (MR750, GE Healthcare). The ^{13}C portion utilized a custom-built clamshell ^{13}C transmitter and a dual-element ^{1}H–^{13}C endorectal receiver, whereas the ^{1}H standard-of-care (SOC) imaging used body coil transmit and a 4-channel array receiver. Calibration of ^{13}C RF transmit power used a built-in 1 cm spherical 8 M urea phantom located inside the endocoil, and the ^{13}C center frequency was referenced to the ^{1}H frequency with a fixed conversion

factor. Time-resolved pyruvate-lactate imaging used a 2D multislice single-shot spiral sequence, and urea used a 3D stack-of-spiral balanced-SSFP.[12] Key sequence parameters included spatial resolution = 7 × 7 × 11.6 mm (pyruvate) & 9 × 9 × 11.6 mm (urea), nominal FOV = 21 × 21 × 11.6 cm (pyruvate) & 27.9 × 27.9 × 18.6 cm (urea), TR = 80 ms (pyruvate) & 12.3 ms (urea), and temporal resolution = 2.5 s. Pharmaceutical release followed QC verification of Investigational New Drug (IND)-approved safety criteria. The co-hyperpolarized solution was delivered through an antecubital IV route with a dosage of 0.43 mL/kg, followed by saline flush, and the scan started 8 s post-injection. The ^{1}H SOC MRI included an axial oblique T_2-weighted sequence, diffusion-weighted sequence with b-values of 600 and 1350 s/mm^2, and dynamic contrast-enhanced imaging as previously published[13].

6.3.4 MRI Data Processing and Image Analysis

Reconstruction, processing and quantification of HP ^{13}C data was conducted on MATLAB (Mathworks, Natick MA) as previously described[14], which accounted for possible off-resonances during acquisition. Briefly, the acquired spiral MRI data was re-gridded and underwent inverse Fourier transform back to image space. ^{13}C-^{1}H image co-registration was confirmed using a color overlay of pyruvate over greyscale T2-weighted images. Bulk off-resonance shift was corrected slice-by-slice by demodulating the raw data to the off-resonance frequency found via an autofocus algorithm[15]. An open-source image processing software, SIVIC, developed by our team was used for visualization and examination of processed data. Pyruvate-to-lactate conversion rate (k_{PL}) was calculated using an input-less two-site exchange model[16,17]. AUC_{urea} was calculated as the urea signal summed over time; AUC_{urea} distribution was corrected for the coil sensitivity profile[18].

6.3.5 Histopathological and Immunochemical Tissue Analyses

Following radical prostatectomy, whole-mount prostate histopathological slides were stained with haematoxylin and eosin (H&E) and reviewed by an experienced genitourinary pathologist (B. A. S.). Foci of prostatic adenocarcinoma were outlined and assigned a Gleason score. Additional immunohistochemical (IHC) staining for lactate dehydrogenase A (LDH-A) was performed on formalin-fixed paraffin-embedded (FFPE) step-sections of the specimen. Four-micron thick sections were deparaffinated, rehydrated, antigen retrieved with citrate buffer and then exposed sequentially to anti-LDHA [(E-9) sc-137243 (Santa Cruz Biotechnology)] then HRP-conjugated secondary antibody for standard DAB staining. All slides were interpreted by our experienced genitourinary pathologist (B. A. S.).

6.4 Results

6.4.1 Dual-agent HP MRI

Following written informed consent, the patient underwent paired ^{1}H mpMRI and dual-agent HP MRI of the prostate. On-study imaging was performed 13 weeks after his initial prostate biopsy. mpMRI again showed a 1.3 cm x 0.7 cm x 0.9 cm left apical posterior peripheral zone with low T2 signal intensity, marked restricted diffusion and early enhancement (Prostate Imaging Reporting and Data System [PI-RADS] v2.1 score 4). No evidence of macroscopic extracapsular extension or seminal vesicle invasion was seen (Figure 6.1). Dual-agent HP MRI identified a focus of increased [1-^{13}C]pyruvate-to-[1-^{13}C]lactate metabolism (k_{PL}) extending from the left apical posterior peripheral zone to the right gland. A corresponding area of abnormal perfusion (AUC_{urea}) was seen in the left gland (Figure 6.2, panels B and C). Interestingly, evidence of metabolism-perfusion mismatch (with several foci of increased k_{PL}/AUC_{urea}) was observed throughout the tumor (Figure 6.2, panel D).

6.4.2 Dual-agent HP MRI

Following informed consent, the patient underwent paired ^{1}H mpMRI and dual-agent HP MRI of the prostate 13 weeks after his initial biopsy. mpMRI again showed a 1.3 cm x 0.7 cm x 0.9 cm left apical posterior peripheral zone with low T2 signal intensity, marked restricted diffusion and early enhancement (Prostate Imaging Reporting and Data System [PI-RADS] v2.1 score 4). No evidence of macroscopic extracapsular extension or seminal vesicle invasion was seen (Fig. 1). Dual-agent HP MRI identified a focus of increased [1-^{13}C]pyruvate-to-[1-^{13}C]lactate metabolism (k_{PL}) extending from the left apical posterior peripheral zone to the right gland. A corresponding area of abnormal perfusion (AUC_{urea}) was seen in the left gland (Fig. 2, panels B and C). Interestingly, evidence of metabolism-perfusion mismatch (with several foci of increased k_{PL}/AUC_{urea}) was observed throughout the tumor (Fig. 2, panel D).

6.4.3 Histopathologic correlation

One week following dual-agent HP MRI the patient underwent radical prostatectomy, which revealed a 2 cm^3 Gleason score 4 + 5 = 9 prostatic adenocarcinoma in the posterior apex. Tumor extension to the right midgland, as detected by HP ^{13}C MRI (but not ^{1}H mpMRI), was confirmed on pathology (Gleason pattern 4). Increased LDH-A staining by immunohistochemistry was observed throughout the tumor relative to surrounding benign prostatic tissue. Areas of comedonecrosis surrounded by intense LDH-A staining were noted in left posterior apex, corresponding to a focus of metabolism-perfusion mismatch (increased k_{PL}/AUC_{urea}) on HP MRI (Figure 6.2, panels D and E).

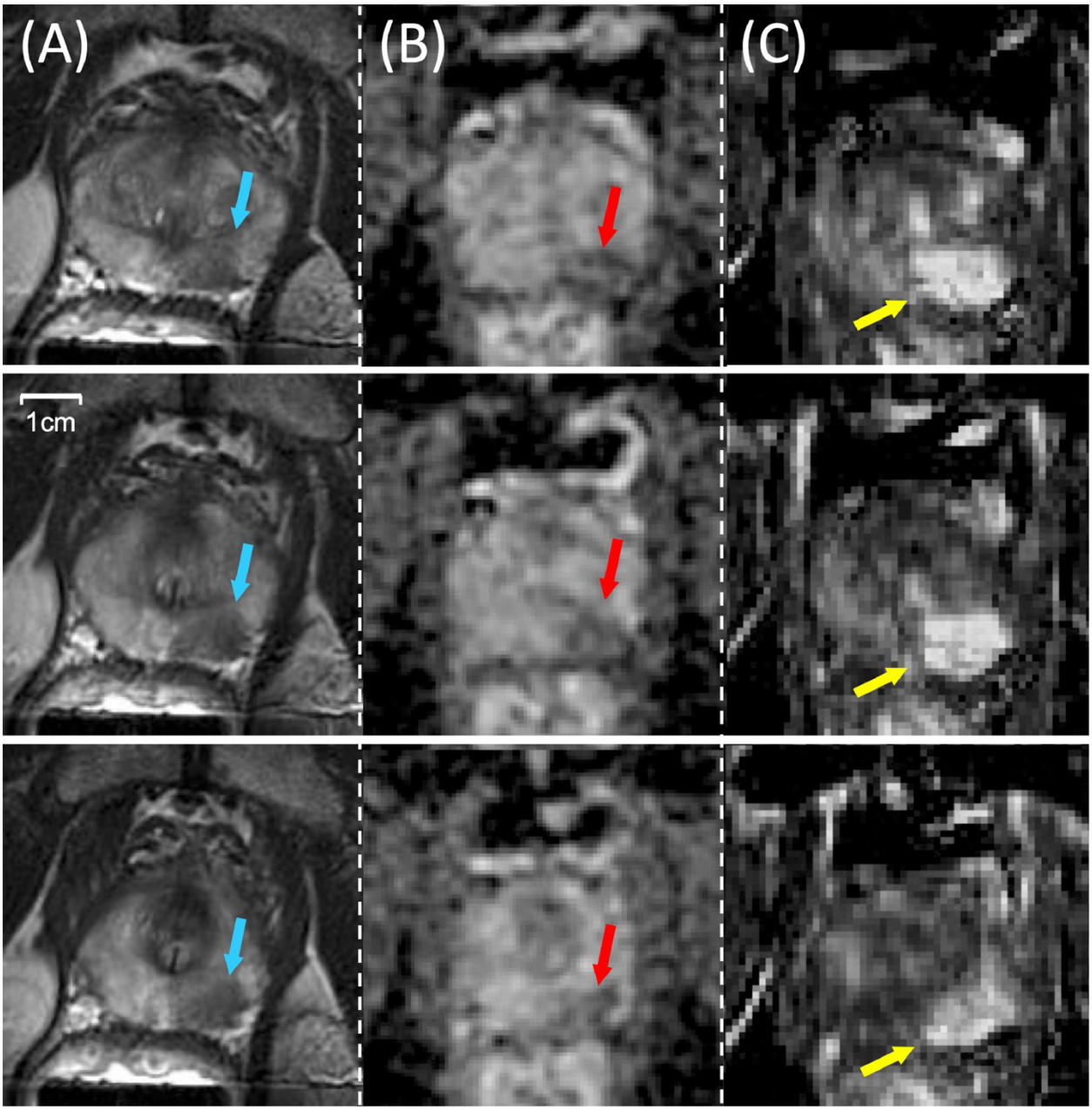

Figure 6.1: Representative axial T2-weighted (A), apparent diffusion coefficient (ADC, panel B) and dynamic contrast-enhanced (DCE, panel C) images, from the base (top row) to apex (bottom row) of the prostate. A well-defined focus of low T2-signal intensity is seen in the left apical posterior peripheral zone and demonstrates marked restricted diffusion on ADC maps (red arrow). The lesion is associated with early enhancement (blue arrow) on DCE images. Tumor extension across the midline is not seen.

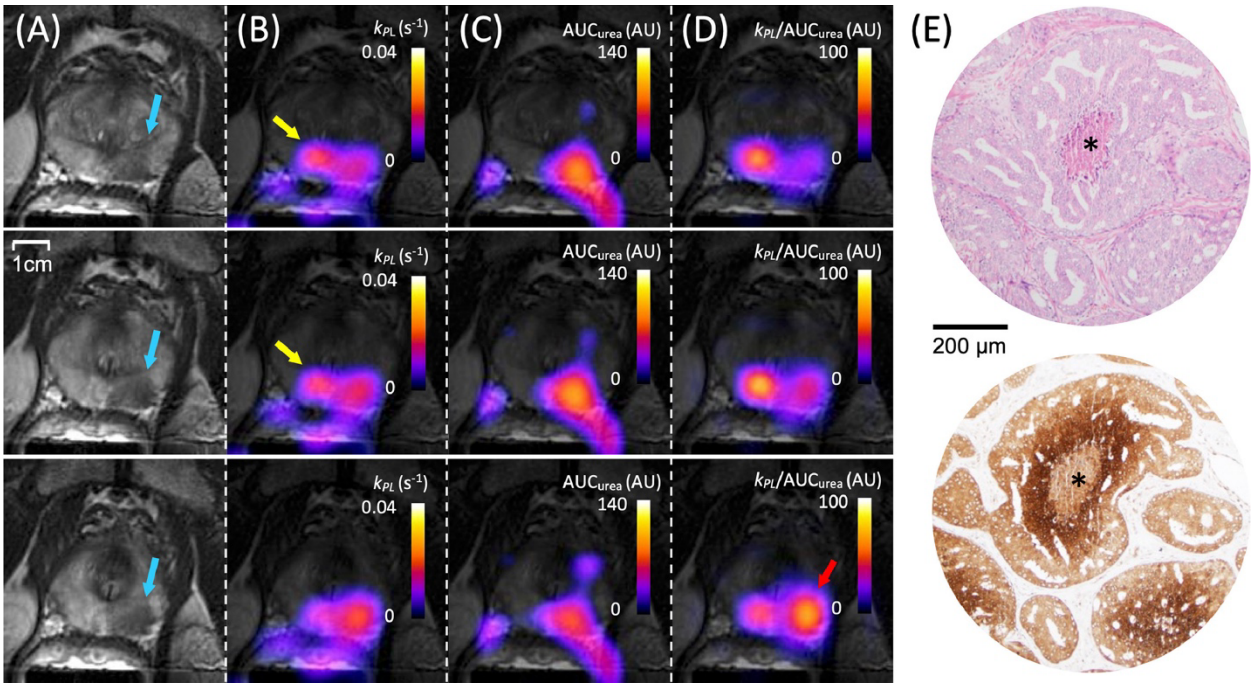

Figure 6.2: Representative axial T2-weighted (T2W) images (A), and T2W images with overlaid k_{PL} (B), AUC_{urea} (C) and k_{PL}/AUC_{urea} (D) maps, from the base (top row) to apex (bottom row) of the prostate. k_{PL} maps demonstrate tumor extension across the midline (yellow arrow) not seen on mpMRI. k_{PL}/AUC_{urea} maps show heterogeneous intratumoral metabolism-perfusion mismatch, including a focus of high metabolism/low perfusion in the left posterior apex (red arrow). Representative H&E and LDH-A stains of this area (E, top and bottom row, respectively) highlight intense LDH-A staining surrounding areas of comedonecrosis (asterisk). k_{PL}, [1-^{13}C]pyruvate-to-[1-^{13}C]lactate conversion rate; AUC_{urea}, [^{13}C]urea perfusion; AU, arbitrary units.

6.5 Discussion

This first-in-human radiopathologic study highlights the feasibility of dual-agent HP MRI in prostate cancer (PC) patients, and the potential for simultaneous assessment of tumor metabolism and perfusion to detect aggressive PC.

Similar to prior reports[6,19,20,21], we observed increased k_{PL} throughout the tumor relative to benign surrounding prostate tissue[6,19]. Increased intra-tumoral [1-^{13}C]lactate signal in PC is thought to be mediated by the influx of lactate into tumor epithelial cells as well as increased pyruvate-to-lactate

conversion via the lactate dehydrogenase enzymes[10,19,22]. Consistent with this, we observed increased LDH-A staining by IHC throughout the tumor relative to benign surrounding tissue. Furthermore, in this patient, extension of clinically significant (Gleason pattern 4) prostate cancer into the contralateral gland—not seen on pre- and post-biopsy mpMRI—was visualized on k_{PL} maps and confirmed at the time of RP. This finding adds to a growing body of literature showing the ability of HP ^{13}C MRI to detect clinically occult areas of PC[19,21,22], highlighting the potential for HP ^{13}C to improve risk stratification and patient selection for focal therapies.

Unlike HP [1-^{13}C]pyruvate, [^{13}C]urea is a metabolically inert probe, which can be used to measure tissue perfusion. Pre-clinical models have shown a direct correlation between decreased area under the curve of the [^{13}C]urea signal (AUC_{urea}) and markers of hypoxia[10]. Along with increased glycolytic activity, increased hypoxia is a hallmark of aggressive PC associated with therapeutic resistance[8,9]. Furthermore, tumor hypoxia has been shown to directly promote glucose uptake and glycolysis through HIF-1 alpha signaling[23]. Using the TRAMP model we have previously shown that high-grade PC is associated with significant metabolism-perfusion mismatch, characterized by increased tumor metabolism relative to perfusion. This can be directly visualized on dual HP [1-^{13}C]pyruvate and [^{13}C]urea MRI as areas of increased k_{PL}/AUC_{urea} within aggressive tumors[10]. In this patient, dual HP MRI revealed heterogeneous metabolism-perfusion mismatching throughout the tumor, including several areas of markedly increased k_{PL}/AUC_{urea}. Notably, we observed a distinct focus of elevated k_{PL}/AUC_{urea} in the left posterior apex, which was characterized by areas of comedonecrosis surrounded by intense LDH-A staining on microscopic examination (Figure 6.2, panel E), suggestive of metabolically active PC cells within a hypoxic tumor microenvironment.

6.6 Conclusions

This first-in-human radiopathologic study demonstrates the feasibility of dual-agent HP MRI in PC patients and its potential to detect aggressive disease. Simultaneous assessment of tumor metabolism and perfusion revealed occult disease not seen on mp ^{1}H MRI, while also showing significant heterogeneous mismatch between tumor metabolism and tissue perfusion in high-grade PC.

6.7 References

1. Drost, F.-J.H., Osses, D.F., Nieboer, D., Steyerberg, E.W., Bangma, C.H., Roobol, M.J., et al., 2019. Prostate MRI, with or without MRI-targeted biopsy, and systematic biopsy for detecting prostate cancer. The Cochrane Database of Systematic Reviews 4(4): CD012663, Doi: 10.1002/14651858.CD012663.pub2.
2. Turkbey, B., Rosenkrantz, A.B., Haider, M.A., Padhani, A.R., Villeirs, G., Macura, K.J., et al., 2019. Prostate Imaging Reporting and Data System Version 2.1: 2019 Update of Prostate Imaging Reporting and Data System Version 2. European Urology 76(3): 340–51, Doi: 10.1016/j.eururo.2019.02.033.
3. Westphalen, A.C., McCulloch, C.E., Anaokar, J.M., Arora, S., Barashi, N.S., Barentsz, J.O., et al., 2020. Variability of the Positive Predictive Value of PI-RADS for Prostate MRI across 26 Centers: Experience of the Society of Abdominal Radiology Prostate Cancer Disease-focused Panel. Radiology 296(1): 76–84, Doi: 10.1148/radiol.2020190646.
4. Boschheidgen, M., Schimmöller, L., Arsov, C., Ziayee, F., Morawitz, J., Valentin, B., et al., 2022. MRI grading for the prediction of prostate cancer aggressiveness. European Radiology 32(4): 2351–9, Doi: 10.1007/s00330-021-08332-8.
5. Kurhanewicz, J., Vigneron, D.B., Ardenkjaer-Larsen, J.H., Bankson, J.A., Brindle, K., Cunningham, C.H., et al., 2018. Hyperpolarized 13C MRI: Path to Clinical Translation in Oncology. Neoplasia (New York, N.Y.) 21(1): 1–16, Doi: 10.1016/j.neo.2018.09.006.
6. Korn N, Larson P.E.Z, Chen H.-Y, Gordon J.W, Bok R.A, Vancriekinge M, *et al.* The rate of hyperpolarized [1-13C] pyruvate to [1-13C] lactate conversion distinguishes high-grade prostate cancer from low-grade prostate cancer and normal peripheral zone tissue in patients ISMRM Annual Meeting, Paris, France (2018)

7. von Morze C, Larson P.E.Z, Hu S, Keshari K, Wilson D.M, Ardenkjaer-Larsen J.H, *et al.* Imaging of blood flow using hyperpolarized [13C]Urea in preclinical cancer models J. Magn. Reson. Imaging, 33 (3) (2011), pp. 692-697, 10.1002/jmri.22484
8. Fraga, A., Ribeiro, R., Príncipe, P., Lopes, C., Medeiros, R., 2015. Hypoxia and Prostate Cancer Aggressiveness: A Tale With Many Endings. Clinical Genitourinary Cancer 13(4): 295–301, Doi: 10.1016/j.clgc.2015.03.006.
9. Milosevic, M., Warde, P., Ménard, C., Chung, P., Toi, A., Ishkanian, A., et al., 2012. Tumor hypoxia predicts biochemical failure following radiotherapy for clinically localized prostate cancer. Clinical Cancer Research: An Official Journal of the American Association for Cancer Research 18(7): 2108–14, Doi: 10.1158/1078-0432.CCR-11-2711.
10. Chen, H.-Y., Larson, P.E.Z., Bok, R.A., von Morze, C., Sriram, R., Delos Santos, R., et al., 2017. Assessing Prostate Cancer Aggressiveness with Hyperpolarized Dual-Agent 3D Dynamic Imaging of Metabolism and Perfusion. Cancer Research 77(12): 3207–16, Doi: 10.1158/0008-5472.CAN-16-2083.
11. Qin, H., Tang, S., Riselli, A.M., Bok, R.A., Delos Santos, R., van Criekinge, M., et al., 2022. Clinical translation of hyperpolarized 13 C pyruvate and urea MRI for simultaneous metabolic and perfusion imaging. Magnetic Resonance in Medicine 87(1): 138–49, Doi: 10.1002/mrm.28965.
12. Tang, S., Bok, R., Qin, H., Reed, G., VanCriekinge, M., Santos, R.D., et al., 2020. A Metabolite Specific 3D Stack-of-Spiral bSSFP Sequence for Improved Lactate Imaging in Hyperpolarized [1-13C]Pyruvate Studies on a 3T Clinical Scanner. Magnetic Resonance in Medicine 84(3): 1113–25, Doi: 10.1002/mrm.28204.
13. Chen, H.-Y., Larson, P.E.Z., Gordon, J.W., Bok, R.A., Ferrone, M., van Criekinge, M., et al., 2018. Technique Development of 3D Dynamic CS-EPSI for Hyperpolarized 13C Pyruvate MR

Molecular Imaging of Human Prostate Cancer. Magnetic Resonance in Medicine 80(5): 2062–72, Doi: 10.1002/mrm.27179.

14. S. Tang, E. Milshteyn, G. Reed, J. Gordon, R. Bok, X. Zhu, *et al.* A regional bolus tracking and real-time B1 calibration method for hyperpolarized 13C MRI Magn. Reson. Med., 81 (2) (2019), pp. 839-851, 10.1002/mrm.27391
15. G.D. Reed, J. Ma, J.M. Park, R.F. Schulte, C.E. Harrison, A.P. Chen, *et al.* Characterization and compensation of inhomogeneity artifact in spiral hyperpolarized 13C imaging of the human heart Magn. Reson. Med., 86 (1) (2021), pp. 157-166, 10.1002/mrm.28691
16. Larson, P.E.Z., Chen, H.-Y., Gordon, J.W., Korn, N., Maidens, J., Arcak, M., et al., 2018. Investigation of analysis methods for hyperpolarized 13C-pyruvate metabolic MRI in prostate cancer patients. NMR in Biomedicine 31(11): e3997, Doi: 10.1002/nbm.3997.
17. Peder Larson., Sule Sahin., eugene17uf., Xiaoxi Liu., Jeremy Gordon., korench1., et al., 2024. LarsonLab/hyperpolarized-mri-toolbox: Updated READMEs, Visualization Tools and bSSFP Fitting, Doi: 10.5281/ZENODO.10915690.
18. Noworolski, S.M., Reed, G.D., Kurhanewicz, J., Vigneron, D.B., 2010. Post-processing correction of the endorectal coil reception effects in MR spectroscopic imaging of the prostate. Journal of Magnetic Resonance Imaging 32(3): 654–62, Doi: 10.1002/jmri.22258.
19. Sushentsev, N., McLean, M.A., Warren, A.Y., Benjamin, A.J.V., Brodie, C., Frary, A., et al., 2022. Hyperpolarised 13C-MRI identifies the emergence of a glycolytic cell population within intermediate-risk human prostate cancer. Nature Communications 13(1): 466, Doi: 10.1038/s41467-022-28069-2.
20. Chen, H.-Y., Aggarwal, R., Bok, R.A., Ohliger, M.A., Zhu, Z., Lee, P., et al., 2020. Hyperpolarized 13C-pyruvate MRI detects real-time metabolic flux in prostate cancer metastases to bone and liver:

a clinical feasibility study. Prostate Cancer and Prostatic Diseases 23(2): 269–76, Doi: 10.1038/s41391-019-0180-z.

21. Nelson, S.J., Kurhanewicz, J., Vigneron, D.B., Larson, P.E.Z., Harzstark, A.L., Ferrone, M., et al., 2013. Metabolic imaging of patients with prostate cancer using hyperpolarized [1-^{13}C]pyruvate. Science Translational Medicine 5(198): 198ra108, Doi: 10.1126/scitranslmed.3006070.
22. Granlund, K.L., Tee, S.-S., Vargas, H.A., Lyashchenko, S.K., Reznik, E., Fine, S., et al., 2020. Hyperpolarized MRI of Human Prostate Cancer Reveals Increased Lactate with Tumor Grade Driven by Monocarboxylate Transporter 1. Cell Metabolism 31(1): 105-114.e3, Doi: 10.1016/j.cmet.2019.08.024.
23. Kierans, S.J., Taylor, C.T., 2021. Regulation of glycolysis by the hypoxia-inducible factor (HIF): implications for cellular physiology. The Journal of Physiology 599(1): 23–37, Doi: 10.1113/JP280572.

Chapter 7: Summary, Side Projects and Future works

7.1 Summary

In this dissertation project, new applications of hyperpolarized ^{13}C magnetic resonance imaging were developed and investigated. The overall goals were to validate and improve MR-TRUS fusion biopsy guidance for prostate cancer patients. The development of specialized prostate cancer metabolic imaging techniques using HP ^{13}C MR and calculated k_{PL} values to grade aggressiveness and stage cancer is biological and medically focused to address current unmet clinical needs. Developing new $^{13}C/^{1}H$ dual-element endorectal coil, C13-array combining endo coil and external detectors into a multichannel array, novel acquisition, and analysis methods for improved prostate cancer characterization and staging are the engineering parts of this proposal.

Chapter 3 describes the development of a new dual-element endorectal coil and preliminary comparative results from both phantom tests and Active Surveillance (AS) patient studies. A new $^{13}C/^{1}H$ dual-element endorectal coil was designed, 3D printed and manufactured with optimal dimensions to improve the comfort and tolerability for patients and achieve higher SNR over the original endorectal coil used for over a decade. After bench and phantom tests, the new endorectal coil was applied in patient studies for mpMRI-TRUS guided fusion prostate biopsies with hyperpolarized C-13 pyruvate molecular imaging in patients on active surveillance. The results of this novel approach with the new $^{13}C/^{1}H$ ERC provides an increase in sensitivity, image quality and ultimately supports better detection of lesions.

In Chapter 4, development of techniques and establishment of a workflow using hyperpolarized ^{13}C (HP ^{13}C) MRI and the pyruvate-to-lactate conversion rate (k_{PL}) biomarker to guide

MR-transrectal ultrasound (TRUS) fusion prostate biopsies is presented. This technical development study demonstrated the feasibility of adding HP ^{13}C-pyruvate MRI to guide TRUS fusion prostate biopsies. HP-MRI was integrated into the diagnostic mpMRI workflow, complete with identification of ^{13}C research targets and sampling of these targets in fusion biopsies. These initial results support future studies in larger cohorts of patients to advance and evaluate the role of HP ^{13}C MRI guided targeted biopsy for improving prostate cancer risk stratification.

Chapter 5 presents the development and demonstration of the *in vivo* feasibility of a 3D balanced steady-state free precession (3D-bSSFP) urea sequence with a stack-of-spiral acquisition for improving the signal-to-noise ratio (SNR) and spatial resolution of the first hyperpolarized ^{13}C MRI human studies with the injection of co-hyperpolarized [1-^{13}Cpyruvate and [^{13}C, $^{15}N_2$]urea imaging contrast agents. The 3D-bSSFP urea sequence with a stack-of-spiral acquisition was demonstrated to increase the SNR and image quality for [^{13}C, $^{15}N_2$]urea in co-hyperpolarized [1-^{13}C]pyruvate and [^{13}C, $^{15}N_2$]urea imaging studies. This work lays the foundation for future human studies to achieve high-quality, high-SNR, and simultaneous metabolism and perfusion imaging.

Chapter 6 describes the first-in-human co-hyperpolarized [1-^{13}C]pyruvate and [^{13}C, $^{15}N_2$]urea imaging study. This first-in-human radiopathologic study demonstrates the feasibility of dual-agent HP MRI in prostate cancer patients, and the potential for simultaneous assessment of tumor metabolism and perfusion to detect aggressive prostate tumors.

7.2 Side Projects

Next in this chapter side projects conducted and future plans are presented.

7.2.1 Developing novel acquisition, reconstruction, and analysis methods for improved prostate cancer characterization

Hyperpolarized ^{13}C MRI data are acquired with a metabolite-selective EPI acquisition[1]. This type of imaging scheme is inherently more flexible than spectroscopic imaging, as the metabolites of interest are selectively excited and encoded, eliminating the need to encode the entire spectrum. However, the single-shot approach increases the echo time (TE) at higher spatial resolution, resulting in signal loss and blurring due to $\mathbf{T_2^*}$ decay. To overcome this limitation and retain high SNR at high spatial resolution. Partial Fourier acquisition and reconstruction methods are being developed in which data from as little as one-half of *k*-space is collected and is used to generate an entire MR image[29,30,31]. Some information in k-space data is redundant that shows its peculiarly mirrored property called the conjugate (Hermitian) symmetry which exists whenever a Fourier transform is performed on any real-valued function[10,11,12]. This property is possible when no phase error occurred during data collection[5-12]. In MR imaging, the conjugately symmetric points represent corresponding data acquired on the rising and trailing tails of two echoes obtained with opposite phase encoding steps(Figure 7.1).[5-12] In theory, only half of *k*-space data needs to be collected, and the other half can be mirrored.[10-12]

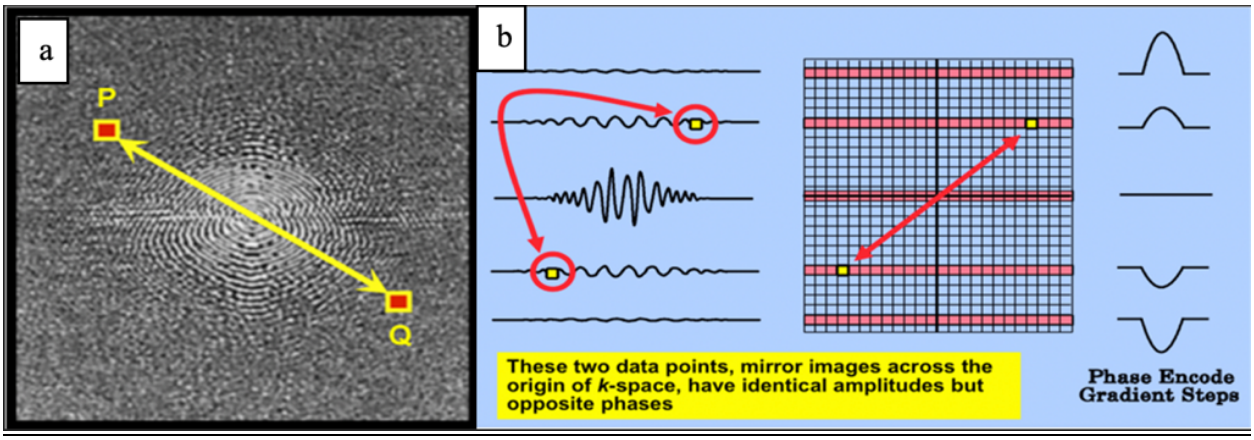

Figure 7.1: Shows Partial Fourier acquisition methods for 2D data sets. (a) Conjugate symmetry of points P and Q. If data for P is known the data for Q can be calculated. (b) Conjugate symmetry of k-space. Mirror image locations across the origin of k-space have real components of the same sign but imaginary components of the opposite sign. (Images adapted from mriquestions.com).

Two types of partial Fourier imaging used in common practice are known generically as read conjugate symmetry and phase conjugate symmetry(Figure 7.2).[24-31] The primary advantages of partial Fourier acquisition in the frequency and phase-encode directions are reduced echo time (TE) and reduced scan time, respectively.[24-31] Phase-conjugate symmetry techniques use data from the top half of *k*-space to estimate data in the lower half of *k*-space (Figure 7.2 A). The k_y-direction is usually taken to be synonymous with the phase-encoding axis in 2D-spin warp imaging. Thus, the name "phase-conjugate symmetry" is used for this type of top-to-bottom data synthesis/estimation.[10-12] Phase-conjugate symmetry techniques reduce imaging time while preserving spatial resolution at the expense of the signal-to-noise ratio (SNR)[7].

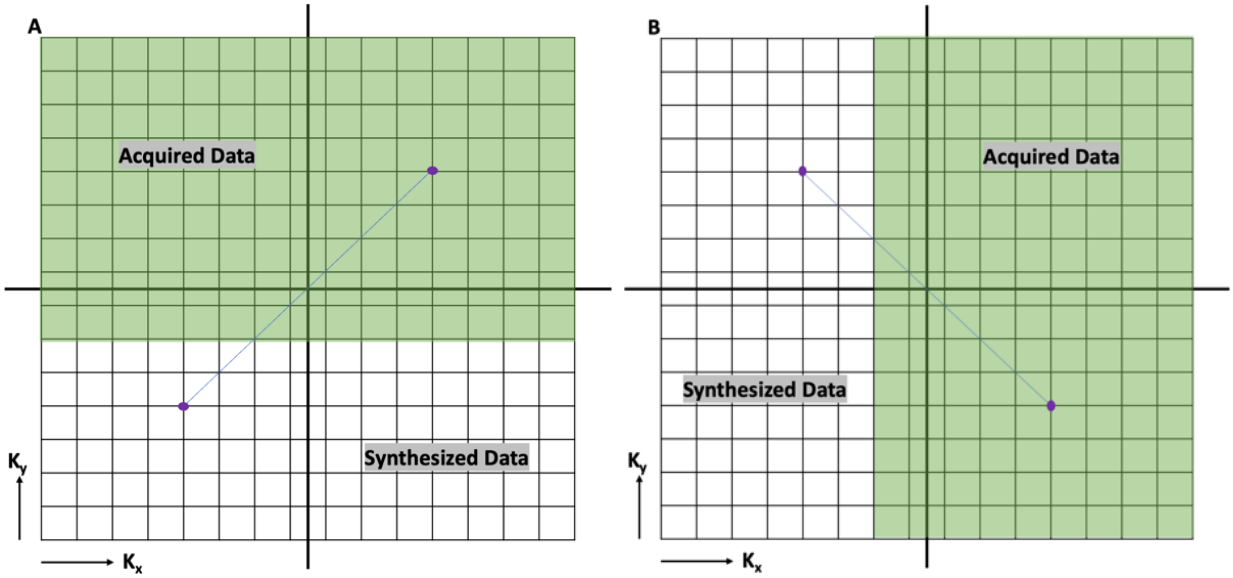

Figure 7.2: Two partial Fourier acquisition methods for 2D data sets. k_x and k_y represent the frequency-and phase-encode directions, respectively. In both cases about half of the k-space data is sampled and the other half is synthesized/reconstructed. **A**. Phase-conjugate symmetry: about half of k-space is sampled in the phase-encoding direction while k-space in the frequency encode direction are fully sampled. **B**. Read-conjugate symmetry: about half of k-space is sampled in the frequency encode direction while k-space in the phase encoding direction is fully-sampled.

Similarly, in read-conjugate symmetry partial Fourier technique, one-half of k-space is used to synthesize the other half.[8,9,10] The direction of symmetry for read-conjugate symmetry is in the

frequency-encode direction.[9,10] Because the *kx*-axis is commonly chosen in diagrams to represent frequency-encoding, read symmetry can be visualized as acquiring data from the "right half" of *k*-space and estimating data in the "left half" as can be seen in Figure 7.2B[5-10]. The sampled "right half" of *k*-space comes from the later portions of each MR echo. Unlike phase conjugate symmetry, the full number of phase-encoding steps are still acquired in read-conjugate symmetry so there is no direct time savings[10-12]. The echo time (TE) can be made shorter by sampling only part of an echo (Figure 7.3).[2-12] Partial Fourier acquisition in the frequency-encode direction reduces gradient moments along that axis, which can reduce flow and motion artifacts.[5-12] Read-conjugate symmetry is particularly advantageous for rapid and echo-planar techniques, but it is also widely used in many other applications including MR angiography and T1-weighted spin-echo imaging. When echo time (TE) is short, the free induction decay (FID) generated by the RF- pulse may spill into the early rising portion of the echo. An image with short TE and little interference between the free induction decay and echo signals can be obtained by sampling the back half of each echo and using read conjugate symmetry to reconstruct the front half[9]. Partial echo of a selected echo time (TE) generates a better SNR by extending sampling time far into the right side of the echo[10,11]. In addition, read conjugate symmetry provides a small FOV at a given echo time as the longer sampling time is associated with the lower gradient amplitude[11,12]. Read conjugate symmetry also reduces the gradient moments along the readout axis which in turn results in reduced flow and motion artifacts in the frequency encode direction.[11,12]

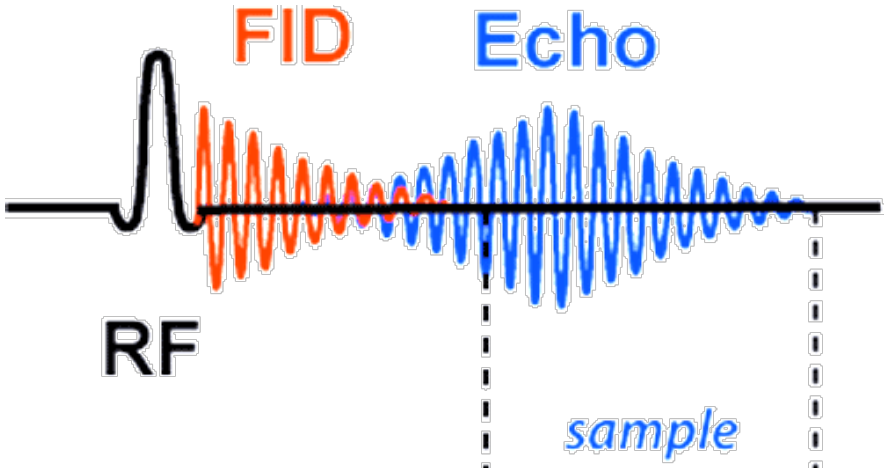

Figure 7.3: When echo time (TE) is short, the free induction decay (FID) generated by the RF- pulse may spill into the early rising portion of the echo. An image with short TE and little interference between the free induction decay and echo signals can be obtained by sampling the back half of each echo and use read conjugate symmetry to reconstruct the front half. (Adapted from mriquestions.com).

The goal of this project was to utilize conjugate symmetry of the partial Fourier imaging techniques to develop novel acquisition, reconstruction and analysis methods for improved prostate cancer characterization and staging. This project retrospectively and prospectively investigating the potential value of using under-sampled k-space to improve HP C-13 MRI. This is achieved by incorporating partial-Fourier in the blip (phase encode) direction of the EPI to reduce the echo train length, reducing the TE and improving SNR and image sharpness. Reconstruction was then performed using the Projection On Convex Sets (POCS) algorithm[14].

Numerical simulations was first performed to show the fidelity of the POCS algorithm to retain image quality with k-space coverage between 50-100%. $\mathbf{B_0}$ inhomogeneity and $\mathbf{T_2^*}$ decay will be incorporated to simulate the signal loss and phase accrual we expect to observe in patients. We have implemented the POCS algorithm in MATLAB and developed a numerical phantom to show the proof of concept with Partial-Fourier reconstruction. To quantify image quality, Structural Similarity Index Measure (SSIM), Root Mean Square Error (RMSE) and SNR are calculated as:

$$SNR = \frac{SI_{mean}}{SD_{noise}} \tag{7.1}$$

$$RMSE = \sqrt{\sum_{i=1}^{n} \frac{(\overline{y_i} - y_i)^2}{n}} \tag{7.2}$$

$$SSIM = \frac{(2\mu_x\mu_y + C_1)(2\sigma_{xy} + C_2)}{(\mu_x^2 + \mu_y^2 + C_1)(\sigma_x^2 + \sigma_y^2 + C_2)} \tag{7.3}$$

For SSIM, x is the compressed image, y is the reference image, μ_x is the mean of x, σ^2_x is the variance of x, σ_{xy} is the covariance between x and y, C_1 is 0.01 times the dynamic range of the pixel values and C_2 is 0.03 times the dynamic range of the pixel values. For RMSE, n is the number of time points, y hat is the reference at a time point t and y bar is the actual across all time points. These metrics will be compared, and contour maps of the parameters graphed for the POCS algorithm compared to a zero padded reconstruction to determine the minimum k-space coverage needed to retain high fidelity. Subsequently, phantom studies on the scanner will be used to investigate the improvement in image quality and SNR with partial Fourier. Under-sampled data reconstructed with POCS will be compared to fully sampled datasets. SNR and SSIM will be compared to quantify the improvement in SNR and the agreement in SSIM to confirm the results from numerical simulation. These results will form the foundation for acquiring prospectively under-sampled human hyperpolarized data proposed in SA4.

7.2.2 Preliminary Results

A POCS based partial Fourier simulation MATLAB code has been written to show the proof of concept with Partial-Fourier reconstruction (Figure 7.4). First, it was used with ideal Shepp Logan phantom where Structural Similarity Index Measure (SSIM), Root Mean Square Error (RMSE) and SNR were compared, and contour maps of the parameters are graphed for both the POCS based and zero padding partial Fourier techniques. The results supported the theory that when no noise is

introduced partial Fourier reconstruction depend on T_2^* values with pf values showing negligible effect whereas zero padding reconstruction depend on pf values while T_2^* values seem to show negligible effect. On the other hand, when high noise is introduced both pf and T_2^* affect both partial Fourier and zero padding reconstructions.

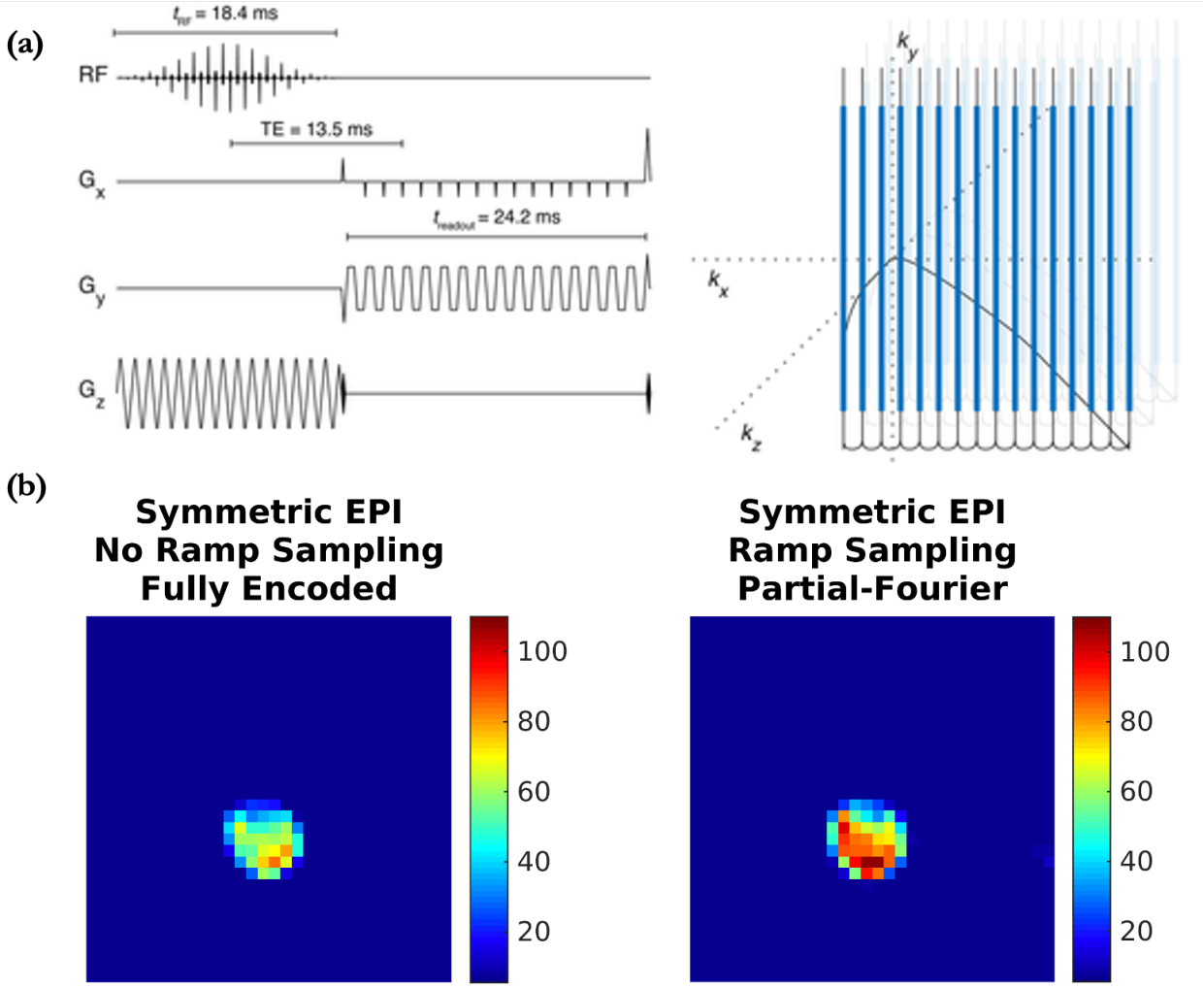

Figure 7.4: Partial Fourier acquisition for single-shot EPI that will be applied. (a) Pulse sequence diagram and k-space coverage for partial-Fourier acquisition in the blip (k_y) dimension. Combining partial Fourier with EPI in the blip dimension will reduces the TE, minimizing T2* decay and improving SNR and image sharpness.[23] (b) Initial phantom results using the EPI pulse sequence show a >1.2-fold gain in SNR with a partial Fourier acquisition.

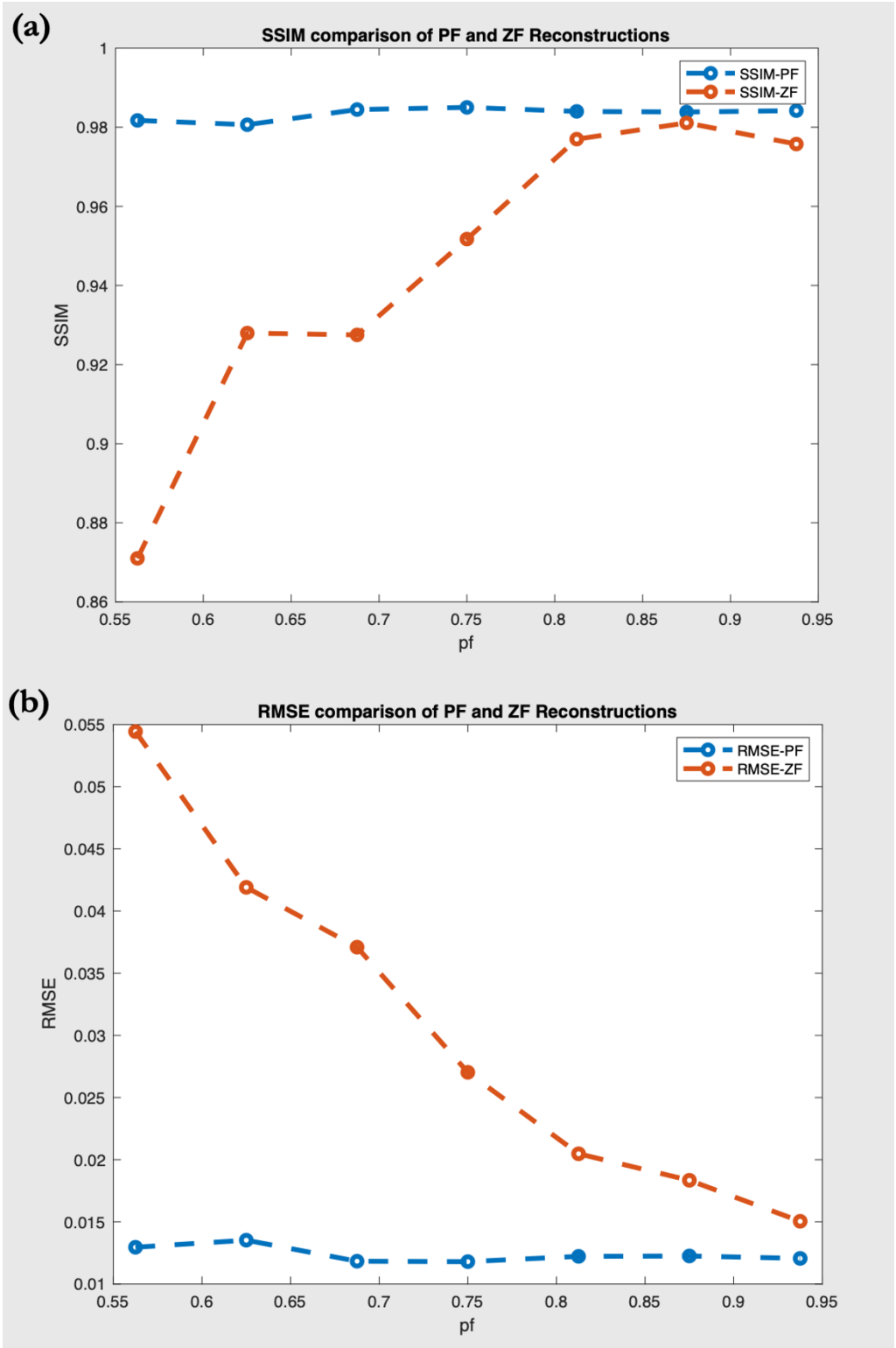

Figure 7.5: Shows the comparative partial Fourier reconstruction of POCS based partial Fourier reconstruction and zero padding partial Fourier reconstruction on images acquired on fully sampled k-space on a patient. (a) SSIM shows that POCS based reconstruction is superior to zero padding reconstruction especially when the partial fraction ratio is low. (b) RMSE data correlates with SSIM and suggests that the POCS based reconstruction is more accurate than zero padding reconstruction.

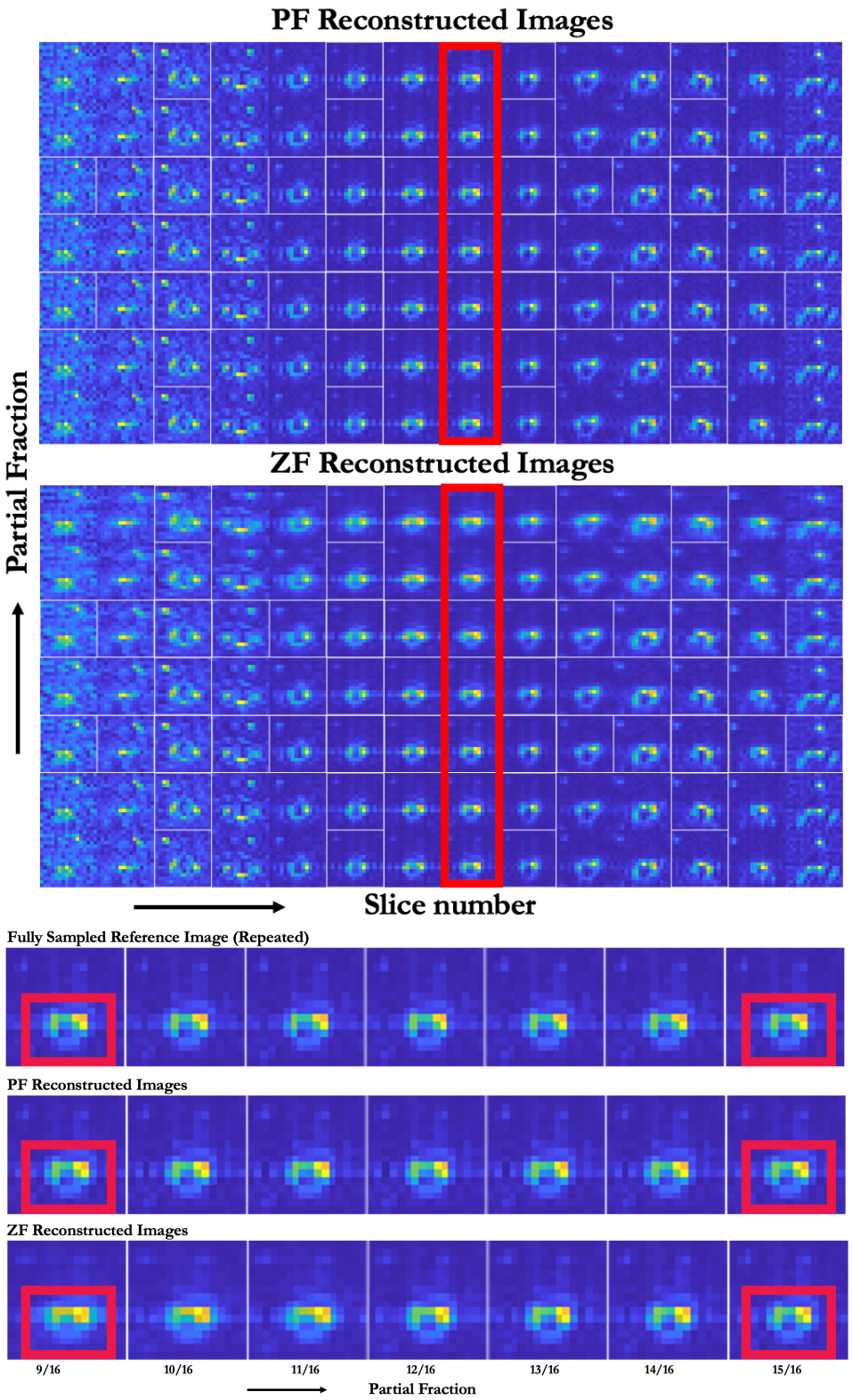

Figure 7.6: Retrospective comparative data of a patient study that were acquired with full k-space. These images were reconstructed with POCS based partial-Fourier reconstruction and zero padding partial-Fourier reconstruction where the respective SSIM and RMSE data is mentioned in Figure 7.5.

7.3 Future Plans

For even higher sensitivity, we plan to develop a novel dual-element ER coil (Figure 7.7). A novel multichannel ^{13}C coil with 16 channels combined with the new dual-element ERC (Figure 7.8) to enable unprecedented sensitivity over the entire prostate, peri-prostatic regions and adjacent lymph nodes where local cancer spread occurs. We expect that this will significantly improve the staging of advanced prostate cancer and at an earlier time than with current methods. In this project, a new multichannel ^{13}C coil array leveraging our prior developments (Figure 7.8), will be utilized to enable multichannel coil combination for increased SNR, parallel MRI and the spatial coverage needed for improved detection of aggressive prostate cancer and metastatic spread to the prostatic bed and lymph nodes. ^{13}C phased array coils require the specialized RF circuitry for ^{13}C & ^{1}H detuning during transmit and during reception detuning & optimal pre-amplification of the ^{13}C signals.

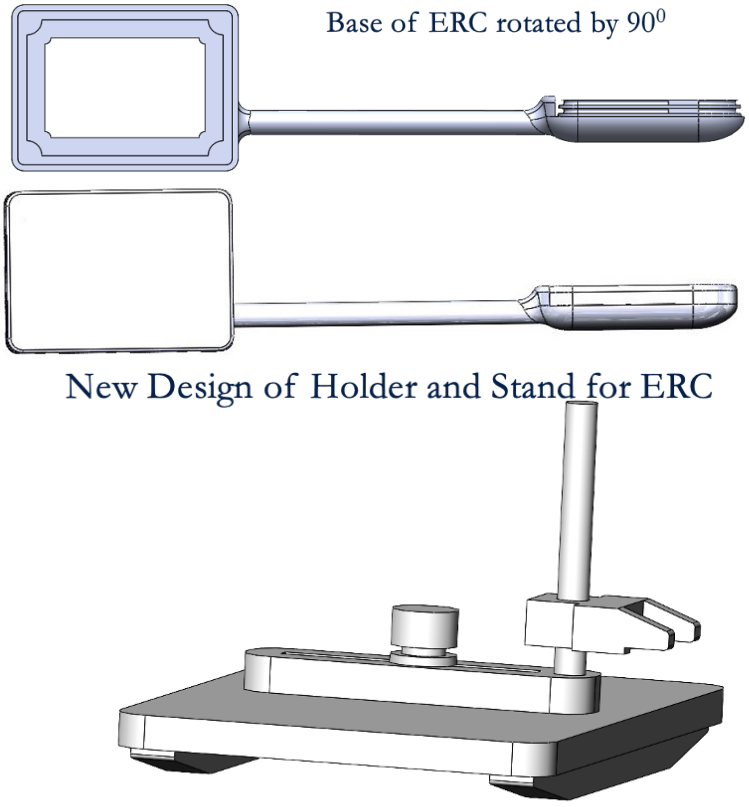

Figure 7.7: SolidWorks design of housing of the newly $^{13}C/^{1}H$ Dual-element endorectal coil with the base rotated by 90^0 and its holder and stand.

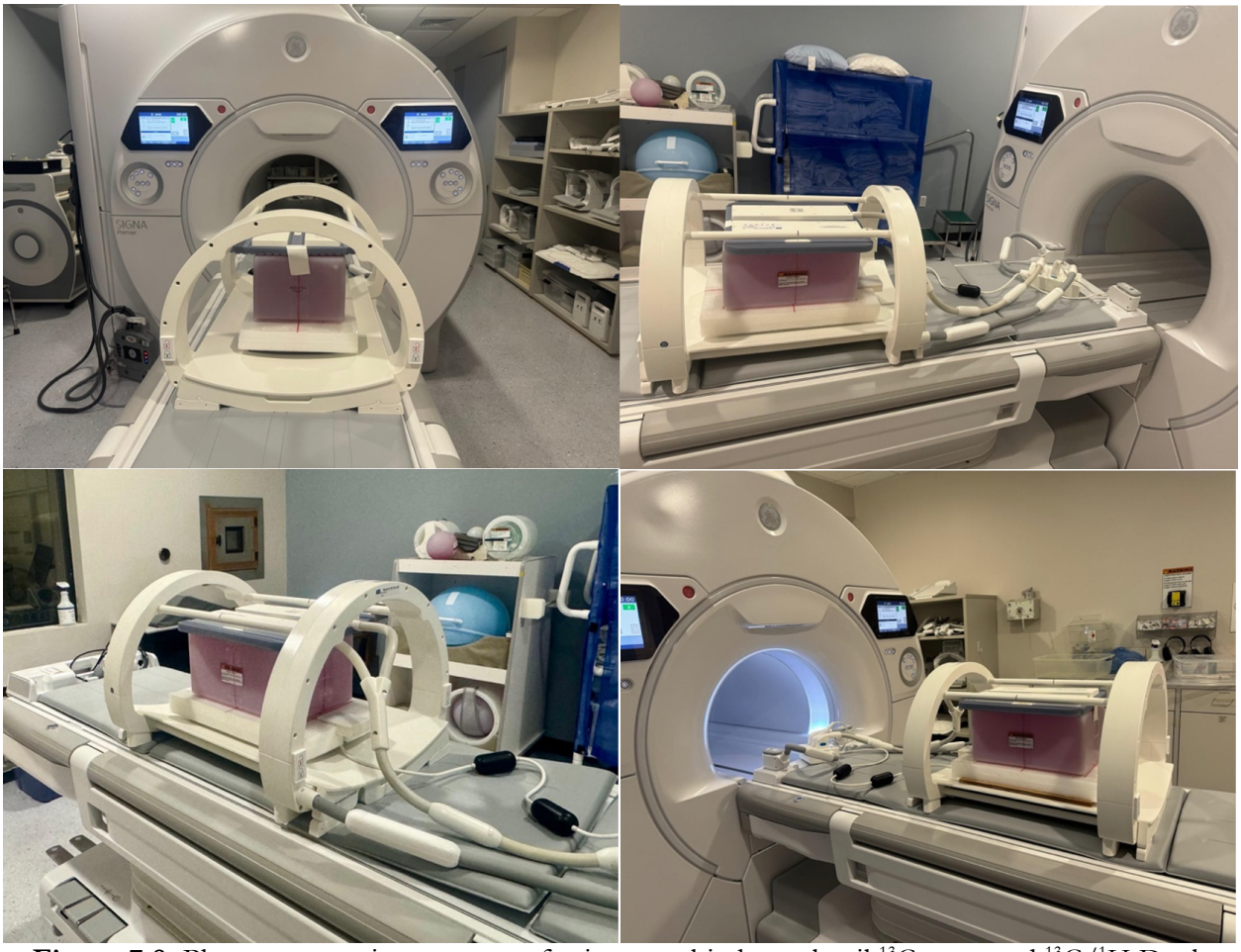

Figure 7.8: Phantom experiment setup of using a multi-channel coil ^{13}C array and $^{13}C/^{1}H$ Dual-Element endorectal coil.

7.3.1 Pilot Patient Studies with the New Hardware and Acquisition Methods

Following bench and phantom safety & performance testing performed above, human studies will be performed using the new hardware and acquisition technologies developed in these projects. To quantify the improvement in image quality with the new external coil, the volunteer subjects will receive two injections of [1-^{13}C]pyruvate, one acquired with the new 16-channel external coil and the other with the current 8-channel array used in prior studies. The [1-^{13}C]pyruvate imaging protocol will consist of metabolite-selective EPI for pyruvate and lactate. The acquisition will toggle between fully-

sampled and partial-Fourier EPI throughout the dynamic scan in order to quantify the improvement in signal-to-noise ratios (SNR) and image quality. Quantitative measures of SNR and coverage will be compared to the current coil by the candidate and image quality improvements will be assessed by the radiologists involved in these studies. Signal variation between the two injections due to differences in polarization and injection time will be removed prior to analysis. Multichannel ^{13}C data will be pre-whitened and coil combined in MATLAB using SNR-optimal methods developed for multinuclear spectroscopic imaging[15]. All methods & results will be disseminated via the current HP center infrastructure to all interested academic sites and industry partners.

Since two HP ^{13}C-pyruvate MRI experiments in the same patient are routinely done due to its safety, we can compare HP data between coils in a single exam. The partial-Fourier EPI pulse sequence and the new coils developed in this proposal will be used to acquire data in patients to determine the coverage and efficacy of the new coils and imaging approaches developed and discussed in this dissertation. Based on our preliminary study using an external commercial 16-channel array that was not optimized for prostate imaging[32] the spatial resolution & coverage will initially be set to encompass the entire prostate, peri-prostatic regions and adjacent lymph nodes where local cancer spread occurs. Quantitative measures of SNR and coverage will be compared to studies using the prior endo coil and between fully-sampled and partial-Fourier acquisitions in the same exam. Also, image quality improvements will be assessed by the radiologists involved in these studies.

7.4 References

1. Chen HY, Larson PEZ, Bok RA, et al. Assessing Prostate Cancer Aggressiveness with Hyperpolarized Dual-Agent 3D Dynamic Imaging of Metabolism and Perfusion. *Cancer Res.* 2017;77(12):3207-3216. doi:10.1158/0008-5472.CAN-16-2083
2. Pauly J, et al. (2005) Partial k-Space Reconstruction.
3. Ohliger, M. A., Larson, P. E., Bok, R. A., Shin, P., Hu, S., Tropp, J., Robb, F., Carvajal, L., Nelson, S. J., Kurhanewicz, J., & Vigneron, D. B. (2013). Combined parallel and partial fourier MR reconstruction for accelerated 8-channel hyperpolarized carbon-13 in vivo magnetic resonance Spectroscopic imaging (MRSI). *Journal of magnetic resonance imaging : JMRI*, *38*(3), 701–713. https://doi.org/10.1002/jmri.23989
4. Geraghty BJ, Lee CY, Chen AP, Perks WJ, Soliman H, Cunningham CH. Partial Fourier reconstruction for improved resolution in 3D hyperpolarized (13) C EPI. Magn Reson Med. 2020;83:2150–9. https://doi.org/10.1002/mrm.28079.
5. Gordon JW, Vigneron DB, Larson PE. Development of a symmetric echo planar imaging framework for clinical translation of rapid dynamic hyperpolarized ^{13}C imaging. *Magn Reson Med.* 2017;77:826–832.
6. Haacke E, Lindskogj E, Lin W. A fast, iterative, partial-Fourier technique capable of local phase recovery. *J Magn Reson.* 1991;92:126–145.
7. McGibney G, Smith M, Nichols S, Crawley A. Quantitative evaluation of several partial fourier reconstruction algorithms used in MRI. *Magn Reson Med.* 1993;30:51–59.
8. Geraghty BJ, Lau JY, Chen AP, Cunningham CH. Dual-echo EPI sequence for integrated distortion correction in 3D time-resolved hyperpolarized ^{13}C MRI. *Magn Reson Med.* 2018;79:643–653.

9. Walheim J, Gotschy A, Kozerke S. On the limitations of partial Fourier acquisition in phase-contrast MRI of turbulent kinetic energy. *Magn Reson Med.* 2019;81:514–523.
10. Feinberg DA, Hale JD, Watts JC et al. Halving MR imaging time by conjugation: demonstration at 3.5 kG. Radiology 1986; 161:527-531
11. MacFall JR, Pelc NJ, Vavrek RM. Correction of spatially dependent phase shifts for partial Fourier imaging. Magn Reson Imaging 1988; 6:143-145
12. MCGibney G, Smith MR, Nichols ST, Crawley A. Quantitative evaluation of several partial Fourier reconstruction algorithms used in MRI. Magn Reson Med 1993;30:51-59
13. Kouchkovsky ID, Chen HY, Ohliger MA, Wang ZJ, Bok RA, Gordon JW, Larson PEZ, Frost M, Okamoto K, Cooperberg MR, Kurhanewicz J, Vigneron DB, Aggarwal R, Hyperpolarized 1-[^{13}C]-Pyruvate Magnetic Resonance Imaging Detects an Early Metabolic Response to Immune Checkpoint Inhibitor Therapy in Prostate Cancer, European Urology, Volume 81, Issue 2, 2022, Pages 219-221, ISSN 0302-2838, https://doi.org/10.1016/j.eururo.2021.10.015. (https://www.sciencedirect.com/science/article/pii/S0302283821021163)
14. McGibney, G., Smith, M.R., Nichols, S.T. and Crawley, A. (1993), Quantitative evaluation of several partial fourier reconstruction algorithms used in mri. Magn. Reson. Med., 30:5159. https://doi.org/10.1002/mrm.1910300109
15. Zhu Z, Zhu X, Ohliger MA, Tang S, Cao P, Carvajal L, Autry AW, Li Y, Kurhanewicz J, Chang S, Aggarwal R, Munster P, Xu D, Larson PEZ, Vigneron DB, Gordon JW, Coil combination methods for multi-channel hyperpolarized 13C imaging data from human studies, Journal of Magnetic Resonance, Volume 301, 2019, 73-79,ISSN1090-7807, https://doi.org/10.1016/j.jmr.2019.01.015. (https://www.sciencedirect.com/science/article/pii/S1090780719300217)

Publishing Agreement

It is the policy of the University to encourage open access and broad distribution of all theses, dissertations, and manuscripts. The Graduate Division will facilitate the distribution of UCSF theses, dissertations, and manuscripts to the UCSF Library for open access and distribution. UCSF will make such theses, dissertations, and manuscripts accessible to the public and will take reasonable steps to preserve these works in perpetuity.

I hereby grant the non-exclusive, perpetual right to The Regents of the University of California to reproduce, publicly display, distribute, preserve, and publish copies of my thesis, dissertation, or manuscript in any form or media, now existing or later derived, including access online for teaching, research, and public service purposes.

DocuSigned by:
Daniel Gebregziabher
88A3ABD619BD488...
Author Signature

11/13/2024
Date